US

University of Sussex

Control of Dynamical Regimes in Optical Microresonators Exploiting Parametric Interaction

Luigi Di Lauro

Submitted for the degree of Doctor of Philosophy

University of Sussex

August 2018

Declaration

I hereby declare that this thesis has not been and will not be submitted in whole or in part to another University for the award of any other degree. Part of the contents of this work are reproductions from published and un-published submissions to journals in which I was the first author. In the specific, Chapters 3 and Chapter 4 have been included in the following publication:

L., Di Lauro, J., Li, D., Moss, R., Morandotti,S. T., Chu, M., Peccianti, and A., Pasquazi, "Parametric control of thermal self-pulsation in micro-cavities", *Optics Letters* **42**, 3407-3410 (2017).

UNIVERSITY OF SUSSEX

LUIGI DI LAURO, DOCTOR OF PHILOSOPHY

CONTROL OF DYNAMICAL REGIMES IN OPTICAL MICRORESONATORS EXPLOITING PARAMETRIC INTERACTION

SUMMARY

Microresonators have the ability of strongly enhancing the propagating optical field, enabling nonlinear phenomena, such as bi-stability, self-pulsing and chaotic regimes, at very low powers.

It is fundamental to comprehend the mechanisms that generate such dynamics, which are crucial for micro-cavities-based applications in communications, sensing and metrology.

The aim of this work is to develop a scheme for the control of nonlinear regimes in microresonators, assuming the interplay between the ultra-fast Kerr effect and a slow intensity-dependent nonlinearity, such as thermo-optical effect.

The framework of the coupled-mode theory is applied to model the system, while the bifurcation theory is used to investigate a configuration in which the power and frequency of a weak signal can control the behaviour of a strong pump.

In this regards, this study demonstrates that the effect of a parametric interaction, specifically the four-wave mixing, plays a fundamental role in influencing the nature of the stationary states observed in a micro-cavity.

The results show possible new strategies for enhanced, low-power, all-optical control of sensors, oscillators and chaos-controlled devices. Moreover, the outcomes provide new understanding of the effect of coherent wave mixing in the thermal stability regions of optical micro-cavities, including optical micro-combs.

Acknowledgements

Firstly, I would like to express my gratitude to my supervisor, Dr Alessia Pasquazi, for the priceless advice and the stimulating conversations, which have enormous supported me and my research throughout my PhD. I would like to thank my supervisor, Prof. Matthias Keller, for the helpful feedback on this work.

I am very grateful to Prof. Marco Peccianti, for his brilliant suggestions and expertise that have helped me during my PhD study.

A special thanks to all members of the Emergent Photonics lab, who have been an extraordinary team to work with. In particular, Hualong Bao, Maxwell Rowley, Benjamin Wetzel and Juan Sebastian Totero Gongora for their precious comments, which have widened my research from various perspectives. Thank you to Luke and Andrew, for sharing joy and pain of the PhD experience and making my journey more enjoyable.

I thank my mother for the all the love and sacrifices that she has made to give me the opportunity to become who I am today.

To Rocío, whose love and encouragement have assisted me in those years, even in the darkest moments, I want to say thank you.

Contents

List of Figures

Introduction

Optical whispering-gallery-mode (WGM) microresonators confine light to small regions, enhancing the optical field by resonant recirculation. The ratio between the quality factor and the modal volume of the WGM is fundamental to define the threshold of optical nonlinear effects. Microcavities, with extremely high Q-factors and reduced modal volumes, allow observing such nonlinear effects at milliwatts powers. The high confinement of the optical field, by design, forces the optical circulating power, lost at each round trip, to dissipate through a very small surface area, toward the mode volume in the bulk of the microresonator. This phenomenon can be identified as the "thermo-optic" effect, which causes a thermal drift of the cavity resonances, proportional to the intensity of internal optical field; it can be observed in microcavities made with insulators [1], as well as in semiconductor microcavities [2–4]. Another typical effect in third-order nonlinear materials is the Kerr nonlinearity. The Kerr and thermo-optic have a different response time. The Kerr effect is generally faster than thermo-optical one, having a ratio between relaxation times of several orders of magnitude (e.g. integrated microresonators). Besides thermo-optic effect, there exist other intensity-dependent nonlinearities, with a slow response if compared with the fast Kerr one. For instance, free carries nonlinearities generated by two-photon absorption in semiconductor cavities [2]. The interaction among slow and fast nonlinearities can influence the overall nonlinear behaviour of the system, providing a low threshold for optical bi-stability and hysteretic response [1, 5], oscillatory instability [6, 7], four-wave mixing amplification at milliwatt levels in integrated ring-resonators [8, 9] and chaotic dynamics [1]. Generally speaking, the dynamical behaviour of a microcavity depends on the type of equilibrium that the system reaches after an initial transient, and from which it evolves in time, defying the system's *phase portrait*. The nature of such an equilibrium can vary as some specific parameters of the system are changed, producing *bifurcations* of the equilibrium in the parameter space. A way to govern the system's bifurcations plays a central role in achieving the desired performance.

The aim of this work is to demonstrate a possible approach for controlling nonlinear dynamics in optical microcavities, in presence of both Kerr and an intensity-dependent nonlinearity with a first-order time response, such as a thermal nonlinearity.

This thesis is organised as follows. In Chapter 1, I will discuss the properties of microresonators, tracing back their origins, describing their properties and exploring the technologies of fabrication and possible applications. Then, in Chapter 2, I will introduce some key concepts of dynamical system theory, including methods for stability and bifurcation analysis, in order to build up a theoretical background that will be essential to study the equilibrium configurations of the system and predict its evolution in the phase space. I will investigate the conditions that define the nature of a stable solution and show some relevant bifurcations in the domain of our analysis. The equations modelling a microcavity will be derived in Chapter 3, within the framework of the coupled-mode theory. Here, I will extend the classical approach of the coupling of modes in linear waveguided structures to the case of nonlinear Kerr medium. In Chapter 4, the influence of the thermo-optic effect, in addition to the Kerr nonlinearity, will be examined in different conditions. Firstly, in the straightforward case of single frequency mode, then in the case of two frequencies coupling. In the latter scenario, through our scheme for bifurcation control, I will prove that the nonlinear regimes of a strong pump can be controlled and driven by a week-intensity signal, ruled by the four-wave mixing. I will present some relevant examples of switching and transferring of dynamics between cavity modes via four-wave mixing, including the case of a route to chaos through the intermittency phenomenon. Finally, the main outcomes and future perspectives of this work will be summarised and discussed in the Conclusions Chapter.

Chapter 1

Background and Applications of Optical Microresonators

1.1 Wispering Gallery Mode Microresonators

At the beginning of 20th century, the *whispering gallery* effect was initially observed and studied by Lord Rayleigh in the contest of the channelling of acoustic modes by the dome of St. Paul's Cathedral in London [10]. The sound waves produced at a point of the dome were reflected with minimal diffraction by the surface of the wall, so that they could continuously bounce with the same angle and travel along the dome's wall. The idea of total internal reflection, applied to explain this phenomenon in the field of acoustic, had already been applied to the field of optics by Daniel Colladon and Jacques Babinet in the 1840s [11], to describe the propagation of electromagnetic waves within curved waveguiding structures. The latter work allowed the fabrication of the first optical fibre between the late 19th and early 20th centuries. With such an achievement, a complete analogy among the fields of acoustic and optics was finally possible.

A *whispering-gallery mode* (WGM) inside a bent optical fibre is enabled when the reflected light beam propagates along the outer surface, below a certain minimum radius of curvature [12]. An optical cavity that supports WGMs is called *whispering-gallery mode resonator* (WGR). Resonant cavities with size range from millimetres to a few micrometers are known as *microresonators* or *microcavities*. The materials employed for microresonators fabrication include silica, silicon, silicon nitride and oxynitride, semiconductors, such as gallium arsenide (*GaAs*), indium phosphide (*InP*), and crystalline materials, such as lithium niobate (*LiNbO$_3$*), calcium fluoride (*CaF$_2$*) and magnesium fluoride (*MgF$_2$*). The large variety of cavity's shapes that has been investigated over

the years, for instance, microdisks [11, 13–16], microtoroids [17–20], photonic crystal cavities [21–23], bottle [24, 25] and bubble [26–28] microresonators (see Fig. 1.1), offers suitability for different applications. Indeed, in the past two decades, microcavities have gained a key role in applied research, as well as integrated in devices performing complex functions for commercial and technological purposes.
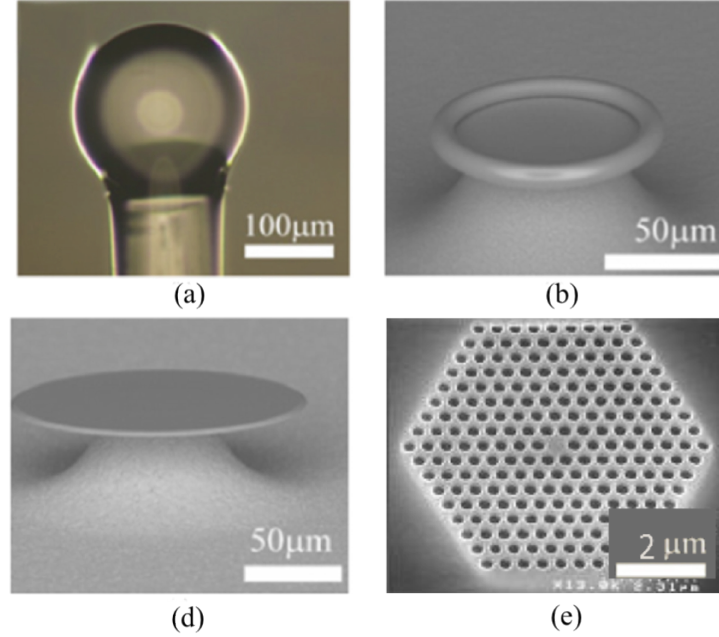
Figure 1.1. Examples of optical microresonator types: (a) silica microsphere; (b) silica microtoroid cavity; (c) silica microdisc; (d) photonic crystal defect microcavity.
A. Pasquazi et al., *Physics Reports* **729** (2018), pp. 1–81.
T. M. Benson et al., *arXiv:physics/0607239*.

1.2 Fabrication Technologies for Microcavities

There are fundamental factors that we have to take into account when designing and fabricating microcavities for potential applications, in the specific, the value of the Q-factor reachable, the cost and robustness, the simplicity of fabrication and the integrability with other technologies. Highly-compact microcavities, with small modal volumes and high-Q factors, exhibiting narrow resonances linewidth, large free spectral range (FSR) and high optical power, are essential factors to consider when realising compact and portable optical devices. Nowadays, it is possible to produce microresonators with the size of a few micrometres [29] and Q-factors reaching $10^{10} - 10^{11}$ [30].

Another important aspect to consider, which has an impact on the performance of microcavities, is the coupling efficiency of the light into and out from the cavity. The latter can be achieved by exploiting fabrication techniques based on the *evanescent-wave coupling*, a phenomenon similar to

the tunnelling effect in quantum mechanics: placing two dielectric waveguides in close proximity (i.e. a waveguide and a microcavity), the evanescent part of the modal field, propagating in one waveguide, can penetrate the adjacent waveguide and excite the n-mode, whose propagation constants are nearly equal [31]. Evanescent-field couplers are opportunely adjusted to control the overlap of the evanescent fields and optimise the exchange of energy between coupled modes. For this purpose, couplers have different geometries, such as prisms, tapered fibres, planar waveguides, as shown in Fig. 1.2.
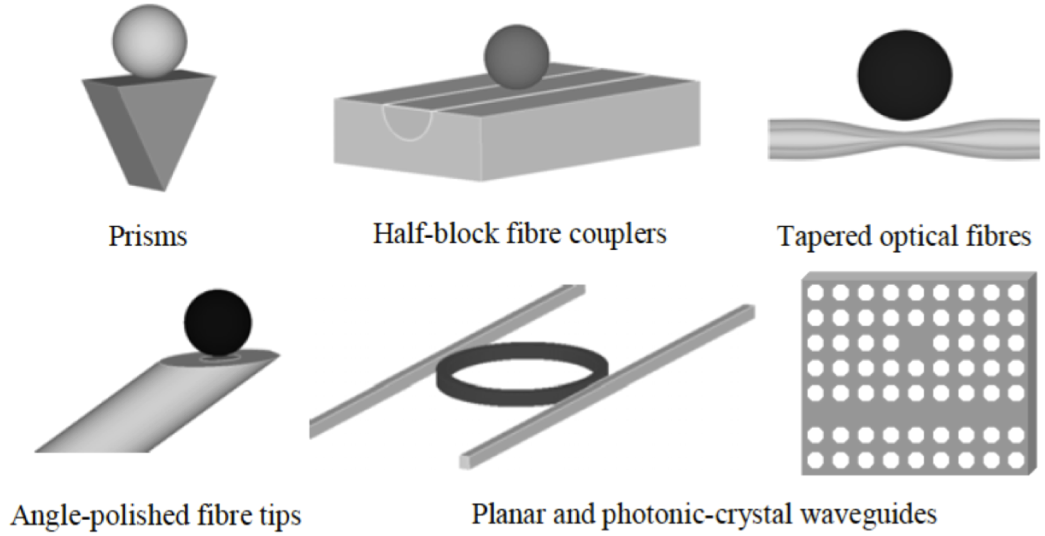
Figure 1.2. Different types of evanescent-field couplers, with various geometries such as prisms, tapered fibres, planar and photonic crystals waveguides.
T. M. Benson et al., *arXiv:physics/0607239*.

The choice of the appropriate method of fabrication depends on the specific design needed (evanescent coupler, shape, material, geometry, etc.), which in turn is tailored to meet the applications's requirements. We can distinguish two main categories of microcavities design: bulk and integrated WGRs platforms.

1.2.1 Bulk Design

One of the simplest microcavity that can be produced in monolithic bulk design is a cylindrical WGM cavity, using a standard piece of telecom single-mode optical fibre, stripped from coating [32, 33]. From that, by choosing an opportune angle of tilting with respect to the coupling waveguide, "spiral" WGMs along the longitudinal direction can be observed [34].

Microresonators with spherical shapes can be obtained in a lab with very effective, cheap and reliable methods. For instance, by melting the tip of a standard telecommunication silica fibre, followed by re-flow of the glass. This is performed typically through ablation via CO_2 laser [35, 36],

although other technique, using microwave plasma torch [37] or rotating electric arc [38], can be applied. Because of the surface tension of the melted silica, the glass re-flows immediately forms a perfect spherical volume, which is highly smooth and with very low roughness, due to the viscosity of the silica. For the fabrication of microspheres with even smaller diameters, the fibre can be either tapered or etched [39]. Microcavities are also shaped on the profile of silica rods, with a similar process involving a CO_2, while the rod is rotated on a spindle [40] (see Fig. 1.3).
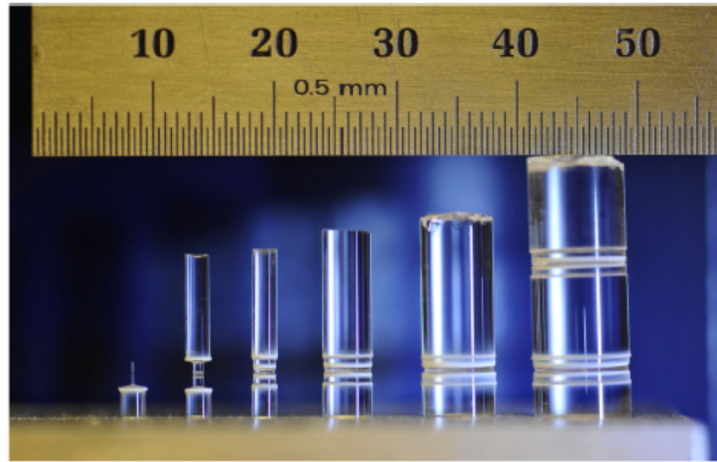
Figure 1.3. Fused silica rod microresonators obtained through ablation via CO_2 laser, with diameters that vary from 200 μm to 8 mm.
A. Pasquazi et al., *Physics Reports* **729** *(2018), pp. 1–81*.

Other techniques rely on standard wafer manufacturing processes, where a thermally-grown silica layer is placed at the top of a substrate of silicon. In this way, silica blocks are created on the wafer and then molten into spherical geometry by controlled heating. Toroidal, disk and ring microresonators can be obtained applying a similar technique: a circular silica pad is initially imprinted on the silica substrate, then a dry-etching step is applied on the remain of the silica layer, followed by a re-flow through a CO_2 laser, in order to reduce the surface roughness and increasing the Q-factor. Monolithic bulk resonators with symmetric shapes, such as spherical, cylindrical and toroidal, allow Q-factors up to 10^{10} [41], as the fabrication processes are able to remove the most of scattering losses [36, 42].

Differently, crystalline materials, such as magnesium or calcium fluorides, are not suitable for melting techniques. Indeed, such a process would destroy their structure and compromise the purity. Nevertheless, there are methods of grinding and polishing that produce crystalline microcavities with very smooth surfaces on a sub-nanometers scale [36, 43, 44], reaching Q-factors up to 10^{11}.

This is also possible because of their low intrinsic absorption and the absence of impurities in the lattice structure [45].

1.2.2 Integrated Technology

In the past ten years, integrated optics has made a huge progress in developing on-chip optical devices, in terms of scalability, reduced footprint, robustness and costs [46–50]. In the same way as electrical conductors carry electrons, bus waveguides can route optical signal directly on-chip. The target is competing in terms of performance with the electronic chip industry, producing complex optical circuits more and more compact, inclusive of filters, modulators, splitter, switches, etc. Silicon is suitable for photonic platforms technology, providing several advantages. First of all, it has very reduced manufacturing costs, then, it offers the possibility of interfacing with existing electronic components, pretty much CMOS technology (Complementary Metal Oxide Semiconductor) [46, 47]; last but not least, silicon is ideal to fabricate high-nonlinear Kerr optical microcavities in different geometries and shapes. However, we have to take into account the significant losses experienced by silicon, caused by two-photon absorption due to the free carriers. To overcome this issue, new CMOS-compatible platforms for nonlinear optics have been developed, for instance, silicon nitride (Si_3N_4) and Hydex glass (high-index doped silica glass) [51] represent a good alternative to silica, with very low linear losses, large nonlinearities and good stability and performances in operational regimes.

Ring microresonators made with Hydex, with a few micrometres of diameter, low bending losses due to the high-index-contrast waveguides, allow high flexibility for compactness and integrability purposes. Moreover, the short round-trip of the optical field enables large FSRs in the order of hundred gigahertz. A four-port ring microresonator made with Hydex [52] is shown in Fig. 1.4. Here, the waveguides are obtained using photolithography and reactive ion etching before over-coating with silica glass. The full compatibility of the device with CMOS technology is achieved by burying the waveguides in fused silica glass. The resonator reaches a Q-factor of 1.2×10^6, corresponding to a mode linewidth of 160 MHz and FSR of 200 GHz. Measurement of nonlinearity have demonstrated a Kerr coefficient five times greater than silica glass, therefore FWM is observed at low power, as well as the thermo-optic effect, as the high confinement of the optical field [53].
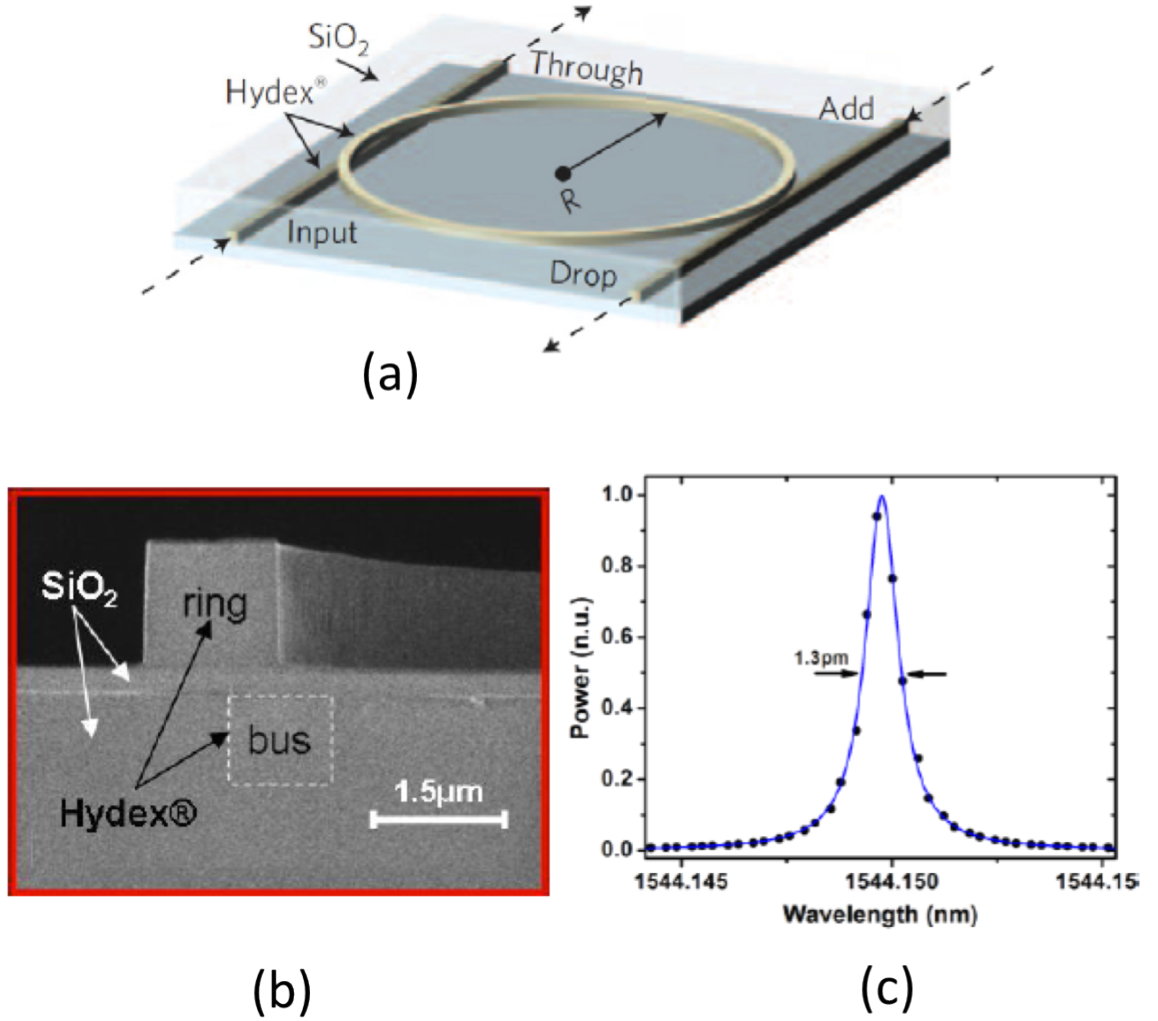
Figure 1.4. Integrated 4 port ring microresonator made with Hydex, with radius $\approx$ 135 μm. (b) SEM (scanning electron microscopy) of the waveguide, with cross-section $\approx$ 1.45μm x 1.5 μm) before depositing upper cladding of SiO; the coupling waveguides (bus) have the same cross section. The waveguide core is high index (n= 1.7 @ λ = 1.55 μm) and the propagation losses have been shown to be as low as $25 GW/cm_2$. (c) Linear transmission spectra of the resonator at the drop port, with FSR of 200 GHz and a mode linewidth of 160 MHz, corresponding to a Q-factor of 1.2 million.
D. J. Moss et al., *arXiv:1404.7619* (2014).

1.3 Applications for Microcavities

In microcavities realised with bulk design, coupling techniques permit the manipulation and filtering of optical signals, obtaining channel-dropping filters and optical add/drop (de)multiplexers [54]. In this regards, passive optical microcavity in the planar configuration (e.g ring or discs), contributed hugely to the progress of telecommunications-oriented photonics. Tunable filters can be made with resonators having an electrically controllable refractive index [15], suitable for ultrafast modulation or switching [55], noise filtering [56], dynamic bandwidth allocation [57], reconfigurable channel routing [58]. The high-quality factors of optical microcavities allow

to stores the light in a reduced volume, realising long buffering in all-optical tunable buffering applications [59], including signal processing in high capacity and ultra-fast communication networks [60, 61]. In the previous section, it has been shown that integrated microcavities, made either in silica or in CMOS-compatible technology, have several advantages with respect to the monolithic bulk design, regarding compactness, portability and low-losses [62]. These features make them preferable over bulk microresonators for optical wavelength multiple-channel filtering for wavelength-division multiplexing in high performance telecommunications [63], modulators for on-chip optical interconnect [64], quantum telecommunications [65],wide-band frequency combs [66, 67], ultra-short pulse generation [68, 69].

Materials exhibiting third-order nonlinear response to an applied electrical field (e.g. silica, silicon, calcium fluoride), such as the Kerr effect in presence of an optomechanical nonlinearity [70], have been effectively employed for designing oscillators in the microwave regime [71]. In integrated ring microresonators, the Kerr optical parametric gain can induce FWM with single pumping laser source [8, 9]. Nonlinear parametric processes, such FWM, enable the generation of optical frequency combs at low power, which offers a very stable optical reference source, with an accuracy up to 10^{-18} [72–76] for applications in metrology [77]. Moreover, the ultra-fast Kerr effect can compete with slower intensity-dependent nonlinearities, e.g thermo-optic nonlinearity (TO), producing self-pulsing [79] and giant self-pulsation [80]. The control of the TO is fundamental for reaching coherent regimes, such as temporal cavity solitons [69, 81, 82], which is crucial for applications in telecommunication.

Microresonantors represent very powerful devices for sensing purpose as well. Due to the considerable Q-factors, even a small change of the intra-cavity field wavelength can be practically observed. Indeed, when placed nearby the evanescent field coupled to a WGM of the resonator, molecules or particles can interact and be polarised by the photons of the field. The latter phenomenon, in turn, induces a shift of the cavity resonances that are excited by the evanescent field, which can be related with the number of molecules, as well as their weight. This can have a number of applications in biology [83, 84] and quantum electrodynamics [42, 85, 86].

Chapter 2

Stability and Bifurcations of Equilibria in Nonlinear Dynamical Systems

2.1 Chapter Introduction

Nonlinear dynamical systems are subject of intense study in transversal topics in various disciplines, such as biology, medicine, chemistry and physics. The study of the equations describing the evolution of a dynamical system has been a branch of physics since the 1600s, after Newton's formulation of the laws of motion and universal gravitation, which laid the foundations of modern physics. In 1881 Poincaré provided a qualitative solution of the three-body problem, introducing the "Poincaré maps" that allow investigating the stability of the steady state solutions of a dynamical system without solving the dynamical equation [88]. Several mathematicians have made fundamental contributions, from Poincaré [88] to van der Pol[1] [89], Cartwright, Littlewood [90, 91], Levinson[2] [92], Andronov[3] [93] and Smale[4] [94], to name only some of them.

With the advent of computers in the 1950s, algorithms to study dynamical systems enabled to simulate numerically experimental conditions. In 1955, Fermi-Pasta-Ulam-Tsingou (FPUT) [95, 96] studied the thermalisation process in a solid, reducing the problem to a simpler unidimensional chain of N atoms in crystals, and assuming the system as an ensemble of the nearest-neighbour nonlinear coupled oscillator, described by the Hooke law. Following the ergodic condition, the

---

[1]A radio engineer who reported one of the first experimental observation of deterministic chaos.

[2]They studied the van der Pol's equations equation for relaxation oscillation, finding simplified solutions.

[3]Andronov gave his contribution on the theory of stability of dynamical systems and bifurcation theory and structural stability. He studied and forged the term "self-oscillation" a connection between oscillations seen in dynamical systems and the theory of Lyapunov stability.

[4]Smale worked on dynamical systems and structural stability extending the previous work of Andronov.

energy supplied to the lowest mode should be equally distributed among the higher modes until reaching the equilibrium, in a long enough time-transient. However, accidentally leaving the computer performing the simulation for longer than scheduled, FPUT observed that the system showed periodicity before converging again to its initial state. The latter was in contraposition with the ergodic behaviour. This paradox, known as "FPUT problem", was one of the first demonstration of nonlinear recurrence; it was solved a few years after, mainly assuming the existence of one-dimensional stable solitons and deterministic chaos. In this perspective, fundamental contributions were given in the 1965s by Zabusky et al. [97], who demonstrated a connection between the periodic nature of the system and the existence of localised excitations, hence solitons. In the 1966s, Izrailev and Chirikiv proved that chaotic orbits appear when the nonlinearity is strong. As the nonlinearity increases, the nonlinear resonances are no longer separate, but overlapped in the frequency space, originating chaotic orbits in the phase space. In the same years, Lorenz performed nonlinear numerical studies on the atmospheric convection, observing a chaotic behaviour of the solutions in a low dimensional system. Such a discovery led Lorenz to define the *Lorenz attractor*, where the set of chaotic solutions of the Lorenz system resemble a *butterfly shape* [98]. Here, the solutions never reach a final state, rather, they keep on oscillating with non-periodical motion. Moreover, Lorentz discovered that the final state was strongly dependent on the initial conditions.

Lorenz and, earlier Poincaré, have shown that chaos can have similarity in a large variety of nonlinear dynamical systems, identifying well defined "routes" to reach a chaotic regime. For instance, the *period-doubling bifurcations* phenomena is a typical route to chaos that, in the 1978, was quantified in terms of Feigenbaum constants, and represented on *bifurcation diagrams* [99]. Nowadays, the study of nonlinear systems belongs to the area of mathematics known as *Dynamical System Theory*. The latter applies different methods to study dynamical systems in a rigorous manner, through the analysis of the steady state solutions and bifurcations, and how those affect the system response.

In this chapter, I will present a qualitative description of basic concepts of stability and bifurcation theory, which will be relevant to fully understand the analysis and results shown in Chapter 4. In Section 2.2, I will define some common terminology concerning dynamical system theory and discuss the stability of equilibrium points. Then, in Section 2.3, I will review most relevant types of local bifurcations and some fundamental global bifurcations of orbits in codimension-1 and codimension-2.

2.2 Stability Analysis of Equilibria

Let us consider a continuous-time dynamical nonlinear system $\{\mathbb{R}^1, \mathbb{R}^n, \phi^t\}$, defined by a set of ordinary differential equations (ODEs) in the vector form:

$$\dot{x} = f(x), \tag{2.1}$$

where $f : \mathbb{R}^n \to \mathbb{R}^n$ is the vector-valued function, and $x \in X$ is the coordinates vector defined on the system's phase space $X : \{x : x = (x_1, x_2, ..., x_n)^T \in \mathbb{R}^n\}$. The system's evolution is typically represented by time-dependent trajectories of an evolution operator ϕ^t that connects any initial state $x_0 \in X$ to some state $x_t \in X$ at time t, assembling the system's phase portrait in a deterministic manner.

A very powerful approach to obtain an insightful analysis of the systems regimes consists in solving the stability problem and classifying the nature of equilibrium points of X. Before approaching the solution of such a problem, we need to introduce some general concepts on the system's stability and phase space of dynamical systems.

Given a generic equilibrium x_0, solution of the equation $f(x_0) = 0$, the Jacobian matrix of $f(x)$ evaluated in x_0 is $J(x_0)$. Let's suppose $\varepsilon(t) = (\varepsilon_1, ..., \varepsilon_n)$ be a small perturbation vector, such that $|\varepsilon(t)| << 1$. Thus, the response of the system at time t against an external perturbation on its initial equilibrium point x_0 is: $x(t) = x_0 + \varepsilon(t)$. Substituting the perturbative expression of $x(t)$ into Eq. 2.1, and assuming $f(x)$ be a smooth function of x, such that we can approximate the function with its Taylor series expansion and neglect terms of order $\mathcal{O}(|\varepsilon|^2)$, we achieve the following linearisation

$$\dot{\varepsilon} = J(x_0)\varepsilon. \tag{2.2}$$

Then, the general solution of Eq. 2.2 can be written as

$$\varepsilon(t) = \varepsilon_0 e^{\lambda t}, \tag{2.3}$$

where ε_0 indicates the eigenvectors of $J(x_0)$, while λ its complex eigenvalues, such that $\lambda = \alpha \pm i\beta$, with α and β real and imaginary parts, respectively. From Eq. 2.3, if all eigenvalues of the Jacobian matrix have negative real parts, the equilibrium x_0 is stable because $|\varepsilon(t)| \to 0$ as $t \to \infty$. Indeed, the perturbed solution, after a certain transient of time, converges to x_0 as ε tends to zero exponentially. Instead, if one of the eigenvalues have a positive real part, $\varepsilon(t)$ grows exponentially, such that:

$|\varepsilon(t)| \to \infty$ as $t \to \infty$. At this point, it is useful to introduce a *topological* classification of the equilibria that allows studying qualitatively the behaviour of our system nearby its equilibria, by comparison with general features of the behaviour of equivalent systems.

In a continuous-time dynamical system, an equilibrium point x_0 is called *hyperbolic* if all the eigenvalues of $J(x_0)$ have non-zero real parts. Hyperbolic equilibria have noteworthy properties, first of all, they are insensitive to small perturbations, preserving qualitatively the phase portrait nearby the equilibria. In other words, the system's phase portrait is *structural stable* in a neighbourhood of a hyperbolic equilibrium. Secondly, hyperbolic equilibria allow the existence of stable and unstable *manifolds*[5], and, most important, the system is *topological equivalent*[6] to its linearisation nearby an hyperbolic equilibrium. The latter statement is supported by the Hartman-Grobman theorem [100], also known as *linearisation theorem*, which makes possible studying the qualitative behaviour of a nonlinear system, such as Eq. 2.1, by investigating quantitatively the behaviour of its linearisation, thus Eq. 2.2, nearby its equilibria.

Conversely, when at least one eigenvalue of $J(x_0)$ has zero real part, the equilibrium x_0 is called *non-hyperbolic*. Those type of equilibria are very sensitive to even small perturbations, which can cause a drastic change of the system's phase portrait, leading to the branching of the equilibrium curve, hence to local bifurcations of non-hyperbolic equilibria. Indeed, non-hyperbolic equilibria represent *critical points* (or singularity) for the system. The type of stability of non-hyperbolic equilibria cannot be defined by the sign of the eigenvalues of the Jacobian of the linearised system Eq. 2.2; it depends on nonlinear terms of $f(x)$. A simple classification of hyperbolic equilibria, for two-dimensional (n=2) and three-dimensional (n=3) systems, is reported in Fig. 2.1 and Fig. 2.2, respectively. Non-hyperbolic equilibria typically assume the name of the bifurcation from which they are originated, therefore, for sake of clarity, I will introduce some of them along with the correspondent bifurcation directly in the next section.

---

[5]In our context, a manifold can be intended as a set of points in $\mathbb{R}^n$ that satisfy the system of equations: $f(x) = 0$.

[6]Two dynamical systems are topological equivalent when they have qualitatively similar phase portraits, for instance, same number of equilibria and cycles of the same stability types.

Eigenvalues	Phase portrait
$\text{Im}[\lambda_i]$ $\text{Re}[\lambda_i]$	stable node
$\text{Im}[\lambda_i]$ $\text{Re}[\lambda_i]$	stable focus
$\text{Im}[\lambda_i]$ $\text{Re}[\lambda_i]$	saddle
$\text{Im}[\lambda_i]$ $\text{Re}[\lambda_i]$	unstable node
$\text{Im}\,\lambda_i$ $\text{Re}\,\lambda_i$	unstable focus
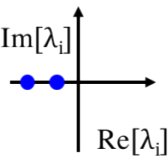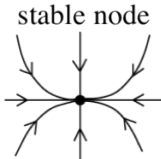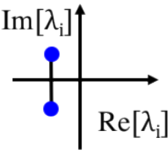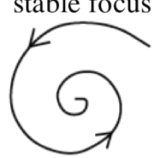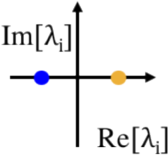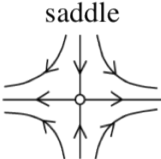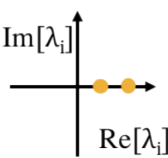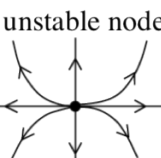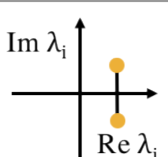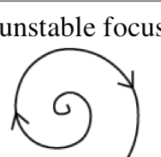
Figure 2.1. Hyperbolic equilibria in a 2-d phase space. Eigenvalues", reporting the eigenvalues on the complex plane with blue dots for the stable case and yellow dots for the unstable case. "Phase portrait" reporting the system's trajectories in the phase space, corresponding to the specific equilibrium.

Adapted from: *Elements of Applied Bifurcation Theory* (pp. 49), by Y. A.Kuznetsov, 2004, New York, NY, Springer Science. Copyright 2004 by Springer.
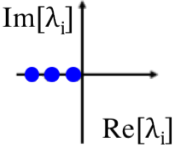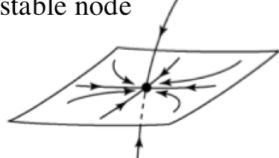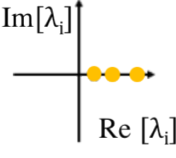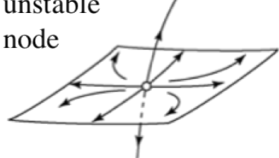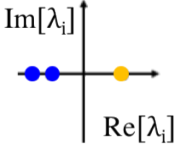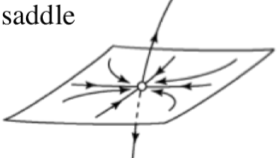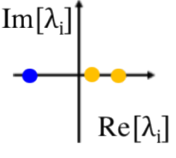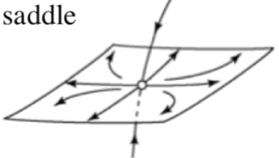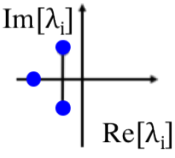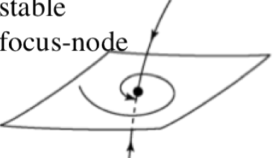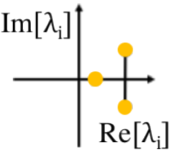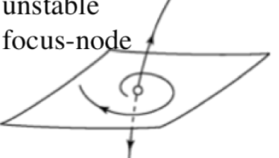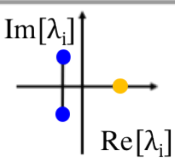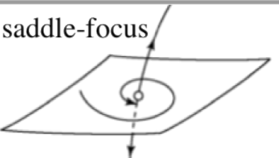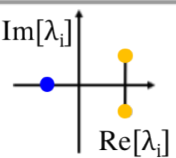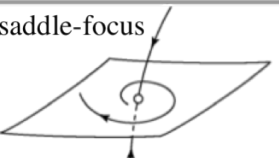
Eigenvalues	Phase portrait	Eigenvalues	Phase portrait
$Im[\lambda_i]$ / $Re[\lambda_i]$	stable node	$Im[\lambda_i]$ / $Re[\lambda_i]$	unstable node
$Im[\lambda_i]$ / $Re[\lambda_i]$	saddle	$Im[\lambda_i]$ / $Re[\lambda_i]$	saddle
$Im[\lambda_i]$ / $Re[\lambda_i]$	stable focus-node	$Im[\lambda_i]$ / $Re[\lambda_i]$	unstable focus-node
$Im[\lambda_i]$ / $Re[\lambda_i]$	saddle-focus	$Im[\lambda_i]$ / $Re[\lambda_i]$	saddle-focus

Figure 2.2. Hyperbolic equilibria in a 3-d phase space. "Eigenvalues", reporting the eigenvalues on the complex plane with blue dots for the stable case and yellow dots for the unstable case. "Phase portrait" reporting the system's trajectories in the phase space, corresponding to the specific equilibrium.
Adapted from *Scholarpedia: "Equilibrium"* by E. M. Izhikevich, 2007, Retrieved from *http://www.scholarpedia.org/article/Equilibrium*, licensed under a Creative Commons Attribution-NonCommercial-ShareAlike 3.0 Unported License, 2011.

2.3 Local and Global Bifurcations in Codimension 1 and 2

In this section, a practical understanding of bifurcations is introduced in a generic dynamical system. Bifurcation theory is a topic that has been widely investigated, either qualitatively or quantitatively, providing a well-developed mathematical background for the study of nonlinear dynamical systems. Bifurcation theory has its origin in the work of Poincaré [88], who introduced the concept of *branching* of solutions, corresponding to a new *phase object*, such as equilibria or cycles for instance, that appears into the phase portrait of the system when a parameter reaches the critical value. In this way, it is possible to classify bifurcations by matching qualitatively same phase objects. Later on, Andronov and colleagues (1930-1950), introduced the concept of *structural stability* of a dynamical system, for which bifurcations manifest themselves by inducing a qualitative change in the dynamical behaviour of the system, hence making the system *structurally unstable* at the bifurcation points in the parameter space [101].

In principle, for each bifurcation type, it is possible to define a *prototypical* system of equations, technically called *topological normal form*

$$\dot{\tilde{x}} = g(\tilde{x}, \beta),\ \tilde{x} \in \mathbb{R}^n,\ \beta \in \mathbb{R}^m, \tag{2.4}$$

having a bifurcation at $\tilde{x} = \tilde{x_0}$, for $\beta = \beta_c$, with β parameters vector and β_c critical parameters vector. The prototypical system 2.4 can be used to benchmark and classify bifurcations in any other generic system:

$$\dot{x} = f(x, r),\ x \in \mathbb{R}^n,\ r \in \mathbb{R}^m, \tag{2.5}$$

that is topologically equivalent near its critical equilibrium, (x_0, r_c), to the system 2.4. This means that system 2.5 must satisfy certain bifurcation conditions at (x_0, r_c) of system 2.4 at $(\tilde{x_0}, \beta_c)$.

Those conditions are called *genericity conditions*, specified together with the normal forms, in order to define uniquely the bifurcation types of the equilibria; they assume the form of nonequalities of certain partial derivatives of the function $f(x, r)$ with respect to coordinates and parameters evaluated at the critical point (x_0, r_c). The genericity conditions can be divided into *nondegeneracy conditions*, when involving partial derivatives with respect to the coordinates, and *trasversality conditions*, when the partial derivatives are performed with respect to the parameters. In other words, the nondegeneracy conditions provide the number and stability of the equilibria when the parameters change, while the transversality conditions show the possible ways to change the hyperbolicity of the equilibria by varying the parameters (*unfolding* the singularity), exhibiting all the bifurcations originating from the critical equilibria in presence of zero eigenvalues.

We can produce bifurcation diagrams where to depict the bifurcation types, by performing the *direct product* of the phase and parameter space $\mathbb{R}^n \times \mathbb{R}^m$. A bifurcation diagram consists of a finite number of regions in $\mathbb{R}^m$, divided by *bifurcation boundaries*[7], which delimit phase portraits of topologically equivalent systems. Intuitively, bifurcations happen when the system moves between such regions, crossing the boundaries.

The number of independent conditions that identify a bifurcation type and state the minimal number of parameters for which that bifurcation arises, determines the *codimension* (or shortly codim) of the bifurcation. The latter depends in turn on the dimensions of the parameter and phase space. Therefore, the number of bifurcations types, as well as the complexity of the bifurcation

---

[7]A bifurcation boundary originates when a new phase object shows up in the phase portrait, and the bifurcation conditions are satisfied

diagrams, increases as the codim increases. Providing a full list of all the possible bifurcations, especially in high-dimensional dynamical systems (e.g. $n > 3$), is impractical. For such a reason, in the next section, only the most significant bifurcations in codim-1 and codim-2, essential to develop our stability analysis for microresonators in Chapter 4 will be shown. We will also distinguish between *local bifurcations*, referring to bifurcations confined in a small neighbourhood of an equilibrium point, and *global bifurcations*, bifurcations that affect a larger portion of the phase space.

2.3.1   Codimension-1 Bifurcations

One of the simplest bifurcation in codim-1 is the *fold* bifurcation, also known as *saddle-node*[8] bifurcation, arising in 1D systems (n=1). A typical example of dynamical system in $\mathbb{R}^1 \times \mathbb{R}^1$ exhibiting a fold bifurcation is:

$$\dot{x} = r + x^2, \tag{2.6}$$

with Jacobian $J(x) = 2x$ and equilibrium solutions $x_0 = \pm\sqrt{-r}$, found by assuming $f = 0$. As it is shown in the diagram reported in Fig. 2.3 (a), when the parameter r is negative the function $f(x)$ has two equilibria, one stable and the other unstable (blue and yellow dots respectively). Indeed, the Jacobian shows a negative eigenvalue when x_0 is negative and a positive eigenvalue when x_0 is positive (see Fig. 2.3 (b)). As the parameter r increases from negative to positive values, the two equilibria move toward each other, collapsing in a single semi-stable equilibrium point at $x_0 = 0$ for the critical value $r_c = 0$, vanishing when $r > 0$ eventually. The fold bifurcation occurring at $(x_0, r_c) \equiv (0,0)$ provides a classic example of creations and destructions of equilibria, moreover, from the bifurcation diagram reported in Fig. 2.3 (c), we better appreciated the origin of name fold: as r approaches to zero the equilibrium curve "folds" manifesting a *turning point*.

The topological normal form $\mathbb{R}^1 \times \mathbb{R}^1$ of the system 2.6, having a fold bifurcation at $(x_0 = 0, r_c = 0)$, can be written as

$$\dot{\tilde{x}} = \beta \pm \tilde{x}^2, \tag{2.7}$$

---

[8]The term saddle-node derives from the terminology adopted for higher dimensional systems, where the equilibria vectors are called nodes and saddles.

with the following genericity conditions on the function f, defining the system 2.6:

$$f_{xx}(x_0, r_c) \neq 0, \tag{2.8a}$$

$$f_r(x_0, r_c) \neq 0, \tag{2.8b}$$

in which f_{xx} and f_r are the partial derivatives of f with respect to the variable x and the parameter r, respectively.
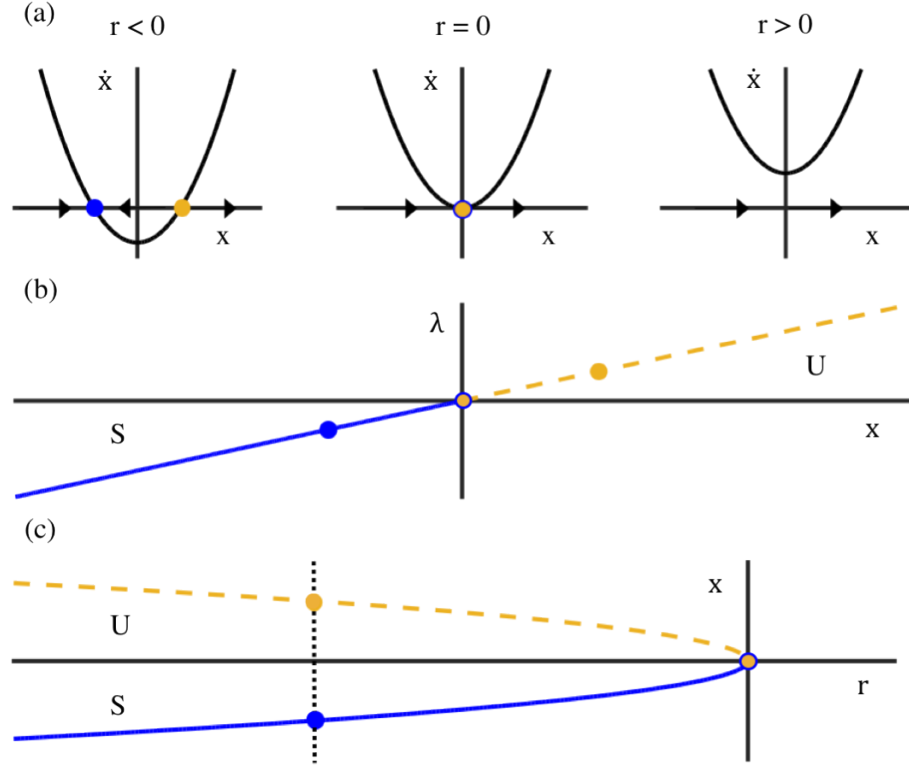
Figure 2.3. Example of fold bifurcation. (a) For $r < 0$ there are two equilibria in the system, represented by dots: the blue one is stable, while the yellow is unstable; the two equilibria approach each other as r approaches to zero, resulting in a "collision" between equilibria that ends generating an unstable equilibrium at $x = 0$. For $r > 0$ there are no equilibria in the system. (b) The stability of the equilibria can be apreciated by observing the sign of the eigenvalue by changing r. (c) The two equilibrium branches converge and annihilate in the folding point at $(x = 0, r = 0)$ (c).

Another fundamental codim-1 bifurcation is the *Andronov-Hopf* or simply *Hopf* bifurcation, observed, for instance in two-dimensional dynamical systems[9], represented by the following system of equations:

$$\begin{pmatrix} \dot{x} \\ \dot{y} \end{pmatrix} = \begin{pmatrix} \mu(r) & -\omega(r) \\ \omega(r) & \mu(r) \end{pmatrix} \begin{pmatrix} x \\ y \end{pmatrix} - (x^2 + y^2) \begin{pmatrix} x \\ y \end{pmatrix}, \tag{2.9}$$

---

[9] $\mathbb{R}^2$ is the lowest dimensional space required for Hopf bifurcatoins.

The equilibria of system 2.9 at $x_0 \equiv (x,y) = (0,0)$ for all the r values, with the Jacobian matrix evaluated at the origin

$$J(x_0) = \begin{pmatrix} \mu(r) & -\omega(r) \\ \omega(r) & \mu(r) \end{pmatrix}, \tag{2.10}$$

showing a pair of complex conjugate eigenvalues depending on the parameter r. The latter can be expressed in terms of two real functions, $\mu(r)$ and $\omega(r)$, such that $\lambda(r) = \mu(r) \pm i\omega(r)$. A Hopf bifurcation appears when the pair of eigenvalues becomes purely imaginary, i.e.: $\lambda = \pm i\omega$, as the parameter r reaches the critical value $r_c = 0$. Without loss of generality, we assume $\mu(r) = r$ and $\omega(r) = \omega_0$, with $\omega_0 > 0$ and plot the bifurcation diagram for the system 2.9 in Fig. 2.4.
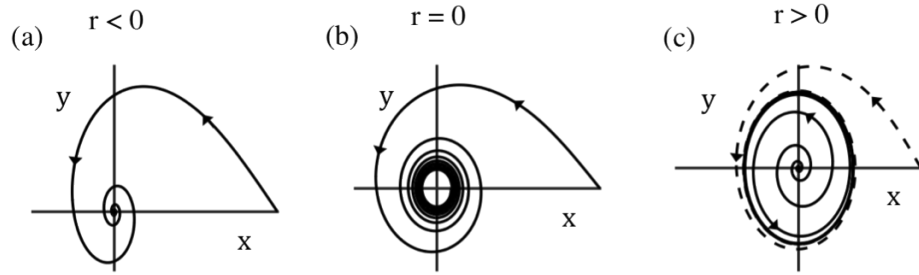
Figure 2.4. Supercritical Hopf bifurcations. The origin is an equilibrium point, which is a stable focus when $r < 0$ (a) and unstable when $r > 0$ (c). When $r = 0$ (b) a stable limit cycle appears surrounding the origin.

By studying the sign of the eigenvalue of $J(x_0)$, for negative values of the control parameter r, the equilibrium point $x_0 = (0,0)$ is linearly stable against small perturbations, hence nearby orbit in the system's phase portrait converge to x_0 moving along spiral trajectories (Fig. 2.4 (a)). In this case, x_0 is called *stable focus*. When the parameter $r < 0$ approaches the critical value $r_c = 0$, the orbits still converge to the equilibrium point but with a slower decay time; once the parameter reaches the critical value, the equilibrium is no longer linearly stable, and a stable *limit cycle* arises in the phase portrait (Fig. 2.4 (b)). Finally, for positive values of r, x_0 becomes an *unstable focus* (Fig. 2.4 (c)).

This scenario is known as *supercritical* Hopf bifurcation, which highlights the fact that a cycle appears "after" the bifurcation takes place for positive values of r. A system having a supercritical Hopf bifurcation shows stable self-sustained oscillations, whose period is related with the imaginary part of the complex pair of eigenvalues (ω_0), and size given by the real part of the eigenvalues. Stable limit cycles are an example of *periodic attractors*: their phase portrait is characterised by a periodic orbit, to which other nearby orbits, ϕ^t, converge.

If we change sign to the cubic terms of Eqs. 2.9, we have a *subcritical* Hopf bifurcation, shown in Fig. 2.5. In this case, an unstable limit cycle disappears as r becomes positive (hence the cycle

exists "before" the critical value r_c). In both cases, the system's equilibrium undergoes a change of stability when the real parts of the eigenvalues cross into the right half complex-plane as r changes from negative to positive values.
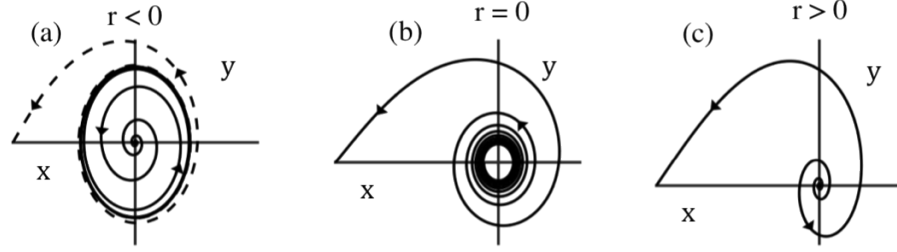
Figure 2.5. Subcritical Hopf bifurcation. The origin is an equilibrium point, which is a stable focus when $r < 0$ (a) and unstable when $r > 0$ (c). When $r = 0$ (c) an unstable limit cycle disappears.

Any generic system with domain in the space $\mathbb{R}^2 \times \mathbb{R}^1$, having a critical equilibrium point at $x_0 = (0,0)$ for $r = r_c$ and eigenvalues $\lambda = \mu(r) + i\omega(r)$, such that $\mu(r) = 0$ and $\omega(r) = \omega_0 > 0$ for $r = r_c$, is topologically equivalent to the normal form

$$\begin{pmatrix} \dot{\tilde{x}} \\ \dot{\tilde{y}} \end{pmatrix} = \begin{pmatrix} \beta & -1 \\ 1 & \beta \end{pmatrix} \begin{pmatrix} \tilde{x} \\ \tilde{y} \end{pmatrix} + \sigma(\tilde{x}^2 + \tilde{y}^2) \begin{pmatrix} \tilde{x} \\ \tilde{y} \end{pmatrix}, \tag{2.11}$$

in a neighbourhood of $\tilde{x} = x_0$, with $\sigma = \pm 1$, if the following genericity conditions are satisfied:

$$l_1(r_c) \neq 0, \tag{2.12a}$$

$$\mu_r(r_c) \neq 0. \tag{2.12b}$$

The nondegeneracy condition 2.12a defines whether a Hopf bifurcation is supercritical ($l_1(r_c) < 0$) or subcritical ($l_1(r_c) > 0$); its sign matches with the sign of σ [101, 102]. $l_1(r_c)$ is a combination of second and third terms of the Taylor series, resulting from a linearisation procedure to obtain the normal form Eqs.2.11. The transversality condition 2.12b requires that the eigenvalues cross the imaginary axis with non-zero speed.

A well-known example of a system showing Hopf bifurcation is the predator-prey model, described by the Lotka–Volterra equations [103]. Such a dynamic is common in many other systems, such as nerve cells (Rinzel and Ermentrout [104]), aeroplane wings (Thompson, Stewart [105]) and fluid flows (Drazin and Reid [106]).

The fold and Hopf bifurcation are examples of local bifurcations, in which equilibrium points appear, disappear or change their stability. Then, there are other types of bifurcations that involve entire orbits, which develops outside a neighbourhood of the equilibrium, covering large regions on the phase space, and connecting different equilibrium points. We refer to the latter as global bifurcations, such as *homoclinic* and *hetorclinc*, being the most important. Those occur when an attractor collides with an equilibrium point or, in general, when stable and unstable manifolds of equilibria intersect. In particular, we focus on homoclinic bifurcations involving nonhyperbolic equilibrium, as their presence characterises complex dynamics in laser systems and nonlinear passive cavities, including microresonators. Homoclinic and heteroclinic orbits or *connections* can be formally defined by considering a continuos-time dynamical system, same as Eq. 2.1. Assume x_0, x_1 and x_2 equilibria of the system:

- an orbit Γ_0 starting at a point $x \in \mathbb{R}^n$ is called *homoclinic* to the equilibrium x_0 if $\phi^t x \to x_0$ as $t \to \pm\infty$;

- an orbit Γ_0 starting at a point $x \in \mathbb{R}^n$ is called *heteroclinic* to the equilibria x_1 and x_2 if $\phi^t x \to x_1$ as $t \to -\infty$ and $\phi^t x \to x_2$ as $t \to +\infty$.

In Fig. 2.6, an example for $n = 3$ of homoclinic (a) and heteroclinic (b) orbits connecting equilibrium points is reported.
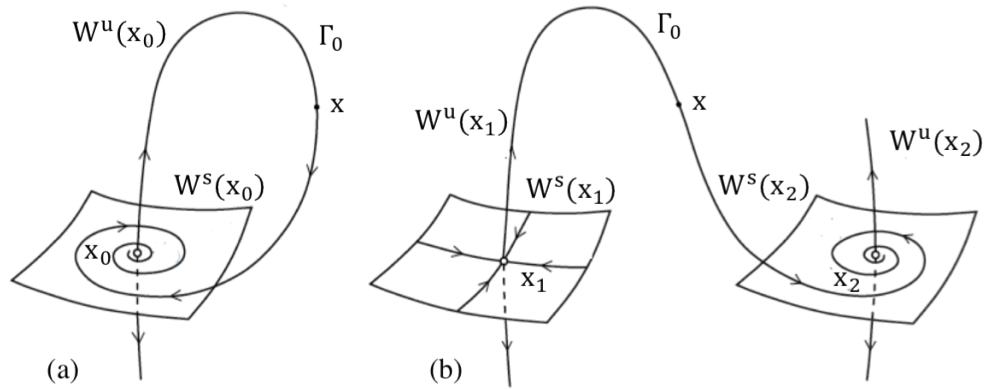
Figure 2.6. Homoclinic and heteroclinic orbits Γ_0 in $\mathbb{R}^3$. A homoclinic orbit to a saddle-focus in (a), while a heteroclinic orbit connecting a saddle and a focus in (b). Note that Γ_0 belongs to the intesection of a stable (W^s) and an unstable manifold (W^u).
Adapted from: *Elements of Applied Bifurcation Theory* (pp. 196), by Y. A.Kuznetsov, 2004, New York, NY, Springer Science. Copyright 2004 by Springer.

Here, we observe the presence of stable and unstable sets, $W^s(x_i)$ and $W^u(x_i)$[10], respectively, where Γ_0 belongs to their intersection. $W^s(x_i)$ and $W^u(x_i)$ are called *invariant sets*[11], which allow to rigorously generalise the concepts on bifurcations in low-dimensional systems to high-dimensional systems.

In this regards, let's consider a dynamical system, depending on one parameter in $\mathbb{R}^3$

$$\dot{x} = f(x,r),\, x \in \mathbb{R}^3,\, r \in \mathbb{R}^1. \tag{2.13}$$

Suppose a critical equilibrium point $x_0 = \{0,0,0\}$ at $r_c = 0$, having a simple zero eigenvalue and no other eigenvalues on the imaginary axis. System 2.13, under the genericity conditions 2.8 defined for fold bifurcations, can be represented in the following topological equivalent form near (x_0, r_c)

$$\begin{cases} \dot{\tilde{x}}_1 = b\tilde{x}_1{}^2, \\[2mm] \dot{\tilde{x}}_2 = \sigma_2\tilde{x}_2, \\[2mm] \dot{\tilde{x}}_3 = \sigma_3\tilde{x}_3, \end{cases} \tag{2.14}$$

in which σ_2 and σ_3 are the signs of the real parts of the nonzero eigenvalues, while $b \neq 0$, generically.

Depending on the signs of the the eigenvalues, we have different equilibria generated by a correspondent bifurcations:

1. $\sigma_2 = -1$ **and** $\sigma_3 = -1$

   fixing $b > 0$, we find two stable eigenvalues in the left-half complex plane. Therefore, the stable set $W^s(x_0)$ is the half-space $\tilde{x}_1 \leq 0$, while the unstable set $W^u(x_0)$ is the half-axis $\tilde{x}_1 \geq 0$. The non-hyperbolic equilibrium produced is called *saddle-node* (see Fig. 2.7 (a));

2. $\sigma_2 = 1$ **and** $\sigma_3 = 1$

   if we fix $b > 0$, we find two unstable eigenvalues in the right-half complex plane. Therefore, this case is analogous to the previous one, the only difference is that stable set $W^s(x_0)$ is the half-axis $\tilde{x}_1 \leq 0$, while the unstable set $W^u(x_0)$ is half-space $\tilde{x}_1 \geq 0$. The non-hyperbolic equilibrium produced is called a *saddle-node* (see Fig. 2.7 (b));

3. $\sigma_1 = 1$ **and** $\sigma_2 = -1$

   if we fix $b > 0$, we find one stable eigenvalue in the left-half complex plane and one

---

[10]$W^s(x_0) = \{x : \phi^t x \to x_0, t \to +\infty\}$, $W^u(x_0) = \{x : \phi^t x \to x_0, t \to -\infty\}$.
[11]An invariant set of a dynamical system $\{T, X, \phi^t\}$ is a subset $W \subset X$ such that $x_0 \in W \Rightarrow \phi^t x_0 \in W$ for all $t \in T$.

unstable eigenvalue in the right-half complex plane. In this case, the two manifolds are two-dimensional half-planes that intersect transversally. The non-hyperbolic equilibrium produced is called *saddle-saddle* (see Fig. 2.7 (c)).
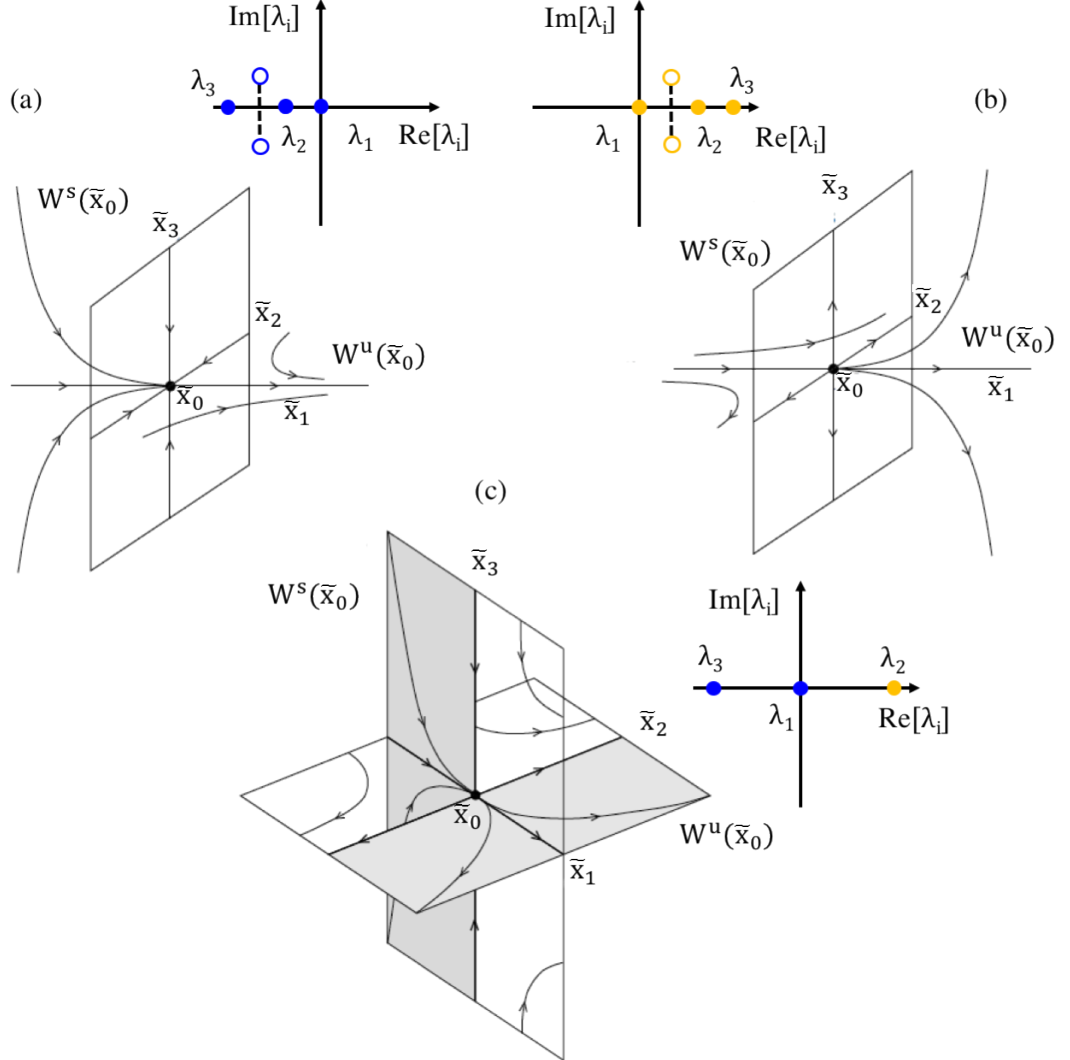
Figure 2.7. Nonhyperbolic saddle-node equilibria ((a) and (b)) and a saddle-saddle equilibria (c)in $\mathbb{R}^3$. Those bifurcatoins arise when an eigenvalue becomes zero, satisfying the fold bifurcation genericity conditions. The two non-zero eigenvalues in (a) and (b) can be either reals or complex conjugates. In the latter case, the orbits converge to the equilibrium by spiralling.
Adapted from: *Elements of Applied Bifurcation Theory* (pp. 254,255), by Y. A.Kuznetsov, 2004, New York, NY, Springer Science. Copyright 2004 by Springer.

Near the origin, the equivalent topological normal form of system 2.13, depending on the parameter is the following:

$$\dot{\tilde{x}} = \beta(r) + b(r)\tilde{x} + \mathcal{O}(\tilde{x}^3).\tag{2.15}$$

Thus, in the first and second case, as the parameter r approaches to $r_c = 0$, an hyperbolic saddle and a three-dimensional node disappear (appear) for $b(0)\beta(0){>}0$ ($b(0)\beta(0){<}0$) through a *saddle-node*

bifurcation; in the third case, two topological different saddles disappear (appear) for $b(0)\beta(0){>}0$ ($b(0)\beta(0){<}0$), when the parameter r reaches zero, through a *saddle-saddle bifurcation*.

Assume that the system 2.13, showing a saddle-node or, alternatively, a saddle-saddle equilibrium x_0 at $r_c = 0$ is topologically equivalent to the normal form 2.15; if there is an orbit Γ_0 homoclinic to the saddle-node or, alternatively, to the saddle-saddle, then a limit cycle appears when the equilibrium disappears. These bifurcations are called *saddle-node homoclinic* or *saddle-saddle homoclinic* bifurcation, respectively. This is the statement of the Shilnikov Theorem [107]. Such bifurcations are example of global bifurcation that originate from local bifurcations (specifically fold-bifurcation). An illustration of the bifurcations is reported in Fig. 2.8.

For sake of completeness, the Shilnikov theorem describes homoclinic bifurcations involving hyperbolic saddles or saddles-foci as well. Differently from the previous case, here the fold bifurcation does not occur, rather, homoclinic orbits can bifurcate simply because there is a topological change of the system's phase space, which is due to perturbation induced by varying $\beta(r)$. Indeed, homoclinic orbit to hyperbolic equilibria are structurally unstable.
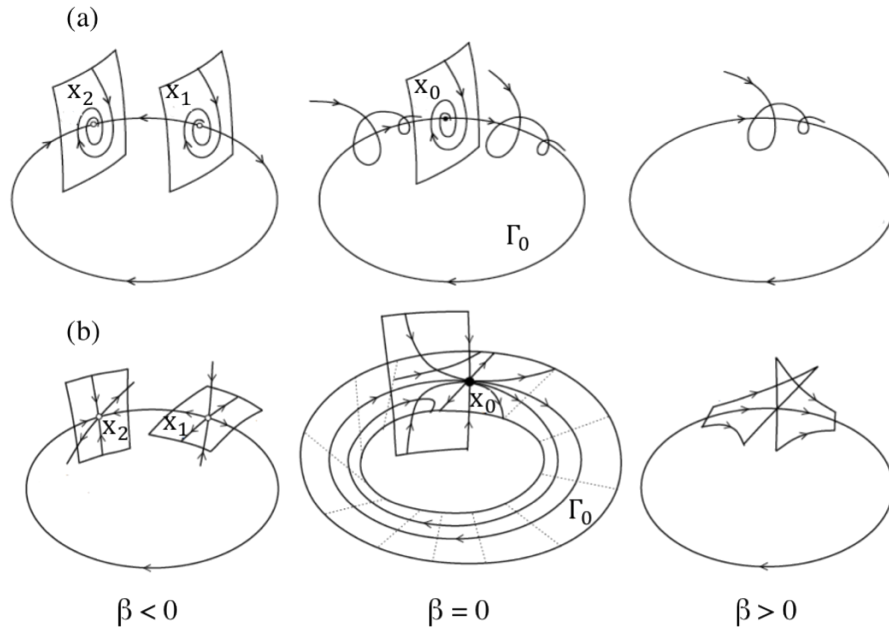
Figure 2.8. A homoclinic "Shilnikov" bifurcation occurs when a homoclinic orbit is nearby a saddle-node (a) or a saddle-saddle nonhyperbolic equilibrium. A limit cycle appears (stable in (a), saddle in (b)) after the equilibria disappears by varying $\beta(r)$.
Adapted from: *Elements of Applied Bifurcation Theory* (pp. 256,258), by Y. A.Kuznetsov, 2004, New York, NY, Springer Science. Copyright 2004 by Springer.

2.3.2 Codimension-2 Bifurcations

In this subsection, I will illustrate a codim-2 bifurcation. For the purpose, consider a two-parameter one-dimensional system having an equilibrium at $x = x_0$, which satisfies the fold bifurcation conditions for $r = r_c$ (single zero eigenvalue). Then, there exist an equilibrium curve $\Gamma \subset \mathbb{R}^1 \times \mathbb{R}^2$ intercepting the point (x_0, r_c), whose equilibrium points $(x, r) \in \Gamma$ satisfy the fold bifurcation conditions. The projection of Γ onto the plane (r_1, r_2) provides the bifurcation boundaries of the fold bifurcation, γ_B (see Fig. 2.9).
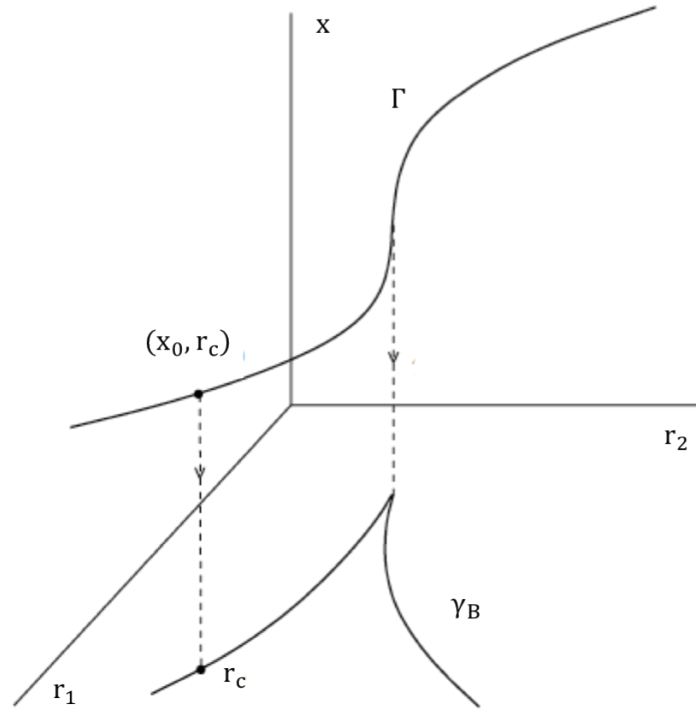
Figure 2.9. Bifurcation curve $\Gamma \subset \mathbb{R}^3$ of a scalar system (x, r_1, r_2), originating from critical equilibrium points that satisfy specific bifurcation conditions. The projection γ_B of Γ onto the plan (r_1, r_2) defines bifurcation boundaries. Adapted from: *Elements of Applied Bifurcation Theory* (pp. 296), by Y. A.Kuznetsov, 2004, New York, NY, Springer Science. Copyright 2004 by Springer.

Equivalently, if we consider a two-parameter two-dimensional system, having the equilibrium $x = x_0$ satisfying the condition for a Hopf bifurcation at $r = r_c$, for some pair of purely imaginary eigenvalues, then there exist an equilibrium curve $\Gamma \subset \mathbb{R}^2 \times \mathbb{R}^2$, whose projection onto the plane (r_1, r_2), γ_B, provides the correspondent bifurcation boundaries of the bifurcation.

At this point, if either the fold or Hopf bifurcation conditions are satisfied at $x = x_0$ for $r = r_c$, then the system shows a *fold-Hopf bifurcation*, also known as *zero Hopf* or *saddle-node Hopf*. This

bifurcation occurs in dynamical systems where $n \geq 3$, as a zero and a purely imaginary pair of eigenvalues are required.

Consider a 3D system with two varying parameters

$$\dot{x} = f(x, r), \ x \in \mathbb{R}^3, \ r \in \mathbb{R}^2. \tag{2.16}$$

with a fold-Hopf bifurcation at $x_0 = (0, 0, 0)$ for $r_c = (0, 0)$. The normal form of the bifurcation assumes the following equations in cylindrical coordinates:

$$\begin{cases} \dot{\xi} = \beta_1 + \xi^2 + s\rho^2, \\ \dot{\rho} = \rho(\beta_2 + \theta\xi + \xi^2), \\ \dot{\phi} = \omega + \theta\xi, \end{cases} \tag{2.17}$$

in which the first two equations are independent from the third one, which describes a rotation around the ξ-axis. Thus, we can assume only the system of two equations for ξ and ρ:

$$\begin{cases} \dot{\xi} = \beta_1 + \xi^2 + s\rho^2, \\ \dot{\rho} = \rho(\beta_2 + \theta\varepsilon + \xi^2), \end{cases} \tag{2.18}$$

In a neighbourhood of x_0 ($\rho = 0$), the system has two equilibria for $\beta_1 < 0$:

$$(\xi_0^{1,2}, \rho_0^{1,2}) = (\mp\sqrt{-\beta_1}, 0), \tag{2.19}$$

originating from a generic fold bifurcation at $\beta_1 = 0$ and defying the boundary $S = (\beta_1, \beta_2) : \beta_1 = 0$ and the branches $S_+ \subset S : \beta_2 > 0$ and $S_- \subset S : \beta_2 < 0$. The latter equilibria can bifurcate when $\rho > 0$, generating a further equilibrium (node or saddle)

$$(\xi_0^3, \rho_0^3) = \left(-\frac{\beta_2}{\theta} + \mathcal{O}(\beta_2), \sqrt{-\frac{1}{s}\left(\beta_1 + \frac{\beta_2^2}{\theta^2} + \mathcal{O}(\beta_2^2)\right)} \right), \tag{2.20}$$

defying the boundary $H = \left\{(\beta_1, \beta_2) : \beta_1 = -\frac{\beta_2^2}{\theta^2} + \mathcal{O}(\beta_2^2)\right\}$. In Fig. 2.10 the bifurcation diagram is represented, corresponding to the normal form 2.18 for $s - 1$ and $\theta > 0$, reporting the bifurcation boundaries γ_B. In the diagram, as we move clockwise around the origin, in the plane (β_1, β_2), we have a stable focus in (1), generated from the branch S_+. Then, crossing the β_1-axis, the system

undergoes a Hopf bifurcation originating a stable limit cycle in a small neighbour of x_0 in (2). Such a cycle grows as we move clockwise in (β_1, β_2), until reaching the boundary of the neighbourhood of x_0, corresponding to a further that originates the branch J. Once crossed J, from (2) to (3), the limit cycle becomes invisible from the inner of the neighbourhood of x_0, a phenomenon known as *cycle blow-up*. Then, in the region (4), crossing the branch S^- from (3) to (4), we have the birth of two nodes and a saddle. The same scenario can be observed in the region (6), crossing the branch S^+, from (1) to (6) (anti-clockwise). In (5), we can appreciate a stable and an unstable node, defined by the branches H_- and H_+ of H. Therefore H represents a *pitchfork* bifurcation, where three equilibrium points are created.
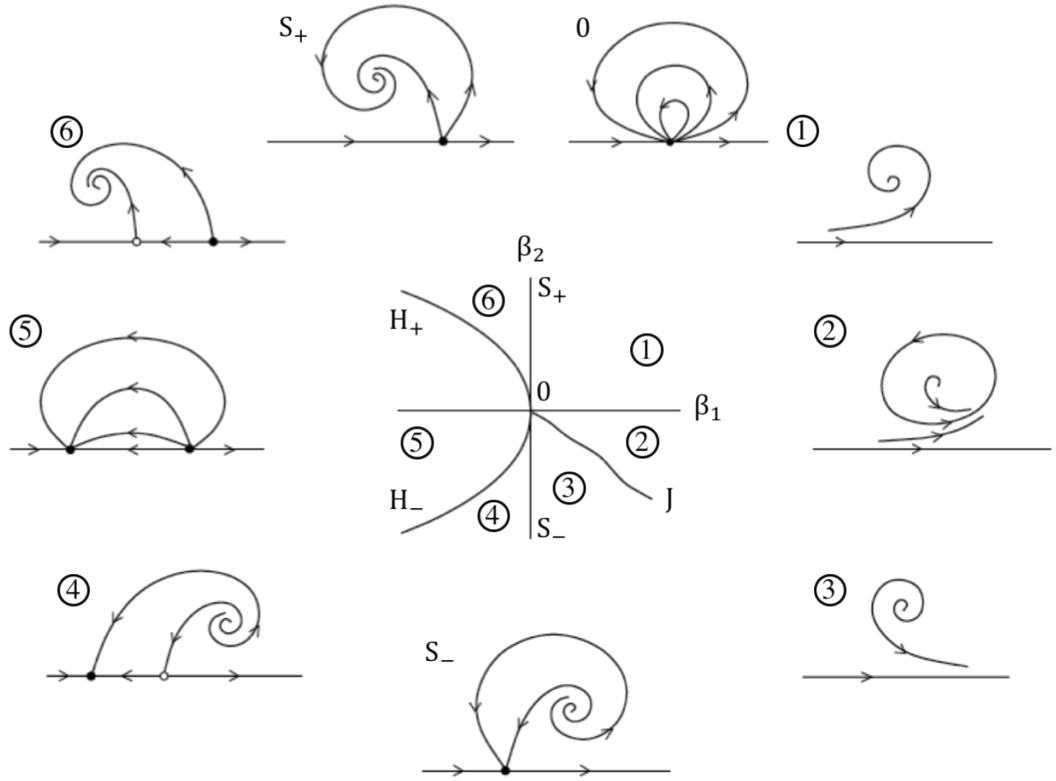
Figure 2.10. Fold-Hopf bifurcation diagram for $s = -1$, and $\theta > 0$. An example of fold-Hopf bifurcation generating different equilibrium branches is reported. By moving onto the plane (β_1, β_2), we observe the birth and death of a limit cycles (*blow-up*) and a pitchfork bifurcation.
Adapted from: *Elements of Applied Bifurcation Theory* (pp. 343), by Y. A.Kuznetsov, 2004, New York, NY, Springer Science. Copyright 2004 by Springer.

In conclusion, in this chapter, I have summarised some theoretical concepts of dynamical system theory, which will support the results of our work shown in Chapter 4, in terms of stability and bifurcations of microcavities equilibrium solutions.

Chapter 3

Dynamical Model for Nonlinear Microcavities

3.1 Chapter Introduction

The coupled mode theory (CMT) is an efficient approach for describing the coupling between propagating modes in waveguiding structures, such as microresonators, with high accuracy in estimating the coupling coefficients and predicting the evolution of the optical fields. The CMT was initially developed in the 1950s in the context of microwave apparatus, for the study of electromagnetic devices [108–110]. Then, from the 1970s, has been expanded and tailored for optical devices as well. [31, 54, 111–171]. This classical theory in linear regimes [31, 110–144], has been generalised during the years to include nonlinear applications and describe quantum regimes.

One of the pioneers of the CMT was Pierce, who, in the 1950s, approached the problem of the interaction of electron beams and electromagnetic waves in tubes by developing a set of coupled differential equations [108]. In the same years, Miller's work provided a description of microwaves waveguides and passive devices [109], whose results were generalised by Louisell to treat tapered waveguide in 1955 [110]. In the following two decades, between the 1970s and 1990s. In particular, Marcuse [110, 112], Snyder [113, 114], Yariv and Taylor [31, 115], independently, developed a coupled-mode theory for optical waveguides. The latter achievement enabled the study of several systems, such as guided-wave optoelectronic [116–119] and fibre optical devices [120–124], multiple waveguide lenses [125, 126], phase-locked lasers array [127], grating waveguides and couplers [128, 129, 131, 132], nonparallel waveguiding structures [111, 133–141], polarisation

rotation in optical fibres [142–144]. Later on, the CMT has been generalised to study the wave coupling in medium with a nonlinear response, such as second harmonic generation in bulk structures [145], waveguides [146] and resonant cavities [54, 147–149], as well as to describe nonlinear soliton propagation [150, 151] and modulation of instabilities in fibre [152].

Nonclassical phenomena, like squeezed states of the light [167] and quantum statistical properties of optical fields involving parametric processes in nonlinear optical couplers [168], have been studied using the approach of the coupling of modes, including, more recently, quantum proprieties of optical structures using a Hamiltonian framework of the CMT [170–172]. In early formulations, the CMT equations were obtained from energy balancing considerations; the first attempt to a rigorous formulation was developed by Schelkunoff [173], who showed that Maxwell's equations, with certain boundary conditions, can be reduced to the set of equations describing the voltage and current into coupled transmission lines, called "Telegraphist's Equations". Such an approach, based on the expansion of orthogonal modes of the uncoupled system, was known as conventional *orthogonal* coupled mode theory (OCMT), which allows obtaining the coupling coefficients unequivocally once the boundary conditions on the modes are defined. While studying optical couplers, Chen and Wang [153] highlighted the limited accuracy of the OCMT. Then, Hardy and Streifer [154] introduced a *nonorthogonal* formulation of the coupled-mode theory (NCMT), arguing that it reproduced, with more accuracy than the OCMT, the same results for dispersion curves and field patterns for the modes of parallel coupled waveguides. What emerged from such a debate during those years was that a strong power nonorthogonality could modify the nature of the coupling and, hence, the interaction among cavity modes. Following that, several reformulations of the conventional OCMT had been developed until 1987, when Haus and co-author introduced a formal approach that resolved almost all the discrepancies between the OCMT and the NCMT [157]. They showed that the coupling of the modes in space [149, 157] and in time [54, 149] could be obtained considering the unknown fields of the coupled system as a superposition of the known fields of the uncoupled system (trial fields) on which applying a variational principle to determine the best approximation of the coefficients of the expansion. In some works, it has been also demonstrated that there exists a unique procedure to orthogonalise the power of the modes, which reproduces the previous results of the OCMT. A few years later, a self-consistent NCMT using the reciprocity theorem was presented by Chuang [161] as well.

In this chapter, I will derive the CMT equations using a variational principle in Section 3.2, in the same fashion as the approach proposed by Haus [149]. Then, I will extend the equations to the

case of nonlinear dielectric materials. In Section 3.3, I will explicitly show the model equations to describe the fields propagation in an optical microcavity, in presence of third-order nonlinearities.

3.2 Coupled Mode Theory in Time

Haus and co-workers derived the nonorthogonal coupled mode equations in space using a variational principle, for linear and lossless waveguides [157]. The NCTM is more general than the OCMT and overcomes its limitation when the trial modes cannot be chosen being orthogonal, for instance when they belong to different reference structures.

Let's start from the Maxwell's equations describing the electromagnetic complex fields propagation in a lossless, non-homogeneous medium with a linear dielectric tensor ε, in general. By neglecting any magnetization of the material, we can write

$$\begin{cases} \nabla \times \mathbf{E} + \mu_0 \partial_t \mathbf{H} = 0, \\ \nabla \times \mathbf{H} - \partial_t \mathbf{D} = 0, \end{cases} \tag{3.1}$$

in which μ_0 is the magnetic permeability of vacuum, $\mathbf{E}$ and $\mathbf{H}$ are the electric and magnetic fields, respectively, while $\mathbf{D}$ is the electric displacement field. Eqs. 3.1, combined together, provide the wave equation for the electric field in a medium ε

$$\nabla \times (\nabla \times \mathbf{E}) = -\mu_0 \partial_{\mathbf{t}}^2 \mathbf{D}. \tag{3.2}$$

By Fourier transforming the fields[1], we obtain

$$\mathbf{E}(\mathbf{r},t) = \frac{1}{2\pi} \int \tilde{\mathbf{E}}(\mathbf{r},\omega) \exp^{-i\omega t} d\omega, \tag{3.3}$$

$$\mathbf{D}(\mathbf{r},t) = \frac{1}{2\pi} \int \tilde{\mathbf{D}}(\mathbf{r},\omega) \exp^{-i\omega t} d\omega, \tag{3.4}$$

where $\tilde{\mathbf{E}}$ and $\tilde{\mathbf{D}}$ are the Fourier transforms of the complex fields $\mathbf{E}$ and $\mathbf{D}$, while ω is the wave frequency. Substituting Eqs. 3.3 and 3.4 into Eq. 3.2, we can write the wave equation in the frequency domain

$$\nabla \times (\nabla \times \tilde{\mathbf{E}}) = \mu_0 \omega^2 \tilde{\mathbf{D}}, \tag{3.5}$$

---

[1]$\mathbf{F}(\mathbf{r},t) = \frac{1}{2\pi} \int \tilde{\mathbf{F}}(\mathbf{r},\omega) \exp^{-i\omega t} d\omega$

where the displacement field $\tilde{\mathbf{D}}$ is defined as

$$\tilde{\mathbf{D}}(\mathbf{r}, \omega) = \varepsilon_0 \varepsilon(\mathbf{r})\tilde{\mathbf{E}}(\mathbf{r}, \omega) + \Delta\tilde{\mathbf{P}}(\mathbf{r}, \omega). \tag{3.6}$$

In the above expression, ε_0 is the permittivity of free space, $\varepsilon(\mathbf{r})$ describes the geometry of the "unperturbed" system and $\Delta\tilde{\mathbf{P}}$ takes into account all the perturbations from the ideal structure (e.g. the presence of an external waveguide for the coupling, imperfections of the resonator, dispersion of the refractive index), which may change the effective index of the modes and promoting to the modal coupling.

By performing the scalar product of Eq. 3.5 by $\mathbf{E}^*$, integrating both sides of such an equation over the volume V of the whole space and solving for ω^2, we reach

$$\omega^2 = \frac{\int \tilde{\mathbf{E}}^* \cdot \nabla \times (\nabla \times \tilde{\mathbf{E}})\mathrm{d}V}{\mu_0 \int \tilde{\mathbf{E}}^* \cdot \tilde{\mathbf{D}}\,\mathrm{d}V}. \tag{3.7}$$

Considering that the fields fade to zero at the infinite, and that there is no radiating power, we can integrate Eq. 3.7 over the volume surrounding the dielectric instead. This leads us to

$$\omega^2 = \frac{\int (\nabla \times \tilde{\mathbf{E}}^*) \cdot (\nabla \times \tilde{\mathbf{E}})\mathrm{d}V}{\mu_0 \int \tilde{\mathbf{E}}^* \cdot \tilde{\mathbf{D}}\,\mathrm{d}V}, \tag{3.8}$$

in which ω assumes the role of action functional of the fields, providing an estimation of the resonant frequencies of the cavity modes.

When $\Delta\tilde{\mathbf{P}} = 0$, that is the case of an unperturbed system, we can "easily" solve the eigenproblem associated to Eq. 3.5 and find the eigenvalues ω_i and the eigenvectors $\mathbf{e_i}$ of the $i-th$ mode of unperturbed system, which satisfies the following equations:

$$\nabla \times (\nabla \times \tilde{\mathbf{e}}_\mathbf{i}) = \mu_0 \omega_i^2 \tilde{\mathbf{d}}_\mathbf{i}. \tag{3.9}$$

The latter defines a set of trial fields $\tilde{\mathbf{e}}_\mathbf{i}$, with which we can expand $\tilde{\mathbf{E}}$ and $\tilde{\mathbf{D}}$ and approach the solution of the coupled-modes problem when $\Delta\tilde{\mathbf{P}} \neq 0$. Therefore, given a set of N trial modes, $\tilde{e}_i, \tilde{d}_i$, we assume the following ansatz

$$\tilde{\mathbf{E}} = \sum_{i=1}^{N} \tilde{a}_i(\omega)\tilde{\mathbf{e}}_\mathbf{i}, \tag{3.10}$$

$$\tilde{\mathbf{D}} = \sum_{i=1}^{N} \tilde{a}_i(\omega)\tilde{\mathbf{d}}_\mathbf{i}, \tag{3.11}$$

where $\tilde{a}_i$ are the modal amplitudes. By replacing Eqs. 3.10 and 3.11 into Eq. 3.8, one obtains

$$\omega^2 = \sum_{i,j=1}^{N} \frac{\tilde{a}_i^* k_{i,j} \tilde{a}_j}{\tilde{a}_i^* w_{i,j} \tilde{a}_j}, \tag{3.12}$$

where

$$w_{i,j} = \int \tilde{\mathbf{e}}_i^* \cdot \tilde{\mathbf{d}}_j \, dv, \tag{3.13}$$

and

$$k_{i,j} = \frac{1}{\mu_0} \int (\nabla \times \tilde{\mathbf{e}}_i^*) \cdot (\nabla \times \tilde{\mathbf{e}}_j) dV = \frac{1}{\mu_0} \omega_j^2 \int \tilde{\mathbf{e}}_i^* \cdot \varepsilon \cdot \tilde{\mathbf{d}}_j \, dV, \tag{3.14}$$

are the terms defining the matrices $\mathbf{W}$ and $\mathbf{K}$, respectively. Eq. 3.12 can also be expressed in matrix representation

$$\omega(\tilde{\mathbf{a}})^2 = \frac{\tilde{\mathbf{a}}^\dagger \mathbf{K} \tilde{\mathbf{a}}}{\tilde{\mathbf{a}}^\dagger \mathbf{W} \tilde{\mathbf{a}}}. \tag{3.15}$$

For lossless dielectrics, $\mathbf{W}$ is a Hermitian positive matrix, as $W = \tilde{\mathbf{a}}^\dagger \mathbf{W} \tilde{\mathbf{a}}$ represents the time-average energy, which is real, while $\mathbf{K}$ is the correction onto the energy that takes into account the coupling of modes, and it is Hermitian as well.

The variational principle states that the real path followed by the system during its evolution is a stationary point of the action functional integral (Eq. 3.12 or Eq. 3.15). Thus, we can differentiate the right hand side of Eq. 3.12 with respect to the amplitudes and phases of $\tilde{a}_j$, keeping $\tilde{a}_i^*$ fixed or, equivalently, by differentiating Eq. 3.12 with respect to the $\tilde{a}_i^*$, keeping $\tilde{a}_j$ fixed, and obtain the best estimation for ω

$$\omega^2 \mathbf{W} \tilde{\mathbf{a}} = \mathbf{K} \tilde{\mathbf{a}}. \tag{3.16}$$

According to the perturbation theory, we can assume that all the modes frequencies are located around a central frequency value ω_0. If we neglect the second-order deviations of ω from ω_0, we reach: $\delta\omega \approx (\omega^2 - \omega_0^2)/2\omega_0$. Then, we can look at $i\delta\omega$ as the result of the time derivative of an exponential function in the form: $\exp(i\delta\omega)t$, which defines the inverse Fourier transform of $\tilde{a}(\omega)$

$$\mathbf{a}(t) = \frac{1}{2\pi} \int \tilde{\mathbf{a}}(\delta\omega) exp^{-i(\delta\omega)t} d(\delta\omega), \tag{3.17}$$

from which we come to the variational formulation of the CMT equations in time:

$$\mathbf{W}\frac{d\mathbf{a}}{dt} = i\mathbf{H}\mathbf{a}, \tag{3.18}$$

where $\mathbf{H} = (\omega_0^2 \mathbf{W} - \mathbf{K})/2\omega_0$ assumes the role of a coupling matrix, providing the coupling coefficients that quantify the modes interaction, hence the rate of energy exchanged one another. $\mathbf{H}$ is a Hermitian matrix, as a direct consequence of the fact that both $\mathbf{W}$ and $\mathbf{K}$ are Hermitian matrices. The latter aspect confirms that the overall of energy of the system must be conserved, indeed, if we derive such an energy, W, with respect to the time and use Eq. 3.18, we can write

$$\frac{d}{dt}[\mathbf{a}^\dagger \mathbf{W}\mathbf{a}] = i[\mathbf{a}^\dagger \mathbf{H}\mathbf{a} - \mathbf{a}^\dagger \mathbf{H}^\dagger \mathbf{a}] = 0. \tag{3.19}$$

3.3 Coupled Mode Theory for a Cavity with Kerr and Thermo-Optical Effect

The microresonators' ability of strongly enhancing the optical field triggers different nonlinear effects and leads to noteworthy dynamical regimes. Bi-stability, self-pulsing (SP) and chaotic regimes can be observed at low powers [1, 5]. The key role is played by slow and fast nonlinearities and their interaction. A possible way of controlling the overall behaviour, in order to achieve a desirable output, has been the main goal of this work.

In such a defined scenario, we exploit the approach of the CMT developed in the previous section to derive a suitable model of equations to study nonlinear dynamics in a microcavity-based oscillator, exhibiting both Kerr and an intensity-dependent nonlinearity, with a first-order time response.

3.3.1 Presence of Kerr Effect

Let's consider the electric displacement field, which takes into account the effect of the polarisation of the material as a response to an electric field $\mathbf{E}$

$$\mathbf{D}(\mathbf{r},t) = \varepsilon_0 \mathbf{E}(\mathbf{r},t) + \mathbf{P}(\mathbf{r},t), \tag{3.20}$$

where $\mathbf{P}(\mathbf{r},t)$ is the polarisation vector that, generally, is a nonlinear function of the electric field in a nonlinear medium. We can express the overall polarisation field $\mathbf{P}$ as

$$\mathbf{P}(\mathbf{r},t) = \mathbf{P_0}(\mathbf{r},t) + \Delta\mathbf{P}(\mathbf{r},t), \tag{3.21}$$

in which $\mathbf{P_0}$ is the polarisation of the unperturbed system, while $\Delta\mathbf{P}$ takes into account either linear perturbation on the resonator, such as coupling waveguides, or nonlinear contributions

$$\Delta\mathbf{P}(\mathbf{r},t) = \mathbf{P_L}(\mathbf{r},t) + \mathbf{P_{NL}}(\mathbf{r},t). \tag{3.22}$$

In this regards, we assume that the resonator is ideal, scalar, isotropic, dispersionless, with a third-order nonlinear response, i.e. Kerr materials, neglecting second-order nonlinear optical effects. For the purpose of this work, we neglect also third-harmonic generation. Therefore, we can write

$$\begin{cases} \mathbf{P}_L(\mathbf{r},t) = \varepsilon_0 \Delta\chi(\mathbf{r})\mathbf{E}(\mathbf{r},t), \\ \mathbf{P}_{NL}(\mathbf{r},t) \approx \frac{3}{4}\chi^{(3)}(\mathbf{r})|\mathbf{E}(\mathbf{r},t)|^2\mathbf{E}(\mathbf{r},t), \end{cases} \tag{3.23}$$

where $\Delta\chi$ considers external linear perturbation and material imperfections, while $\chi^{(3)}$ is the third order susceptibility [174]. As trial solution, we consider a superposition of orthogonal modes of the uncoupled system, defined as

$$\mathbf{E}(\mathbf{r},t) = \sum_i A_i a_i(t)\mathbf{e}_i(\mathbf{r}), \tag{3.24}$$

where $A_i = \sqrt{2/\varepsilon_0 n_i^2 V_i}$ are normalisation coefficients, in which V_i is the mode volume of the $i-th$ mode; it represents the space filled by the field profile inside the resonator, and it is defined as

$$V_i = \int ||\mathbf{e}_i(\mathbf{r})||^2 \mathrm{d}V. \tag{3.25}$$

n_i is the effective refractive index of the $i-th$ mode $\mathbf{e_i}$

$$n_i^2 = \frac{\int \varepsilon(\mathbf{r})||\mathbf{e}_i(\mathbf{r})||^2 \mathrm{d}V}{\int ||\mathbf{e}_i(\mathbf{r})||^2 \mathrm{d}V}. \tag{3.26}$$

Moreover, we suppose that the amplitudes $a_i(t)$ are slowly-varying functions of time. By using the ansatz Eq. 3.24, we can introduce a generalization of the CMT equations 3.18 for nonlinear medium [175, 176]

$$\frac{da_i(t)}{dt} = -\frac{1}{4}\sqrt{\frac{2}{\varepsilon_0 n_i^2 V_i}} \int \partial \frac{\Delta\mathbf{P}}{\partial t} \cdot \mathbf{e}_i^* e^{i\omega_i t} \mathrm{d}V, \tag{3.27}$$

in which ω_i represents the frequency of the $i-th$ mode. We can analyse the linear and nonlinear contribution of the vector $\Delta\mathbf{P}(\mathbf{r},t)$ separately. When the nonlinear term is neglected, we obtain an

equivalent form of the CMT equations 3.19

$$\frac{da_i(t)}{dt} = \sum_l \Gamma_{il} a_l(t) e^{i(\omega_i - \omega_l)t} + \zeta, \tag{3.28}$$

where the exponential function $e^{i(\omega_i - \omega_l)t}$ removes all the modes of frequency ω_l with a large phase mismatch. The term ζ represent the coupling of the cavity with the input evanescent modes (though input coupling). Γ_{il} are the overlap tensors, given by

$$\Gamma_{i,l} = \frac{i\omega_l}{2} \int \frac{\Delta \chi(\mathbf{r})}{n_i n_l} \mathbf{e}_l \cdot \mathbf{e}_i^* \frac{dV}{\sqrt{V_l V_i}}, \tag{3.29}$$

which evaluate the losses of the mode due to the output coupling. If there is no interaction with other modes, the equation 3.28 reduces to

$$\frac{da_i(t)}{dt} = -\frac{1}{\tau_{ph}} a_i(t) + \sqrt{\frac{2}{\tau_e}} E_{in} e^{-i(\omega_i - \omega_{in})t}, \tag{3.30}$$

where ω_{in} is the external pump frequency and E_{in} its amplitude, τ_{ph} represents the photon lifetime, related with the linear coupling; τ_{ph} depends on either intrinsic losses, due to the resonator itself, or extrinsic losses, τ_e, because of the coupling geometry of the cavity. From τ_{ph} we can determine the amount of energy transferred through the coupling and define the bandwidth of the resonance: $\delta_\omega = 2/\tau_{ph}$. The field at output of the microcavity for every mode can be written as

$$E_i = E_{in} e^{i(\omega_i - \omega_{in})t} - \sqrt{\frac{2}{\tau_e}} a_i, \tag{3.31}$$

whose intensity is mediated by extrinsic losses, τ_e. Assuming a critical coupling of the microcavity, the internal losses are equal to the coupling losses, hence $\tau_{ph} = \tau_e/2$. It worthwhile pointing out that the intra-cavity fields are expressed in $[J]^{1/2}$, while the external coupled fields are in $[W]^{1/2}$. When we consider the nonlinear contribution of $\Delta \mathbf{P}$ into Eq. 3.27, we obtain

$$\frac{da_i(t)}{dt} = \sum_{k,l,q} \Gamma_{iq}^{kl} a_k(t) a_l(t) a_q(t)^* e^{i(\omega_i + \omega_q - \omega_k - \omega_l)t}, \tag{3.32}$$

with Γ_{iq}^{kl} nonlinear tensor expressed as

$$\Gamma_{i,q}^{k,l} = i(\omega_k + \omega_l - \omega_1) \frac{3}{4\varepsilon_0} \int \frac{\chi(\mathbf{r})^3 \mathbf{e}_k \mathbf{e}_i^* \cdot \mathbf{e}_l \cdot \mathbf{e}_q^*}{n_k n_i n_l n_q \sqrt{V_k V_i V_l V_q}} dV. \tag{3.33}$$

The CMT assumes that all the modes of a cavity have frequencies that remain very close to their natural value ω_0, which, in other words, means that the theory assumes quasi-degenerate modes in the spatial domain for those belonging to the same mode family i.e. $\mathbf{e}_i \approx \mathbf{e}_{i_0}$. This approximation can be used in our framework, because the phase mismatch $\omega_i + \omega_q - \omega_k - \omega_l$, which leads the energy exchange among modes, prefers modes that satisfy the condition: $\omega_i + \omega_q - \omega_k - \omega_l \approx 0$, for efficiency reasons. Therefore, considering that the nonlinear susceptibility $\chi^{(3)}$ is constant over the mode volume, and that the refractive indices are degenerate, Eq. 3.33 becomes

$$\Gamma_{i_0} = i\omega_i \frac{3}{4} \frac{\chi^{(3)}}{\varepsilon_0 n_0^4} \frac{\int ||\mathbf{e}_{i_0}||^4 dV}{\left[\int ||\mathbf{e}_{i_0}||^2 dV\right]^2} = i\omega_i \frac{n_2 c}{n_{i_0}^2 V_{eff}}, \tag{3.34}$$

with the Kerr refractive index $n_2 = 3\chi^{(3)}/(4\varepsilon_0 c n_0^2)$, and V_{eff} the effective volume of the cavity, defined as: $V_{eff} = V_{i_0}^2 \left[\int ||\mathbf{e}_{i_0}||^4 dV\right]^{-1}$.

At this point, we suppose both linear and nonlinear contributions of $\Delta\mathbf{P}$. Therefore, we replace Eq. 3.34 into Eq. 3.32, then we combine Eqs. 3.30 and 3.32 to obtain, finally, the CMT equations for nonlinear medium

$$\begin{aligned}\frac{da_i(t)}{dt} = &-\frac{1}{\tau_{ph}}a_i(t) + \delta_{i,i_0}\sqrt{\frac{1}{\tau_{ph}}}E_{in}e^{i(\omega_{i_0}-\Omega_{in})t} \\ &+ \Gamma_{i_0}\sum_{k,q,l}\delta_{i+q-l-k}a_k(t)a_l(t)a_q^*(t)e^{i(\omega_i+\omega_q-\omega_l-\omega_k)t}.\end{aligned} \tag{3.35}$$

Eqs. 3.35 takes into account an external coupling with a continuous-wave source, with power $|E_{in}|^2$, coupled into the mode ω_{i_0} of the microcavity. Moreover, we also consider a laser detuning shift, Ω_{in}, with respect to the central value of frequency ω_{i_0}, thus an effective pump frequency: $\omega_{in} = \omega_{i_0} + \Omega_{in}$. The laser detuning introduces terms into the equations depending explicitly on the time. In order to remove this dependence, we assume ω_{in} as reference frequency, and express the modal fields with respect to an equidistant frequency grid: $a_i = \breve{a}_i \exp[i(\omega_i - \omega_{in})t] = \breve{a}_i \exp[i(\omega_i - \omega_{i_0} - \Omega_{in})t]$. Replacing the latter equation into Eq. 3.35, we finally achieve the coupled-mode equations for a nonlinear microcavity

$$\begin{aligned}\frac{d\breve{a}_i(t)}{dt} = &i\Omega_{in}\breve{a}_i(t) - \frac{1}{\tau_{ph}}\breve{a}_i(t) \\ &+ i\Gamma_{i_0}\sum_{j,l,m}\delta_{i+l-m-j}\breve{a}_j(t)\breve{a}_m(t)\breve{a}_l^*(t) + i\frac{1}{\sqrt{\tau_{ph}}}\delta_{i0}\breve{S}_{in}.\end{aligned} \tag{3.36}$$

The third term on the right-hand side of Eq. 3.36 describes the mixing of four different photons due to the Kerr nonlinearity, while $\check{S}_{in}$ is the external field amplitude appropriately rescaled.

3.3.2 Thermo-Optical Effect

Coupled mode theory can also be efficiently used to model different types of nonlinearity, such as thermo-optical effect. When a laser pumps energy into a microcavity, it can act as an internal heat source, producing a strong increase of the temperature due to the small mode volume and high-Q factor. The intensity of the propagating optical field can reach values above $1\text{GW}/cm^2$ [175]. The generated heat propagates through the bulk of the resonator and then to the surroundings. This phenomenon has an effect on the refractive index, which is temperature dependent, and manifest itself with a shift of the WGMs and a variation of the free spectral range of the cavity. Therefore, we need to consider an additional terms of detuning into the Eqs. 3.36 that we define as $\varepsilon_T(t)$, which is dependent on the energy coupled into the resonator. In a first approximation, it can be expressed with a first-order decay equation as the following

$$\tau_T \frac{d\varepsilon_T}{dt} = -\varepsilon_T + Q_T, \tag{3.37}$$

where τ_T is a decay constant that models the thermal dissipation of the system, while Q_T represents the heating of the resonator, which is proportional to the total inner energy

$$Q \propto \sum_i |a_i|^2. \tag{3.38}$$

By inserting Eq. 3.37 in 3.27, and properly setting $\omega_{in} = \omega_{i_0} + \Omega_{in}$ we obtain the full set of CMTs including the thermal detuning of the cavity resonances

$$\begin{aligned}
\frac{d\check{a}_i(t)}{dt} &= i\Omega_{in}\check{a}_i(t) + i\Omega_T\check{a}_i(t) - \frac{1}{\tau_{ph}}\check{a}_i(t) \\
&+ \iota\Gamma_{i_0} \sum_{j,l,m} \delta_{i+l-m-j}\check{a}_j(t)\check{a}_m(t)\check{a}_l^*(t) + i\frac{1}{\sqrt{\tau_{ph}}}\delta_{i_0}\check{S}_{in},
\end{aligned} \tag{3.39}$$

$$\tau_T \frac{d\Omega_T}{dt} = \Gamma_T \sum_k |\check{a}_k(t)|^2 - \Omega_T, \tag{3.40}$$

in which

$$\Gamma_T = i\omega_i \frac{n_2^T c}{n_{i_0}^2 V_{eff}}, \tag{3.41}$$

where n_2^T is the thermo-optic refractive index, controlling the slow nonlinear detuning rate, while τ_T is its decay time.

3.3.3 Derivation of the Model for Kerr Microcavities with a Thermo-Optical Nonlinearity

We consider the coupling of two external fields, $\check{S}_p$ and $\check{S}_s$, that we refer as pump and signal, with frequencies ω_p and ω_s, respectively. Eqs 3.39 and 3.40 are suitable to model a nonlinear microcavity subjects to the Kerr and thermo-optical effects.

In third-order materials, the Kerr nonlinearity generates self-phase modulation (SPM) and cross-phase modulation (XPM), two nonlinear effects arising because of the dependence of the refractive index from the intensity of the propagating electric fields. SPM is responsible of a self-induced phase shift of the individual optical fields $\check{S}_p$ and $\check{S}_s$ meanwhile they are propagating, while XPM manifests itself with a phase shift of the the individual optical field, $\check{S}_p$, due to the presence of $\check{S}_s$ and vice versa. The overall phase shift experienced by the fields can be quantified as: $\Delta\phi_{p,s} \propto (|\check{S}_{p,s}|^2 + 2|\check{S}_{s,p}|^2)$, in which the first term is related with SPM, while the second one depends on the XPM. From the previous equation for phase shift, we note that, given equally intense optical fields, the amount of shift due to XPM is twice that of SPM. In terms of conservation of energy ω_i must be equal to ω_f, so that, to observe SPM or XPM, one of the following conditions must be satisfied:

$$\omega_{p,s} + \omega_{p,s} = \omega_{p,s} + \omega_{p,s}, \text{ for SPM,}$$

$$\omega_p + \omega_s = \omega_p + \omega_s, \text{ for XPM.}$$

We anticipate that, the model that we are developing in this chapter will be initially applied to the case of degenerate four-wave mixing (FWM), where two photons of the pump laser with frequency ω_p interact with one photon of the signal at frequency ω_s, to generate the idler's photon at $\omega_{id}^{l,r}$. The apexes l and r state for "left" and "right" idler, or in other words, generated at lower or at higher frequency with respect to the pump frequency ω_p (down-conversion or up-conversion), respectively). Following the conservation of energy, this process must satisfy the conditions: $2\omega_p = \omega_s - \omega_{id}^l$ or $2\omega_s = \omega_p - \omega_{id}^r$, with ω_s and $\omega_{id}^{l,r}$ symmetrically distributed with respect to the central pump frequency, ω_p, as depicted in Fig. 3.1 (a). Then, we will also take into account higher order FWM terms generation, specifically, up to the presence of a secondary idler, whose frequency must satisfy the condition: $\omega_p + \omega_s = \omega_{id}^l - \omega_{id}^r$, as shown in Fig. 3.1 (b).
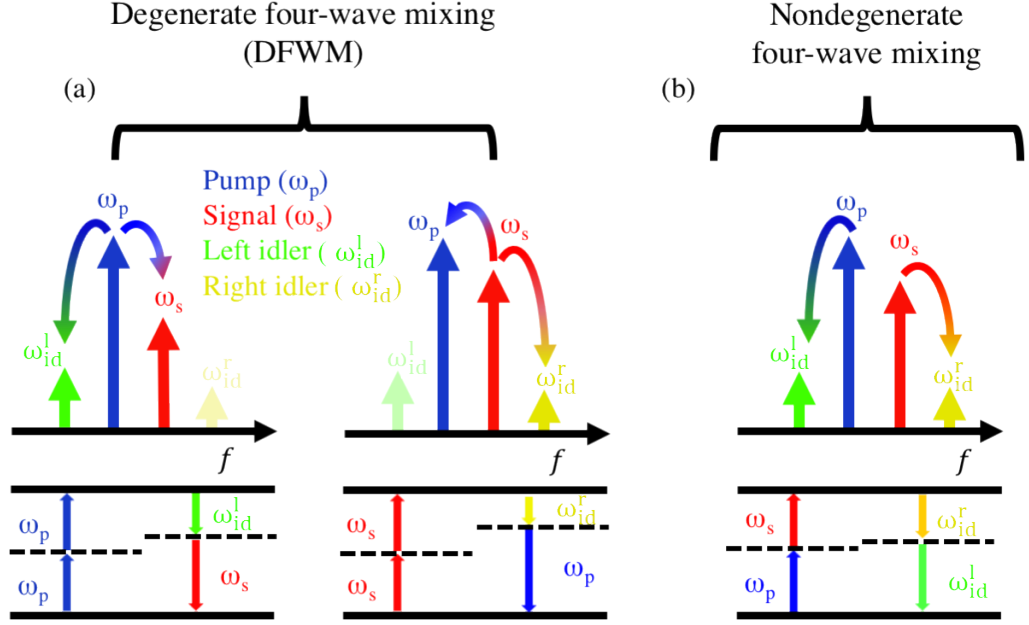
Figure 3.1. Examples of four-wave mixing processes. (a) Degenerate four-wave mixing in which two photon of the pump ω_p, interacting with the nonlinear material, are converted in one photon of the signal ω_s and in one photon of the idler ω_{id}^l, respectively. In the same manner, two photon of the signal ω_s are converted in one photon of the pump ω_p and in one photon of the idler ω_{id}^r, respectively. (b) The FWM can generate a secondary idler, in the specific one photon of the pump ω_p and one photon of the signal ω_s, through nonlinear interactions with the medium, are converted in one photon of the left idler ω_{id}^l and in one photon of the right idler ω_{id}^r, respectively.

Under the above conditions, assuming the coupling of four different intra-cavity fields, a pump ($\breve{a}_p$), a signal ($\breve{a}_s$), a primary idler ($\breve{a}_{id}^l$) and a secondary idler ($\breve{a}_{id}^r$) due to the external coupled fields, $\breve{S}_p$ and $\breve{S}_s$, the CMT Eqs. 3.39 and 3.40 can be explicitly written as

$$\frac{d\breve{a}_p}{dt} = -\left[i\Omega_p + \tau_{ph}^{-1} + i\Omega_T - i\Gamma_K(|\breve{a}_p|^2 + 2|\breve{a}_s|^2 + 2|\breve{a}_{id}^l|^2 + 2|\breve{a}_{id}^r|^2)\right]\breve{a}_p$$
$$+ \Gamma_K(2\breve{a}_p^*\breve{a}_s\breve{a}_{id}^l + \breve{a}_s^2\breve{a}_{id}^{r*} + 2\breve{a}_s^*\breve{a}_{id}^r\breve{a}_{id}^l) - i\tau_{ph}^{-1/2}\breve{S}_p, \tag{3.42}$$

$$\frac{d\breve{a}_s}{dt} = -\left[i\Omega_s + \tau_{ph}^{-1} + i\Omega_T - i\Gamma_K(|\breve{a}_s|^2 + 2|\breve{a}_p|^2 + 2|\breve{a}_{id}^l|^2 + 2|\breve{a}_{id}^r|^2)\right]\breve{a}_s$$
$$+ \Gamma_K(2\breve{a}_s^*\breve{a}_p\breve{a}_{id}^r + \breve{a}_p^2\breve{a}_{id}^{l*} + 2\breve{a}_p^*\breve{a}_{id}^r\breve{a}_{id}^l) - i\tau_{ph}^{-1/2}\breve{S}_s, \tag{3.43}$$

$$\frac{d\breve{a}_{id}^l}{dt} = -\left[i\Omega_{id}^l + \tau_{ph}^{-1} + i\Omega_T - i\Gamma_K(|\breve{a}_{id}^l|^2 + 2|\breve{a}_p|^2 + 2|\breve{a}_s|^2 + 2|\breve{a}_{id}^r|^2)\right]\breve{a}_{id}^l$$
$$+ \Gamma_K(\breve{a}_p^2\breve{a}_s^* + 2\breve{a}_{id}^{r*}\breve{a}_p\breve{a}_s), \tag{3.44}$$

$$\frac{d\breve{a}_{id}^r}{dt} = -\left[i\Omega_{id}^r + \tau_{ph}^{-1} + i\Omega_T - i\Gamma_K(|\breve{a}_{id}^r|^2 + 2|\breve{a}_p|^2 + 2|\breve{a}_s|^2 + 2|\breve{a}_{id}^l|^2)\right]\breve{a}_{id}^r$$
$$+ \Gamma_K(\breve{a}_s^2\breve{a}_p^* + 2\breve{a}_{id}^{l*}\breve{a}_p\breve{a}_s), \tag{3.45}$$

$$\tau_T\frac{d\Omega_T}{dt} = \Gamma_T(|\breve{a}_p|^2 + |\breve{a}_s|^2 + |\breve{a}_{id}^l|^2 + |\breve{a}_{id}^r|^2) - \Omega_T. \tag{3.46}$$

where Ω_p, Ω_s, Ω_{id}^l and Ω_{id}^r are the detuning from the resonant frequencies of the pump, signal, primary and secondary idler respectively, while Γ_K is given by Eq. 3.34. It is helpful to introduce a dimensionless normalization of the temporal variable t against the photon lifetime τ_{ph}, hence $t\tau_{ph}$ provides the physical time in seconds. In order to obtain dimensionless equations, the optical amplitudes must be normalized with respect to the Kerr constant, by defining the set of intra-cavity amplitudes and external coupling amplitudes: $a_i(t) = \check{a}_i(t)\sqrt{\tau_{ph}\Gamma_K}$ and $S_i(t) = \check{S}_i(t)\sqrt{\tau_{ph}^2\Gamma_K}$, respectively. Finally, we obtain

$$\frac{da_i}{dt} = -a_i - i[\delta_i + \Delta - (2I_T - |a_i|^2)]a_i + iF_i - iS_i, \tag{3.47}$$

$$\sigma\frac{d\Delta}{dt} = -\Delta - \rho I_T, \tag{3.48}$$

in which (0) is the pump, (1) is the signal, (-1) the primary idler and (2) the secondary idler. $I_T = \sum_{k=0\pm1} I_k$ is the total cavity energy; $I_i = |a_i|^2$, $P_i = |S_i|^2$ and $\delta_i = \Omega_i\tau_{ph}$ are the normalized intra-cavity energies, the coupled powers and frequency detuning, respectively. Δ is the detuning due to the slow nonlinearity (thermo-optical), where $\sigma = \tau_T/\tau_{ph}$ is the normalised relaxation time; $\rho = \Gamma_T/\Gamma_K$ is the effective nonlinear coefficient normalised against the Kerr constant. The parameter σ depends on the quality factor and can be engineered. Crystalline high-Q resonators can easily have σ of the order of a few tens, while integrated resonators, with a lower Q-factor and a higher relaxation constant, can have σ up to several orders of magnitude. The values for ρ are usually in the range of one to three orders of magnitude and can exhibit both signs [5, 177, 178]. The FWM terms in the Eq. 3.47 are

$$F_0 = 2a_0^*a_1a_{-1} + a_1^2a_2^* + 2a_1^*a_2a_{-1}, \tag{3.49}$$

$$F_1 = 2a_1^*a_2a_0 + a_0^2a_{-1}^* + 2a_0^*a_2a_{-1}, \tag{3.50}$$

$$F_{-1,2} = a_{0,1}^2a_{1,0}^* + 2a_{2,-1}^*a_0a_1, \tag{3.51}$$

Therefore, in this chapter, the framework of the non-orthogonal coupled mode theory in time (Section 3.2) has been applied to model the special case of a homogeneous, anisotropic, dispersionless microresonator. A set of ordinary differential equations, which is a prototypical model for time-dependent nonlinearities, has been built; it describes the dynamics of the intra-cavity fields and providing a general understanding of a large class of devices, accurately reproducing the thermal relaxation in microcavities [1] with a time response τ_T and a nonlinear thermo-optical index Γ_T.

In the next chapter, I will discuss relevant results obtained by performing a numerical study in function of the fundamental parameter of the system, appreciating how the interaction among fast and slow nonlinearities can be opportunely adjusted to achieve a desired nonlinear regime.

Chapter 4

Analysis of Stability and Nonlinear Dynamical Regimes in Kerr Microcavities with a Thermo-Optical Nonlinearity

4.1   Chapter Introduction

Thermo-optic and Kerr effect can have a strong impact on the response of microresonators, for instance, they can induce a frequency shift of the resonant frequencies of the optical modes, affecting also the free spectral range of the cavity. Such nonlinear effects are related to a linear dependence of the refractive index on the optical intensity and they may have different origins and timescales. Whereas the Kerr effect arises from the interaction between the electric field and the medium, quantified by the third-order component of the nonlinear polarisation vector, the thermal effect is due to the self-heating of the cavity, enhanced by the strong confinement of the light inside the modes volume of a microresonator. In this manner, a propagating field acts as an internal source of heat, with the result that the cavity undergoes an increase of the temperature. Then, the generated heat is dissipated toward the surroundings until the system reaches an equilibrium. This results in a gradient of temperature within the confined inner region of the microresonator. Since the refractive index is temperature-dependent, the temperature gradient causes a further shift of the cavity resonances. Such an occurrence may contribute to thermo-optic instabilities, such as

self-pulsing (SP), as we will see in this chapter. We take into Kerr and thermo-optical nonlinearity, which are quantified in our model by their constants, Γ_K and Γ_T, respectively. The Kerr effect acts at atomic timescales, usually modelled as an instantaneous response. Conversely, other third-order nonlinearities, such as thermo-optical, opto-mechanical and free carrier, have a slower relaxation time compared to the Kerr response, as it has been seen in the introduction and in Chapter 1.

Here, we are focused on the interplay between the Kerr and thermo-optical nonlinearity, and in which way those influence the system's equilibrium stability, in order to implement a scheme that allows ruling desired dynamical regimes. Particularly, we consider a configuration in which a weak signal is meant to trigger and control the self-oscillatory behaviour of a strong pump coupled into a microcavity, considering the role of the four-wave mixing (FWM).

A dramatic change of the dynamics of a nonlinear system(e.g. an optical microcavity), usually matches a bifurcation of some equilibrium point in the parameter space. Therefore, we need to investigate the stability of the steady-state solutions of microresonators and the bifurcations of its equilibria, in order to determine the dynamical evolution of the system from an initial stationary state. The theoretical background defined in Chapter 2 and 3 will be applied to provide an analysis of the system's phase space and find bifurcations in the parameter space. Numerical techniques based on the Newton-Raphson continuation method [101] and a 5th order step-adaptive Runge-Kutta-Fehlberg method (see Appendix A.3) are suitable to propagate the coupled-mode theory (CMT) equations in time[1].

This chapter is organised as follows: in Section 4.2 I will apply a perturbative method to linearise the model equations 3.47 and 3.48, and obtain the perturbation matrix, whose eigenvalues define the stability of the steady state solutions for a system of coupled fields in an optical microcavity. Then, in Section 4.3, I will use the linearised model to describe the illustrative case of single-frequency coupling, determining analytic expressions for the boundaries separating different region of stability. I will also introduce the concept of the stability maps and bifurcation diagrams. The interplay between the thermo-optical and Kerr effect on the nonlinear response of a microcavity will be discussed in Section 4.4. The outcomes from Sections 4.3 and 4.4 will lay the basis to fully comprehend the case of two frequency coupling in Sections 4.5 and 4.6, where I will prove that the four-wave mixing, induced to the coupling of the signal, is fundamental in creating and reallocating bifurcations in the parameter space and changing the nature of the equilibria of the system, hence its dynamical evolution. Finally, in Section 4.7, I will provide a clear example

---

[1]MATLAB and MATCONT for the numerical continuation and bifurcation study of continuous and discrete parametrised dynamical system have been used. The codes are reported in Appendix A.

of switching between different operational regimes and transferring of dynamics between cavity modes, via FWM, including the case of chaotic states.

4.2   Linearisation of the Coupled Mode Equations

The system of equations 3.47 and 3.48 describes the time evolution of complex fields propagating into a microcavity. Hence, we can consider the field amplitudes and their correspondent complex conjugate counterparts such that the system can be written as:

$$
\begin{cases}
\frac{da_i}{dt} = -a_i - i[\delta_i + \Delta - (2I_T - |a_i|^2)]a_i + iF_i - iS_i, \\
\frac{da_i^*}{dt} = -a_i^* + i[\delta_i + \Delta - (2I_T - |a_i|^2)]a_i^* - iF_i^* + iS_i^*, \\
\sigma\frac{d\Delta}{dt} = -\Delta - \rho I_T.
\end{cases}
\tag{4.1}
$$

We remind the explicit expression of the terms appearing above: $F_0 = 2a_0^* a_1 a_{-1} + a_1^2 a_2^* + 2a_1^* a_2 a_{-1}$, $F_1 = 2a_1^* a_2 a_0 + a_0^2 a_{-1}^* + 2a_0^* a_2 a_{-1}$, $F_{-1,2} = a_{0,1}^2 a_{1,0}^* + 2a_{2,-1}^* a_0 a_1$ are the FWM terms, while $I_i = |a_i|^2$ and $P_i = |S_i|^2$ are the normalised intra-cavity energies and coupled powers, respectively. Moreover, $\rho = \Gamma_T/\Gamma_K$, while $\sigma = \tau_T/\tau_{ph}$.

Following the notation introduced in Section 2.2, Eqs. 4.1 represent a set coupled ODEs, where the vector-valued function is: $f : \mathbb{C}^9 \times \mathbb{R}^6 \to \mathbb{C}^{15}$, while the amplitude and parameter vectors are: $x = (a_0, a_0^*, a_1, a_1^*, a_{-1}, a_{-1}^*, a_2, a_2^*, \Delta)^T$ and $r = (\sigma, \rho, \delta_0, \delta_1, P_0, P_1)^T$, respectively. Then, let $x_0 = (A_0, A_0^*, A_1, A_1^*, A_{-1}, A_{-1}^*, A_2, A_2^*, D)$ be a steady state solution of the system and consider the following first-order perturbative ansatz

$$
\begin{cases}
a_i(t) = A_i + \delta a_i(t), \\
\Delta(t) = D + \delta\Delta(t),
\end{cases}
\tag{4.2}
$$

where $\delta a_i(t)$ and $\delta\Delta(t)$ are first-order perturbation terms, belonging to the perturbation vector $\varepsilon = (\delta a_0, \delta a_0^*, \delta a_1, \delta a_1^*, \delta a_{-1}, \delta a_{-1}^*, \delta a_2, \delta a_2^*, \delta\Delta)^T$. The latter is found solving the following linearised equation

$$
\frac{d\varepsilon}{dt} = M\varepsilon
\tag{4.3}
$$

where M is the perturbation matrix evaluated in x_0

$$M = \begin{pmatrix} \frac{\partial f_{a_0}}{\partial a_0} & \frac{\partial f_{a_0}}{\partial a_0^*} & \cdots & \frac{\partial f_{a_0}}{\partial \Delta} \\ \cdots & \ddots & & \\ \frac{\partial f_\Delta}{\partial a_0} & \frac{\partial f_\Delta}{\partial a_0^*} & \cdots & \frac{\partial f_\Delta}{\partial \Delta} \end{pmatrix} \qquad (4.4)$$

The linearisation theorem discussed in Section 2.2 allows to analyse the stability of the steady state solutions, by numerically solving the eigenvalues problem associated to the Jacobian matrix $M(x_0)$. Once worked out the eigenvalues for each equilibrium point, we can realise stability maps and study the bifurcations of the equilibrium curve by changing some parameters of the system.

Given a set of initial conditions, the system evolves from one initial steady state toward a final steady state, according with the equations, defining the time-parametrised phase portrait that we can numerically represent.

4.3   Single Frequency Continuous Wave Pumping

Assume an external field S_0 due to a single pump source, with frequency ω_0, coupled into a microcavity mode. The model of Eqs. 4.1, is reduced to the following system of two coupled ODEs

$$\begin{cases} \frac{da_0}{dt} = -a_0 - i[\delta_0 + \Delta - |a_0|^2]a_0 - iS_0, \\ \frac{da_0^*}{dt} = -a_0^* + i[\delta_0 + \Delta - |a_0|^2]a_0^* + iS_0^*, \\ \sigma\frac{d\Delta}{dt} = -\Delta - \rho|a_0|^2, \end{cases} \qquad (4.5)$$

The steady state solutions of Eqs.4.5 can be analytically found by solving the cubic equation

$$-iS_0 - ia_0(-i + \delta_0 - (1+\rho)|a_0|^2) = 0, \qquad (4.6)$$

from which we obtain the general set of solutions

$$a_0 = \left\{ \frac{\sqrt[3]{b}}{\sqrt[3]{2}3^{2/3}\eta_2} + \frac{\sqrt[3]{\frac{2}{3}}\eta_1}{\sqrt[3]{\zeta}}; -\frac{\left(1-i\sqrt{3}\right)\sqrt[3]{\zeta}}{2\sqrt[3]{2}3^{2/3}\eta_2} - \frac{\left(1+i\sqrt{3}\right)\eta_1}{2^{2/3}\sqrt[3]{3}\sqrt[3]{\zeta}}; -\frac{\left(1+i\sqrt{3}\right)\sqrt[3]{\zeta}}{2\sqrt[3]{2}3^{2/3}\eta_2} - \frac{\left(1-i\sqrt{3}\right)\eta_1}{2^{2/3}\sqrt[3]{3}\sqrt[3]{\zeta}} \right\},$$

$$\Delta = -\rho a_0,$$

$$(4.7)$$

with

$$\eta_1 = (-i + \delta_0), \ \eta_2 = (1 + \rho), \ \zeta = 9\chi_2^2 S_0 + \sqrt{3}\sqrt{27\chi_2^4 S_0^2 - 4\chi_2^3 \chi_1^3}.$$

In Fig. 4.1, for a value of $\rho = -10$, we represent the stationary resonances (Eq. 4.6), for two fixed values of pump power, $P_0 = 0.01, 0.1$, by varying the pump detuning δ_0 and the intra-cavity energy I_0. Comparing Fig. 4.1 (a) with (b), we qualitatively note that, when the energy is low (Fig. 4.1 (a)), the resonance exhibits the "classic" Lorentzian shape, due to the linear terms of Eq. 4.6. When the pumping is increased (Fig. 4.1 (b)), the optical circulating power increases in turn, thus the contribution of Kerr and thermo-optical nonlinearity will no be longer negligible. This results in a frequency "drifting" of the resonance with respect to the central value, giving rise to a "triangular" or "bent" shape that is typical observed from the measurements. Equivalently, the latter phenomenon arises when the bi-stable threshold is reached. Such a threshold indicates when the contribution of the nonlinear term of the Eq. 4.6 becomes competitive over the linear terms. This aspect will be discussed in detail in the next section, when we analyse the resonances shift in relation with the ρ coefficient, which depends on the microcavity material.
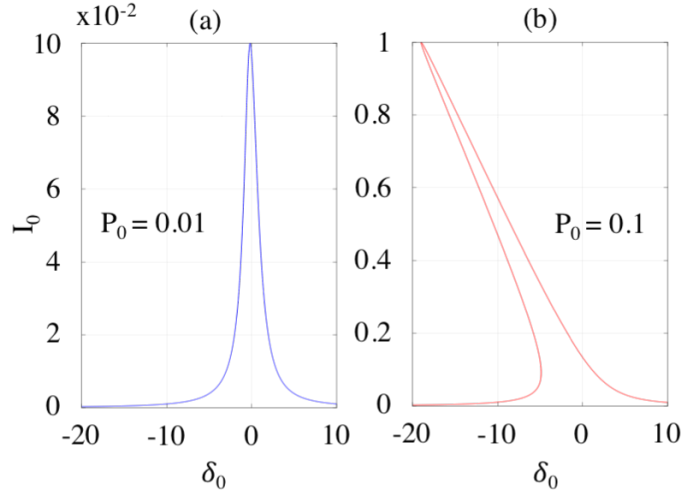
Figure 4.1. Comparison between stationary solutions at low and high power, in (a) and (b) respectively, with single pumping, by varying δ_0 and I_0, fixing P_0. When $P_0 = 0.01$ the shape of the resonance is a typical Lorentzian peak. At higher power in (b), with $P_0 = 0.1$, the shape is subject to a drift, which is due to the contribution of nonlinear terms.

By using the linearisation procedure, with the ansatz 4.2, we can write the terms of the Jacobian 4.4 as

$$
M = \begin{pmatrix}
-1 + i(2|a_0|^2 - \Delta - \delta_0) & ia_0^2 & -ia_0 \\
-ia_0^* & -1 - i(2|a_0|^2 - \Delta - \delta_0) & ia_0^* \\
-\rho \frac{a_0^*}{\sigma} & -\rho \frac{a_0}{\sigma} & -\frac{1}{\sigma}.
\end{pmatrix}
\tag{4.8}
$$

Then, we solve the characteristic equation $Det(M - \lambda I) = 0$, from which we may have one real and a complex pair of eigenvalues or three real eigenvalues, depending on the discriminant of the equation.

According to Section 2.2, if one of the real eigenvalues is positive at a specific equilibrium point, such an equilibrium is unstable; if all the real eigenvalues are negative, the equilibrium is stable. Instead, if there is a complex conjugate pair of eigenvalues with positive real parts, then the system shows periodic instability.

The condition that define the unstable boundaries is given by the equation: $Det(M) = 0$, corresponding to a simple zero eigenvalue of the matrix 4.8.

$$
I_0^{U,\pm} = \frac{2\delta_0 \pm \sqrt{\delta_0^2 - 3}}{3(\rho - 1)},
\tag{4.9}
$$

where $I_0^{U,+}$ represents the upper unstable boundary, while $I_0^{U,-}$ the lower one. By imposing $I_0^{U,+} = I_0^{U,-}$, we can work out the critical value of detuning for the U region, $\delta_c^U = \pm\sqrt{3}$, which depends on the sign of ρ. From the critical detuning we can estimate the bi-stability threshold:

$$
I_0^B = \pm \frac{\sqrt{3}}{3(\rho - 1)},
\tag{4.10}
$$

To obtain the expressions for the SP boundaries we impose the eigenvalues be in the complex form: $\lambda = \lambda_r) + i\lambda_i$ and substitute the latter expression into the characteristic equation for the determinant of Jacobian 4.8. Then, we separate the real from the imaginary contributions and impose $Re(\lambda_i) = 0$, such that we reach

$$
\begin{cases}
d_2\lambda_i^2 - d_0 = 0, \\
\lambda_i^2 - d_1 = 0,
\end{cases}
\tag{4.11}
$$

where d_0, d_1 and d_2 are combinations of the coefficient of M:

$$
\begin{cases}
d_0 = \frac{2+\sigma+\delta_0^2\sigma-4\delta_0 I_0^2\sigma+3I_0^4\sigma+2\delta_0 I_0^2\rho\sigma-4I_0^4\rho\sigma+I_0^4\rho\sigma}{\sigma}, \\
d_1 = \frac{\delta_0^2+4\delta_0 I_0\rho-4\delta_0 I_0+3I_0^2\rho^2-6I_0^2\rho+3I_0^2+1}{\sigma}, d_2 = \frac{2\sigma+1}{\sigma}.
\end{cases}
\tag{4.12}
$$

By solving Eq. 4.11 with respect to λ_i we reach the following relation between the coefficients: $d_0 = d_1 d_2$, from which obtaining the SP energy boundaries by means of Eqs. 4.12

$$
I_0^{SP,\pm} = \frac{\delta_0(2(2+\rho)\sigma-\rho)}{2(1+\rho)(\rho(\sigma-1)+3\sigma)} \pm \sqrt{\frac{\delta_0^2(2(2+\rho)\sigma-\rho)^2}{4(1+\rho)^2(\rho(\sigma-1)+3\sigma)^2} - \frac{1+\sigma(2+\sigma+\delta_0^2\sigma)}{\sigma(1+\rho)(\rho(\sigma-1)+3\sigma)}},
\tag{4.13}
$$

while the critical detuning value for the SP region is given by imposing $I_0^{SP,+} = I_0^{SP,-}$

$$
\delta_0^{SP} = \frac{2(1+\sigma)}{\rho-2\sigma}\sqrt{\sigma^{-1}(1+\rho)(\rho(\sigma-1)+3\sigma)}.
\tag{4.14}
$$
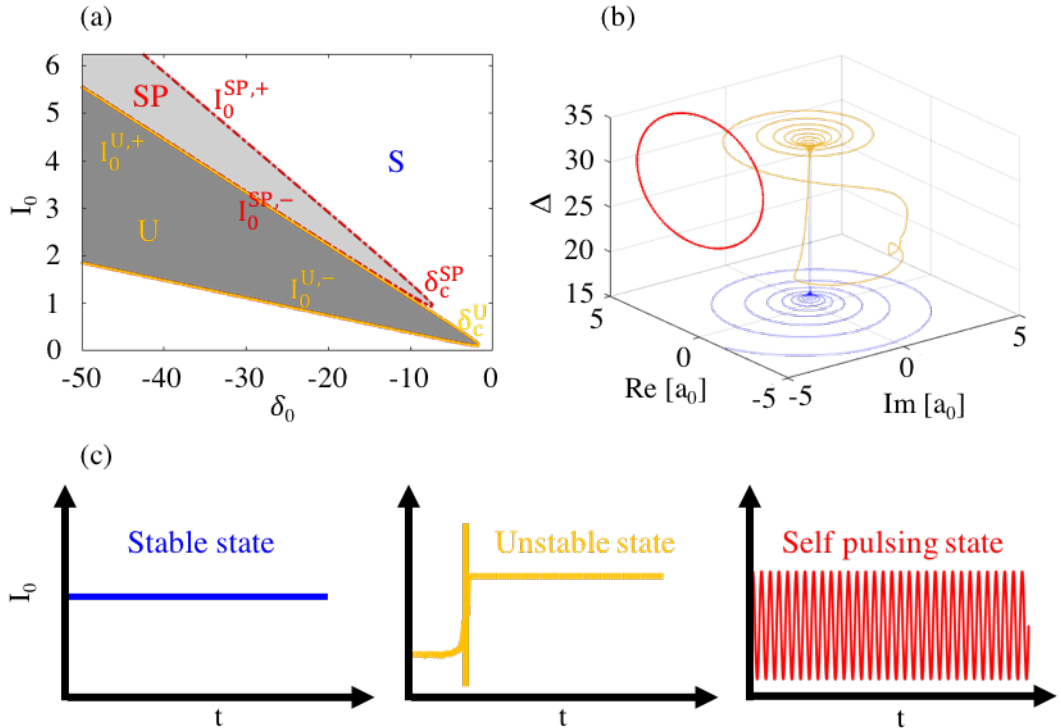
Figure 4.2. Stability map of equilibria (a) system's phase space (b) and dynamical evolution (c) of a set of steady state solutions, with $\sigma = 50$ and $\rho = -10$. The stable region is represented in blue (S), the unstable region in yellow (U) and the self-pulsing region (SP) in red. The analytic boundaries of U and S are obtained by plotting Eqs. 4.9 and 4.13 respectively. In (b) and (c), with the detuning is $\delta_0 = -15$, we can appreciate the phase portraits (b) and relative output in (c). They correspond to a stable focus in S, showing stationary output (blue line), an unstable saddle-node in U, having unstable output (yellow line), and a limit cycle in SP, with periodic solution (red line).

The analysis of stability carried out, resulting in the stability diagram or map (δ_0, I_0) represented in Fig. 4.2 (a), allow us to predict different dynamical regimes in a neighbour of the equilibria within the S, U and SP region. This is, indeed, reported in the phase portraits and in the response graph $I_0(t)$, shown in Fig. 4.2 (b) and (c) respectively. Here, it has been represented the time evolution from a stable solution in S (blue line), an unstable in U (yellow line) and a periodic one in SP (red line).The chosen values of $\sigma = 50$ and $\rho = -10$ in Fig. 4.2 consider a thermo-optic nonlinearity being 10 times larger than the Kerr one, with opposite sign, while a thermo-optical relaxation time being 50 times slower than the photon lifetime, allowing slow heat dissipation per round-trip. Such values are typical of bulk resonators, as microspheres or microrods [6, 179, 180]. The sign and magnitude of the thermo-optical coefficient depends on the material, such as density of material and polarizability, both connected to the temperature, hence to the strength of the electric field applied. For instance, CaF_2, BaF_2 and NaF have a negative thermo-optica coefficient, while for SiO_2, MgF_2 and Si is positive [180].
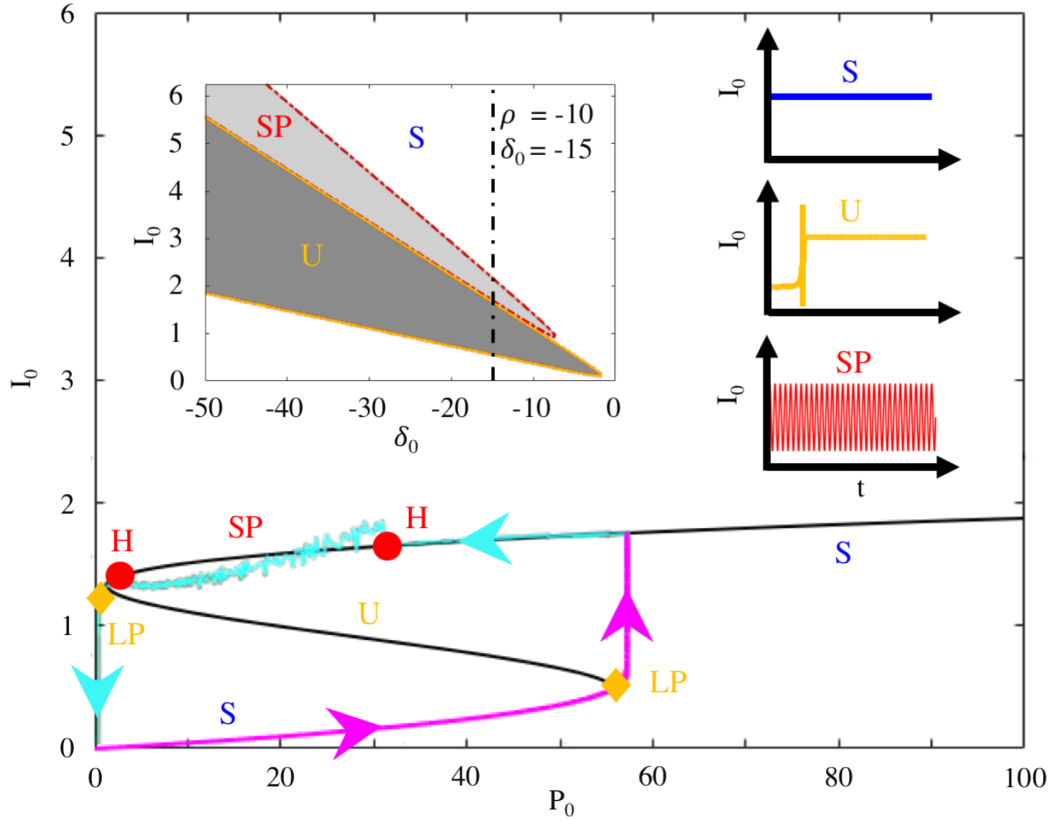
Figure 4.3. Bifurcation diagram reporting hysteresis response for $\sigma = 50$, $\rho = -10$ and $\delta_0 = -15$. The stable branch of the region S lies below the unstable branch within the region U, which is included between two limit points (fold bifurcations, LP). On the upper branch, Hopf bifurcations (H) delimit the region SP, where the system is self-stable. The hysteresis loop is shown first increasing, then decreasing the pump power.

The stability of the stationary solutions can change with the variation of a parameter of particular interest, also defined as active parameter (see Section 2.3). In order to show an example of bifurcations of the equilibria a bifurcation diagram has been realised in Fig. 4.2, considering the input pump power P_0 as active parameter and fixing $\delta_0 = -15$. The diagram (P_0, I_0) is reported in Fig. 4.3. The black line in Fig. 4.3 represents the steady-state curve: moving along the curve, from low to high powers (magenta path), we encounter, first the lower stable branch, then we switch to the upper stable branch without achieving the self-stable region, since the presence of the unstable branch. Conversely, from high to low powers (cyan path), we encounter, initially, the upper stable branch, then the self-stable branch and, finally, we switch to the lower stable branch. This is the effect due to the bi-stable nature of the system, manifesting with the phenomenon of *hysteresis*. The hysteresis loop is due to the presence of an unstable branch separating two stable branches. Here, in fact, for the same value of power P_0 there are two stable and one unstable solution for I_0. The particular state reached depends on how we previously pumped the cavity.

Now, we examine in details the eigenvalues of the system, defining the equilibrium curve (P_0, I_0) in Fig. 4.3 ($\sigma = 50$, $\rho = -10$ and $\delta_0 = -15$). In Fig. 4.4, the real and imaginary parts of the eigenvalues are plotted as a function of I_0. The critical values, where the system presents a bifurcation, are opportunely highlighted.

For low values of I_0, we have a complex pair of eigenvalues ($\lambda_{1,3}$, green line) with negative real parts and a real leading eigenvalue[2] λ_2 (black dashed), which is negative as well. This generates stable foci-nodes, for which nearby trajectories approaching them defining spirals in the 3D phase space (this can be clearly appreciated by looking at the blue curve in Fig. 4.2 (b)). Such equilibria belong to the region S in Fig. 4.2 (a). Then, a saddle-node bifurcation or limit point bifurcation (LP), appears at the critical value $I_0 = 0.55$, as the leading eigenvalue λ_2 is zero. Here, two new hyperbolic equilibria are generated, a focus and a saddle. In this case, any nearby trajectory moves away from the equilibrium along spirals, because of the complex pair $\lambda_{1,3}$, as represented in Fig. 4.2 (b) (yellow curve). These equilibria belong to the region U in Fig. 4.2 (a). For sake of clarity, it appears that the real part of the leading eigenvalue has opposite sign with respect to the real parts of the complex pair so that the bifurcation generates a homoclinic loop. However, if the conditions of the Shilnikov theorem are met (see Section 2.3), limit cycles are originated from the homoclinic orbits. Then, there is a second saddle-node bifurcation happening at the critical value $I_0 = 1.66$ where $Re(\lambda_2)$ becomes negative again. It is worthwhile to note that the region where we observe

---

[2]The eigenvalue with negative real part, closest to the imaginary axes are called *leading* eigenvalue.

bi-stability is delimited by two LP bifurcations. At the critical value $I_0 = 1.70$, the complex pair of eigenvalues, whose real parts becoming positive crossing the semi-half complex plan. This gives rise to a Hopf bifurcation, that we label with H and define the region SP in 4.2 (a). Here, the trajectories converge to the stable limit cycle, originated by the bifurcation and depicted with the red line in Fig. 4.2 (b). Thus, the output of the system has periodic oscillation, as reported in Fig. 4.2 (c). Finally, $I_0 = 2.16$ represents another critical point, where the real parts of $\lambda_{1,2,3}$ become negative, reaching stable steady states in the region S.
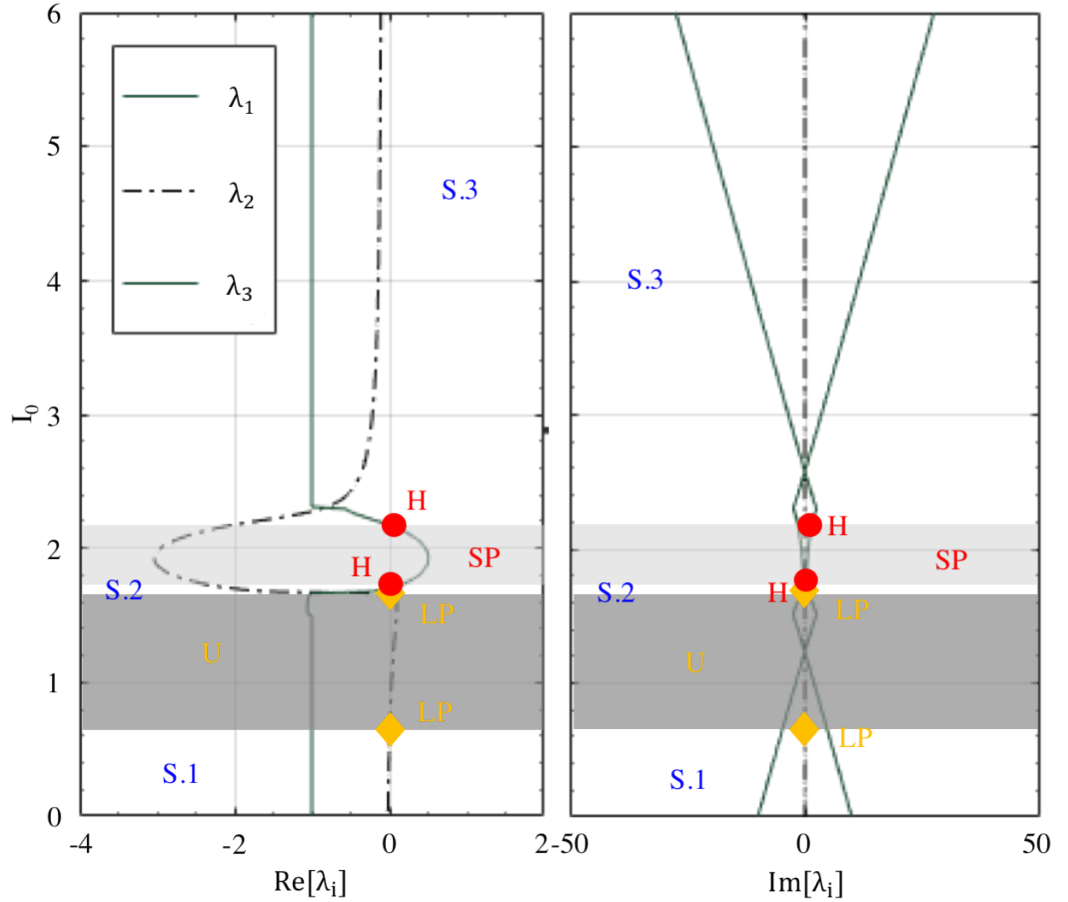
Figure 4.4. Real and imaginary parts of the eigenvalues of the Jacobian matrix 4.8 for $\sigma = 50$, $\rho = -10$, $\delta_0 = -15$, plotted as function of the intra-cavity energy I_0, in (a) and (b) respectively. The yellow marks state LP bifurcations, while the red dots correspond to Hopf ones. Initially, the real leading eigenvalue λ_2, (black dashed) is negative and the equilibria are stable foci in S. Then, the leading eigenvalue assumes positive values between $I_0 = 0.55$, and $I_0 = 1.66$, generating the unstable branch in U, included among LP bifurcations. Here, the equilibria are unstable a saddle-foci. Between the values $I_0 = 1.66$ and $I_0 = 1.70$, λ_2 is negative, thus we find again stable foci. At the critical value $I_0 = 1.70$, the complex pair of eigenvalues λ_1, λ_3 lead, having real positive parts. This produces the self-stable branch in SP, included between two Hopf bifurcations, H, at $I_0 = 1.70$, and $I_0 = 2.16$ respectively. At $I_0 = 2.16$, we have another critical point due to the negative part of λ_2, that produces stable foci in the region S.

4.4 Kerr Against the Thermo-Optic Effect

For practical purposes, the frequency of the pump laser needs to be adequately adjusted to take into account the drift of the resonances, due to the Kerr and the thermo-optic nonlinearity. We can numerically analyse this problem, by overlapping the stability maps with the nonlinear resonances curves. This situation is represented by the left graphs in Fig. 4.5 for $\sigma = 50$ and different values of $\rho = -10, 0, 10$, in (a), (c) and (e), respectively. Instead, in the right graphs of Fig. 4.5, we highlight the nature of the equilibria with respect to amount of pump power P_0, for the same values of σ and ρ, in (b), (d) and (f), respectively. The bent shapes of the nonlinear resonances quantify the overall shift that they undergo as P_0 is increased. For $\rho = -10$, the nonlinear terms globally produce a blue-shift (see Fig. 4.5 (a) and (b)). Therefore, if we set a negative detuning value, for instance $\delta_0 = -15$ (Fig. 4.5, black dashed line), we start from a stable solution on the negative slope of the resonance curve, then we reach an unstable point, finally, if the coupling is strong enough, we have either a stable or a self-pulsing solution located on the the positive slope.

When $\rho \to 0$, hence when the Kerr effect dominates over the thermo-optical effect, we observe a red-shift of the resonance the resonances in Fig. 4.5 (c,d). Similarly, in Fig. 4.5 (e,f), when $\rho = 10$. In both cases ($\rho \geq 0$), the system seems not to show self-stable solutions at high energy, conversely to the case with $\rho < 0$.

In general, from Fig. 4.5, we better realise that an increment of the circulating power leads to an enhancement of the drift of the resonances, which can have either a thermal origin or derive from the Kerr effect. Overall, the amount of shift is the result of the competition between the Kerr and thermo-optic nonlinearity, and determine the hysteresis loop seen in Fig. 4.3. Indeed, the area of the hysteresis can be related with ρ, as well as with the laser detuning; the area reduces as δ_0 approaches to the central frequency ω_0, as the hysteresis becoming negligible.

We can discuss those results taking a look directly at the eigenvalues plotted in Fig. 4.6, as function of I_0, for $\sigma = 50$, $\rho = -10$ and $\delta_0 = -15$ in (a), $\rho = 0$ and $\delta_0 = 3$ in (b) and $\rho = 10$ and $\delta_0 = 15$ in (c). We compare the case of $\rho < 0$ in Fig. 4.6 (a) with the case of $\rho \geq 0$ in (b) and (c). When $\rho < 0$, there is a complex pair of eigenvalues with positive real parts in the range $I_0 = [1.702, 16]$, where the SP region appears (Fig. 4.6 (a)). When $\rho \geq 0$ the imaginary parts of the complex pair of eigenvalues are zero where the system showed SP solutions for $\rho < 0$ in (a). Therefore, there are not regions of SP observed for $\rho \geq 0$ (Fig. 4.6 (b) and (c)).
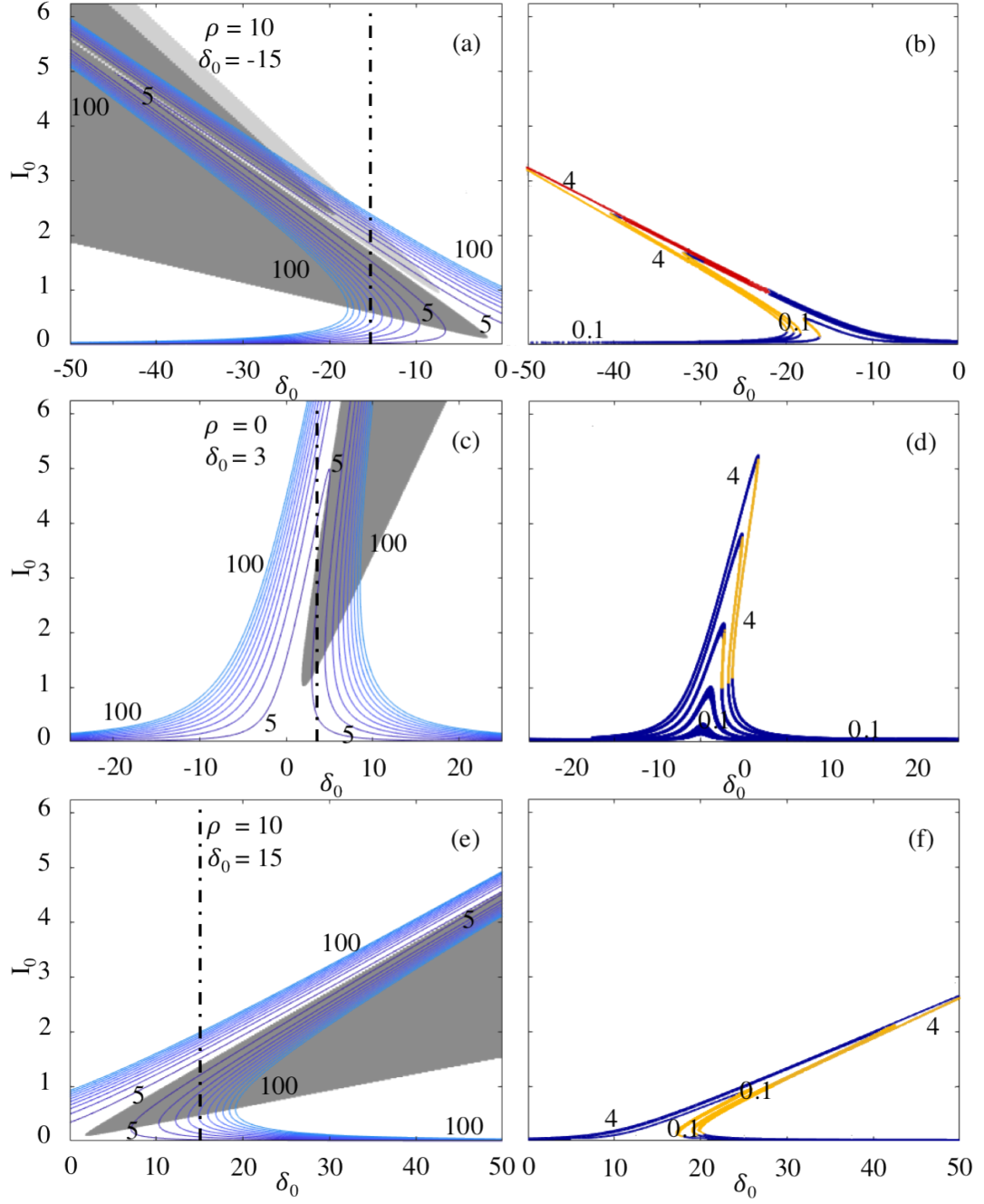
Figure 4.5. Stability maps and nonlinear resonances against thermo-optic coefficient, for $\sigma = 50$, $\rho = -10, 0, 10$, in (a), (c) and (e) respectively. The difference of sign between Kerr and the thermo-optic coefficients affects the stability of the regions, inducing a blue-shift of the cavity resonances, when $\rho < 0$ or a red-shift, when $\rho > 0$. This aspect becomes more clear by observing the stationary states from 5 to 100 (resonances curves) plotted in overlap with the stability maps in each of the previous cases, for values of $\delta_0 = -15, 3$ and 15 in (b), (d) and (f) respectively.
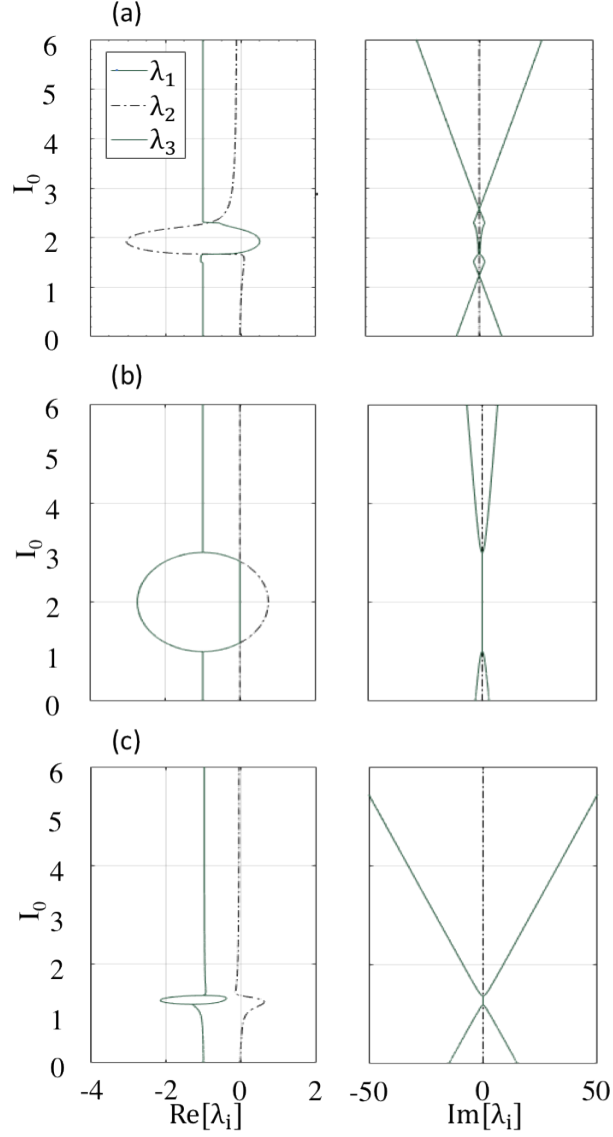
Figure 4.6. Eigenvalues for $\sigma = 50$, $\rho = -10$, $\delta_0 = -15$ in (a), $\rho = 0$, $\delta_0 = 3$ in (b) and $\rho = 10$, $\delta_0 = 15$ in (c). The eigenvalues analysis show that when $\rho >= 0$ (b,c) there are not self-pulsing region in the system, conversely to the case with $\rho < 0$ (a).

Reaching self-stable regimes with low pump power might result experimentally tricky because the hysteresis phenomena. Nonetheless, it is possible to define the condition to achieve SP regimes from stable equilibrium states at low energies

$$\delta_0^{SP} < \delta_0^{U},$$ (4.15)

which defines a map as a function of the parameters (ρ, σ).
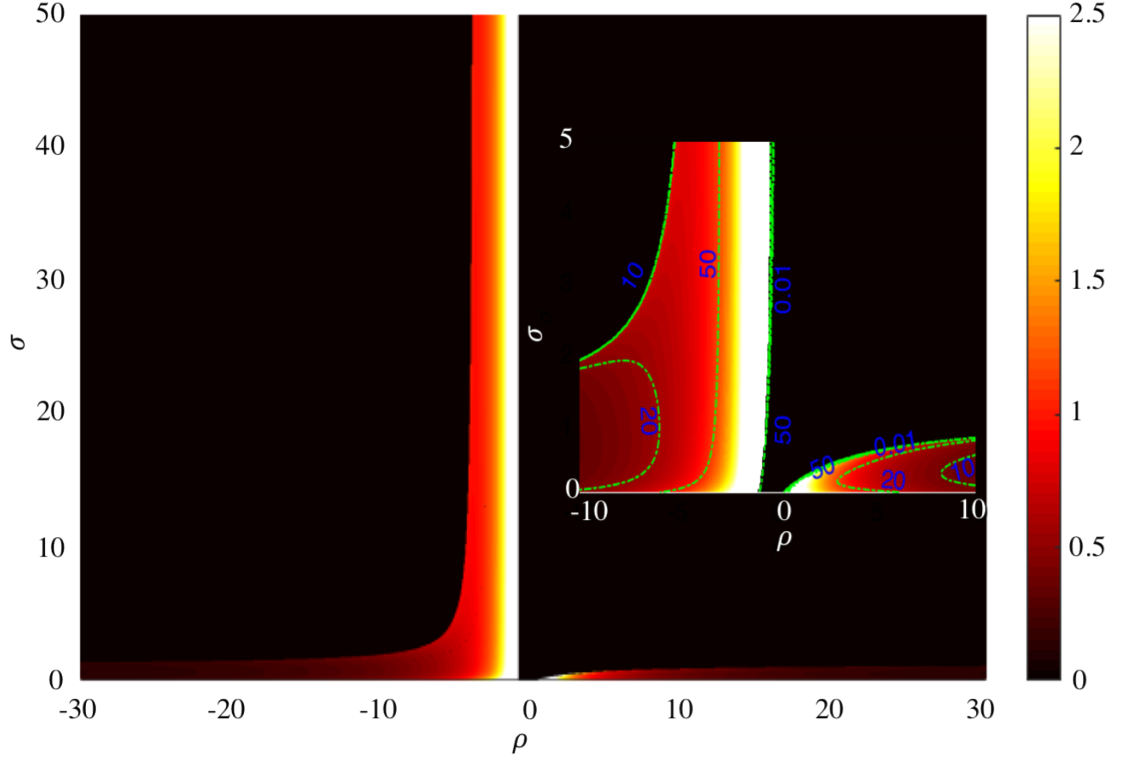
Figure 4.7. The map (ρ,σ) reports the parameters ρ and σ that satisfy Eq. 4.15, whose energy to observe the SP regime increases from low to high, in accordance with the colormap from dark-red to white color. The dark region is defined by (ρ,σ) that do not meet the condition 4.15 or by the discontinuity condition 4.16. Green dashed lines are concerning the values of P_0 supplied.

The colour map of Fig. 4.7 defines the threshold power for a P_0 necessary to enable SP: low power values correspond to dark-red, high values to white. The map has been worked out from Eq. 4.13, evaluated at $\delta_0^{SP} = \delta_0^U = \pm\sqrt{3}$. It is useful to identify discontinuity regions of values (ρ,σ)

$$(1+\rho)(\rho(\sigma-1)+3\sigma) \leq 0. \tag{4.16}$$

The black region in the map, corresponding to (ρ,σ) values where SP states are not accessible from lower energy states, depends on either the discontinuity condition 4.16, or when the condition 4.15 is not satisfied. We observe that the energy required to achieve the condition 4.15 shrinks with σ. The latter means that when the thermo-optical nonlinearity compete with the Kerr effect on timescales that become comparable, or in those cavities having high Q-factors [175], SP states are easily observed. The lowest values of energy are found in the region given by $|\sigma/\rho| \ll 1$. There is a narrow region, defined by $\sigma/\rho > 1$, in the semi-negative ρ plane that allows SP solutions for relatively low values of energy. Therefore, in the next sections, it will be interesting to investigate

the influence of the FWM on the thermal dynamics assuming σ values within the range from 1 to 100.

4.5   Case of Two-Frequency Continuous Wave Excitation: the Role of Parametric Effects

The ability to control multi-stability, SP and other interesting dynamics arising from the nonlinear interaction between optical fields and the cavity medium, is fundamental for achieving the desired performance. The theory of stability showed in Chapter 2 has provided us with the theoretical tools to study the steady states of a microresonator and the bifurcations of its equilibrium, while the framework of CMT, derived in Chapter 3, has defined the theoretical background to describe the dynamical evolution of the propagating fields. In the Sections 4.3 and 4.4, our analysis has been applied to the simple case of a single mode. We had a preliminary understanding of the role played by the parameters ρ, σ and by the detuning of the resonances.

Given a certain configuration of the stationary states for the pump cavity field, a relocation of its bifurcations in the system's parameter space would create new branches of equilibria, modifying the behaviour of a microcavity. Under this assumption, we study the role that a signal may have in influencing the nonlinear regimes (e.g. self-oscillations) of a strong pump, taking into account the effect of a parametric interaction, specifically FWM [181].

It will be demonstrated that the additional mode coupled into the microcavity affect dramatically the dynamics of the pump even at very low signal powers. It will be shown that oscillating regimes can be induced, as well as controlled in amplitude and shape, changing the amplitude of the signal.

Let us consider two continuous wave lasers coupled into two different resonant frequencies of the cavity, (pump and signal). We assume that these waves can interact in a third-order nonlinear medium via FWM, generating a primary and, possibly, a secondary (weaker) idler, as described in Section 3.3.

If the energy of the pump is very high, the signal and idler fields can be generated through FWM in a similar way as achieved in *optical parametric oscillators* (OPO), whose gain is given by

$$k = G - 1, \tag{4.17}$$

where

$$G = Re\left\{\sqrt{I_0^2 - \Delta_k^2}\right\},$$

with $\Delta_k = \delta_0 + I_0(2+\rho)$ the effective phase mismatch. Therefore, when the gain overcomes the intrinsic losses, which here are normalised to one, the signal and idler amplitudes grow. The condition for which $G > 1$ represents the threshold of the OPO. In this work, the parametric gain is neglected, thus $G < 1$ for each case that is described next.

Considering the generation of a single idler, a_{-1}, the system 4.1 becomes

$$\begin{cases} \frac{da_0}{dt} = -a_0 - i[\delta_0 + \Delta - (2I_T - |a_0|^2)]a_0 + 2ia_0^* a_1 a_{-1} - iS_0, \\[2mm] \frac{da_0^*}{dt} = -a_0^* + i[\delta_0 + \Delta - (2I_T - |a_0|^2)]a_0^* - 2ia_0 a_1^* a_{-1}^* + iS_0^*, \\[2mm] \frac{da_1}{dt} = -a_1 - i[\delta_1 + \Delta - (2I_T - |a_1|^2)]a_1 + ia_0^2 a_{-1}^* - iS_1, \\[2mm] \frac{da_1^*}{dt} = -a_1^* + i[\delta_1 + \Delta - (2I_T - |a_1|^2)]a_1^* - i(a_0^2)^* a_{-1} + iS_1^*, \\[2mm] \frac{da_{-1}}{dt} = -a_{-1} - i[\delta_{-1} + \Delta - (2I_T - |a_{-1}|^2)]a_{-1} + ia_0^2 a_1^*, \\[2mm] \frac{da_{-1}^*}{dt} = -a_{-1}^* + i[\delta_{-1} + \Delta - (2I_T - |a_{-1}|^2)]a_{-1}^* - i(a_0^2)^* a_1, \\[2mm] \sigma\frac{d\Delta}{dt} = -\Delta - \rho I_T, \end{cases} \tag{4.18}$$

We have a perturbation 7×7 matrix associated to the system above, given by the Jacobian 4.4, whose eigenvalues can be worked out numerically. It is possible, however, to obtain an approximate expression for the boundaries of the equilibrium regions when the idler terms are neglected. In this case, the interaction between the pump and the signal occurs via cross-phase modulation (XPM). In the limit of large absolute pump detuning $|\delta_0| >> 0$, the tongue is bounded by:

$$I_0^{XPM} = \frac{\delta_1 - 2I_1(1+\rho) \pm \sqrt{I_1^2(1+\rho)^2 - 1}}{2 + \rho} \tag{4.19}$$

These regions allow to easily distinguish the effect of the parametric FWM from the effect of the XPM, where the idler plays no role. Relevantly, new SP/U regions appear where the stationary state has a large idler's intensity. Here the FWM can be considered the dominant effect. To roughly identify the region where the FWM is strong, we can note that high FWM gain occurs where the generated idler frequency is resonantly coupled, i.e. $\delta_{-1} = (2+\rho)I_T - I_{-1}$, leading to:

$$\delta_0 = \frac{\delta_1}{2} + \frac{(2+\rho)I_T - I_{-1}}{2} \approx \frac{\delta_1}{2} + \frac{I_0(2+\rho)}{2} \tag{4.20}$$

being the latter approximation valid for low $I_{\pm 1}$ intensities.

4.5.1 Equilibrium Analysis for a negative ρ

We assume $\sigma = 50$ and $\rho = -10$, which can be compatible with materials like CaF_2, BaF_2. Then, we study the map of stability setting a signal detuning $\delta_1 = -7$ and an intra-cavity signal energy $I_1 = 0.1$. The results are reported in Fig. 4.8.
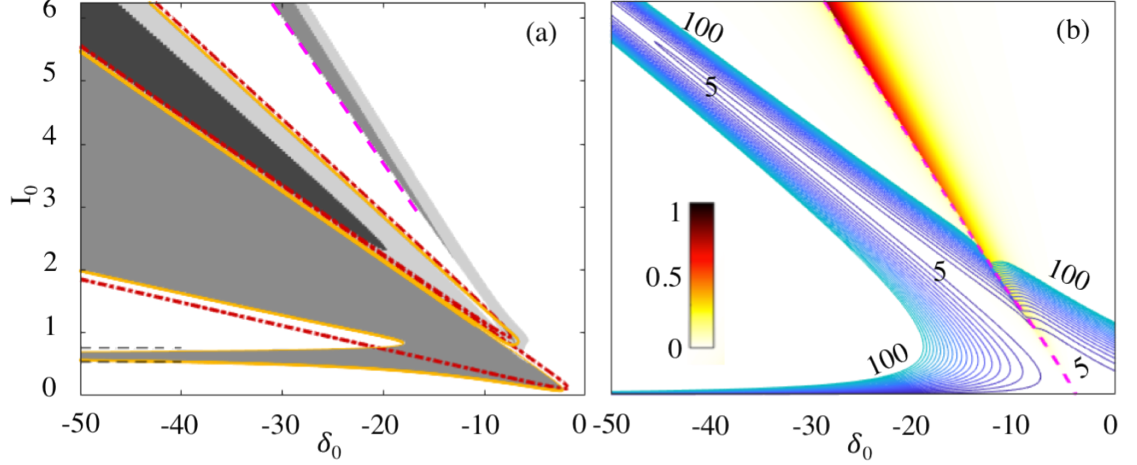
Figure 4.8. (a), (Stability map and (b) stationary state for $\sigma = 50$, $\rho = -10$, $\delta_1 = -7$; $I_1 = 0.1$. (a) Stable (S), unstable (U), self-pulsing (SP) and overlapping SP\U region are in white, dark gray, light gray, and black, respectively. The boundaries of the SP regions for $S_1(t) = 0$ and $F_i = 0$ are in dashed red and orange, respectively. Black and magenta dotted lines are Eqs. 4.19 and 4.20, respectively. (b) Stationary state values for the lowest I_{-1} are reported in fake colors; nonlinear resonances are in blue for P_0 from 5 to 100.

It is important to stress that such energy values are small comparable to the threshold $2|\sqrt{3}(\rho + 1)|^{-1} \approx 0.12$, for observing any signal bi-stability when the pump is off. Nevertheless, such an energy is able to produce in the stability regions two relevant changes, when compared to the case of no signal ($S_1 = 0$, red dashed lines). First of all, the coupled signal creates a new tongue in the U region, purely related to the XPM and to the change in the detuning Δ induced by the signal. This is visible when comparing the results with the regions where no FWM is present, $F_i = 0$ (orange) in Fig. 4.8 (a), described by Eq. 4.19. Unfortunately, these regions cannot be easily accessed experimentally at low intensities, requiring values $P_0 > 30$ in the examples reported. This is clear when looking at the iso-level curves of the stationary state for constant input pump powers in Fig. 4.8 (b) (blue contour lines). Secondly, new FWM induced, SP/U region arise where the stationary state has a large idler's intensity, with detuning δ_0 satisfying Eq. 4.20. The latter

equation is plotted with a magenta line for the specific cases. Notably, those SP/U[3] regions can be accessed for relatively low input pump powers, with $P_0 > 3$. The idler mode can have up to three real solutions, which, however, are found only for high pump excitation ($P_0 > 40$); the stationary state of the idler solution with the lowest energy is reported in Fig. 4.8, in false colour map.
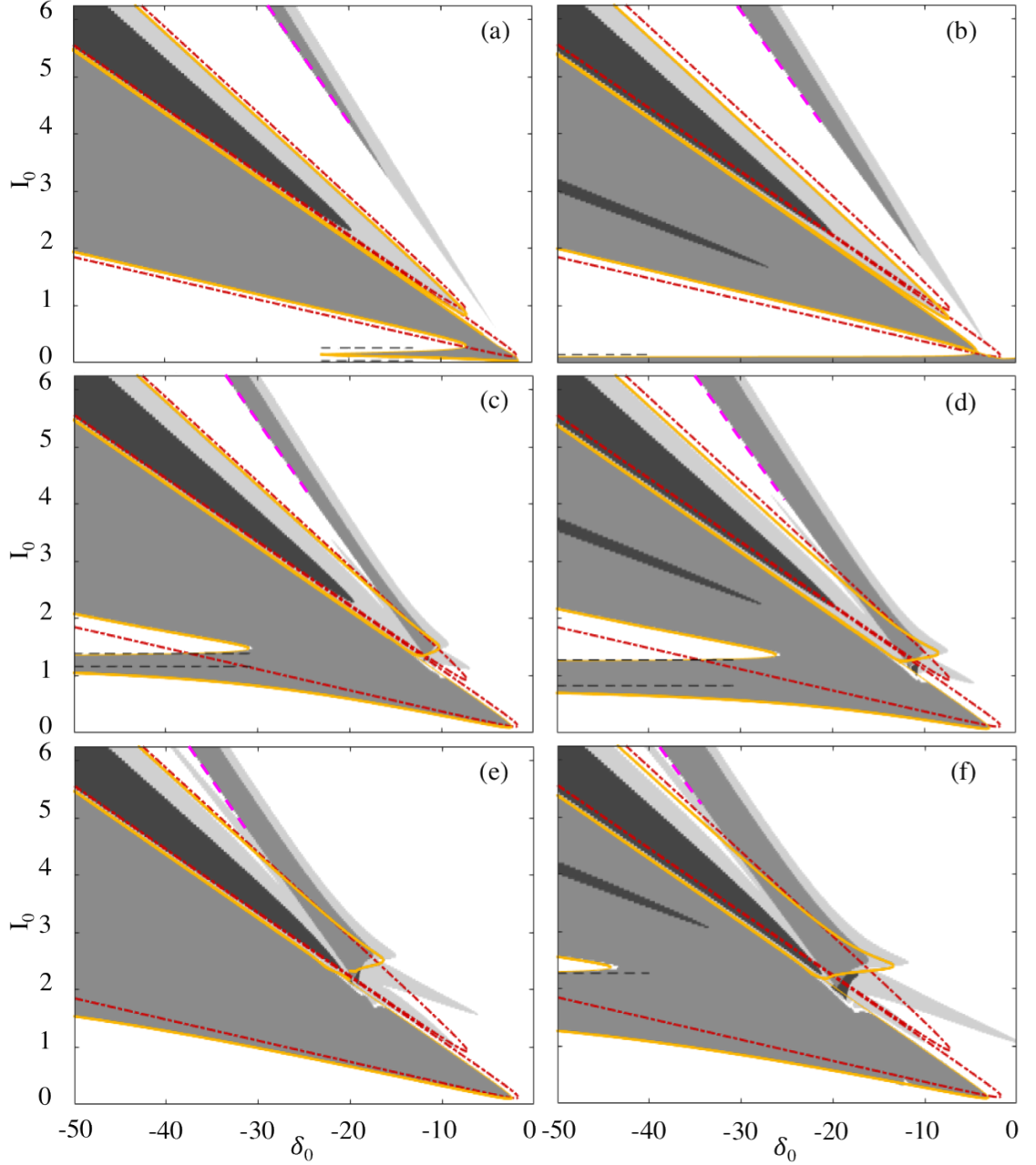
Figure 4.9. The stability regions of the system can be opportunely "adjusted" by tuning the signal detuning δ_1. We consider $\sigma = 50$, $\rho = -10$ and two values of $I_1 = 0.1, 0.2$ (left and right graphs respectively), for detuning $\delta_1 = -3, -12, -20$ in (a,b), (c,d) and (e,f) respectively. We observe that new SP tongues emerges and merges with exiting SP and U regions. Their shapes can also be modified by the signal intra-cavity energy I_1 (follow the graphs from top to bottom).

---

[3]It is important to remind that the overlapping of SP with U region means that SP solutions are found for values of the pump energy P_0 included between the two LP points which define the unstable branch of the bi-stability curve at a given detuning.

In general, Eqs. 4.19 and 4.20 provide a useful mean to evaluate the regions that can be affected by the presence of the signal. In particular, 4.20 shows that the signal detuning can be used to move the SP regions over the (δ_0, I_0) plane. This indeed appears clear when observing the sequence of plots shown in Fig. 4.9, realised by progressively changing the signal detuning, which assume the values: $\delta_1 = -3, -12, -20$ in (a,b), (c,d) and (e,f) respectively, for $I_1 = 0.1$ in (a,c,e) and for $I_1 = 0.2$ in (b,d,f), for $\sigma = 50$ and $\rho = -10$. Following the graphs from top to bottom, we note that the primary SP tongue merges with a secondary one, which is mainly generated by the idler via FWM, as δ_1 increases. Moreover, the signal detuning modifies the shape and the dimension of the primary U region, contributing the development of secondary unstable region in the high-energy SP domain. Therefore, δ_1 is a fundamental parameter for a reallocation of the equilibria.

We can have a better insight looking at the eigenvalues of a solution of interest of the map, in order to study how the real and imaginary parts change as δ_1 changes and how the FWM affects it. The case with $\sigma = 50$, $\rho = -10$, $\delta_0 = -5.4$, $I_0 = 0.8$ and signal energy $I_1 = 0.2$ has been represented in Fig. 4.10, including either the contribution of the FWM in Fig. 4.10 (a) or neglecting its terms from the Eqs. 4.18 in Fig. 4.10 (b). Therefore, in Fig. 4.10 (a), when we consider the FWM contribution, we can distinguish thee pair of complex conjugate eigenvalues and a real eigenvalue (black dashed). The latter is leading in the range $\delta_1 = [-8, -9.4]$ and $\delta_1 = [-11.2, -20]$, remaining very close to zero but never becoming positive. Instead, in the range $\delta_1 = [-2.9, -8]$ and $\delta_1 = [-9.4, -11.2]$ two complex conjugate pairs are leading (green and red lines), which assume positive values giving rise to Hopf bifurcations. The third pair (blue line) has negative real values over the whole δ_1 range. Therefore, the solutions present a self-oscillating behaviour at the energy and pump detuning considered. In absence of FWM (Fig. 4.10 (b)), the real parts of all the eigenvalues are negative over the values of δ_1 considered, having steady state solutions. Remarkable, in presence of FWM, is that SP solution are reached for detuning and energy values that do not lie on the unstable branch, where the system shows bi-stability.
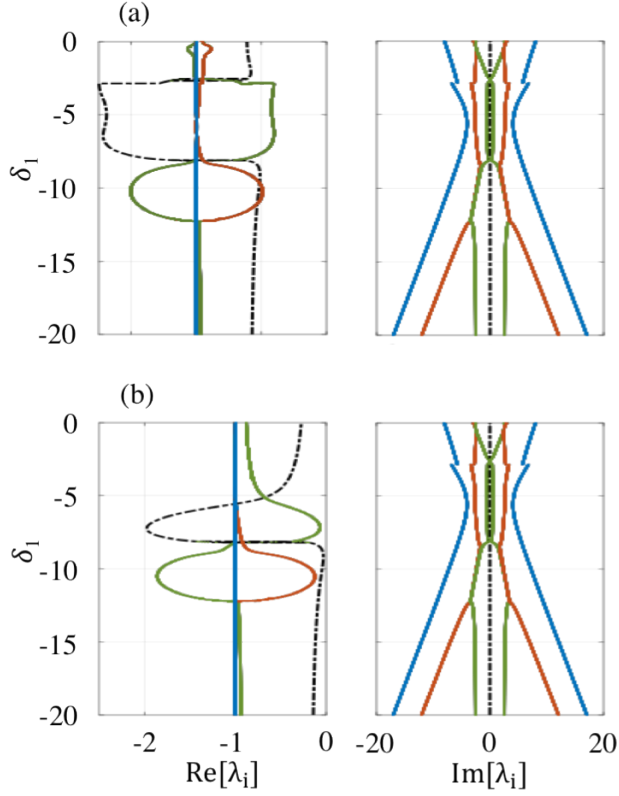
Figure 4.10. We consider $\sigma = 50$, $\rho = -10$, $\delta_0 = -5.4$ $I_0 = 0.8$ and $I_1 = 0.2$, including in (a) FWM contribution and neglecting its terms from Eqs. 4.1 in (b). The Jacobian matrix of the system Eq. 4.4 has three complex conjugate pairs and one real eigenvalues, shown in different colours. Imaginary parts of the same pair of complex conjugate eigenvalues are drawn with the same colours. In (a), the leading eigenvalue (black dashed) is real and negative in the range $\delta_1 = [-8, -9.4]$ and $\delta_1 = [-11.2, -20]$. Then, Hopf bifurcations appear in the range $\delta_1 = [-2.9, -8]$ and $\delta_1 = [-9.4, -11.2]$, due to leading complex conjugate pairs of eigenvalues (green and red lines), with positive real parts. There is a further complex pair of eigenvalues (blue line) with negative real parts all over the range of δ_1. When we remove the FWM in (b) all real parts of the eigenvalues assume negative values over the range of δ_1 considered, thus the self-stable equilibria are replaced by stable foci.

4.5.2 Equilibrium Analysis for a positive ρ

We now study the case of Kerr and thermo-optic coefficient having the same sign, which is typical in materials like SiO_2 and Si. We set $\sigma = 50$, $\rho = 10$, $I_1 = 0.1$. From the preliminary considerations regarding the case of single pump coupling discussed in Section 4.4 and shown in Fig. 4.5 (c) for $\rho > 0$, we set a positive pump detuning range and plot the stability map. From Fig. 4.11 (a), we note that SP and U overlapping regions now appear where the system had uniquely unstable steady solutions (see Fig. 4.5 (c) for comparison). Those new SP regions, especially at low energy, are still related to the XPM and the detuning Δ induced by the signal, approximate by Eq. 4.19 when $|\delta_0| >> 0$. As for $\rho < 0$, the regions where the FWM is stronger are those located where the

stationary states have a large idler's intensity. This appears clear from the iso-level curves of the stationary state for constant input pump powers in Fig. 4.11 (b). Differently from the case of $\rho < 0$, the SP regions seem to be bounded exclusively within the U region, in other words, SP cannot be experimentally observed because of the bi-stability.
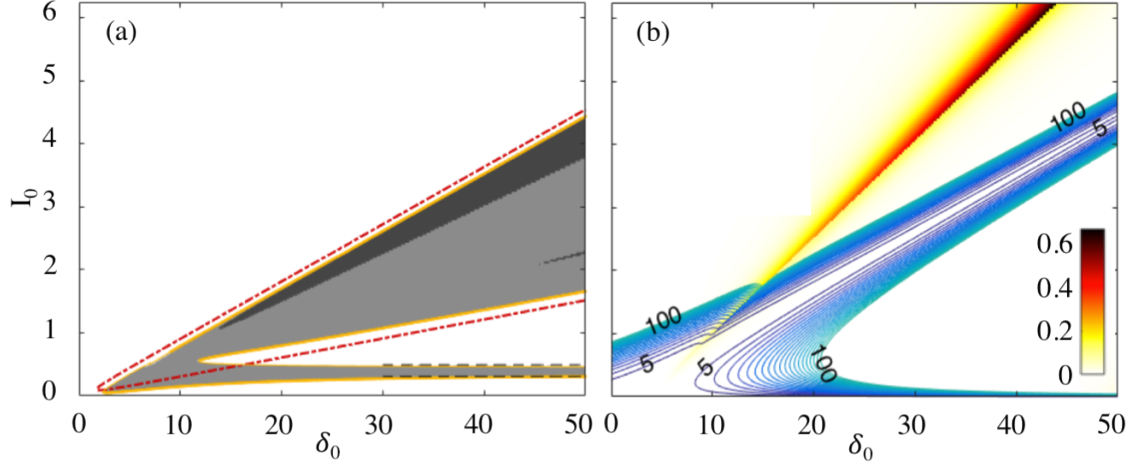
Figure 4.11. (a) Stability map and (b) stationary state values for the lowest I_{-1} for $\sigma = 50$, $\rho = 10$, $\delta_1 = 7$, $I_1 = 0.1$. In (a), stable (S), unstable (U), self-pulsing (SP) and overlapping SP\U regions are in white, dark gray, light gray, and black, respectively. The boundaries of the S regions for $S_1(t) = 0$ and $F_i = 0$ are in dashed red and orange, respectively. Black and magenta dotted lines are Eqs. 4.19 and 4.20, respectively. (b) Stationary state values for the lowest I_{-1} are reported in fake colors; nonlinear resonances are in blue for P_0 from 5 to 100.

We can try to exceed this limitation by tuning δ_1 as it has been previously done for $\rho < 0$. In Fig. 4.12 we consider $\delta_1 = 3, 12, 20$ in (a,b), (c,d) and (e,f) respectively for $I_1 = 0.1$ in (a,c,e) and for $I_1 = 0.2$ in (b,d,f). Even though the signal detuning changes, the SP regions are still bounded within the U region. However, we take into account the idler solution with the lowest energy, thus the substantial FWM contribution in promoting self-pulsing may be observed at higher energies (yet, they are tricky to access experimentally).

For sake of completeness, we now chose a particular solution in the region resulting from the overlap U/SP, and examine the eigenvalues as δ_1 changes. The outcome is displayed in Fig. 4.13 for $\sigma = 50$, $\rho = 10$, $\delta_0 = 20$, $I_0 = 1.5$ and signal energy $I_1 = 0.2$. In 4.13 (a), when we take into account the FWM contribution, there are a positive real leading eigenvalue and three complex pairs (there are different eigenvalues with the same imaginary part), whose real parts are positive in the range $\delta_1 = [0, 17]$. The latter are responsible for the narrow SP tongue enclosed at the bottom of the U region in (Fig. 4.12 (b) (d) and (f). Then, in the range $\delta_1 = [17, 20]$ all the eigenvalues have negative real parts, hence the solutions produce stable foci, becoming unstable or self-pulsing when

$\delta_1 > 20$, which is due to the presence of a real positive eigenvalue (black dashed) and complex pairs (blue line) with positive real parts (Hopf bifurcation).

When we neglect the FWM from the system, in Fig. 4.13 (b), we have only one real leading eigenvalue (black dashed) that remains constantly positive for all the range of $\delta_1 < 20$ considered, defining unstable solutions.
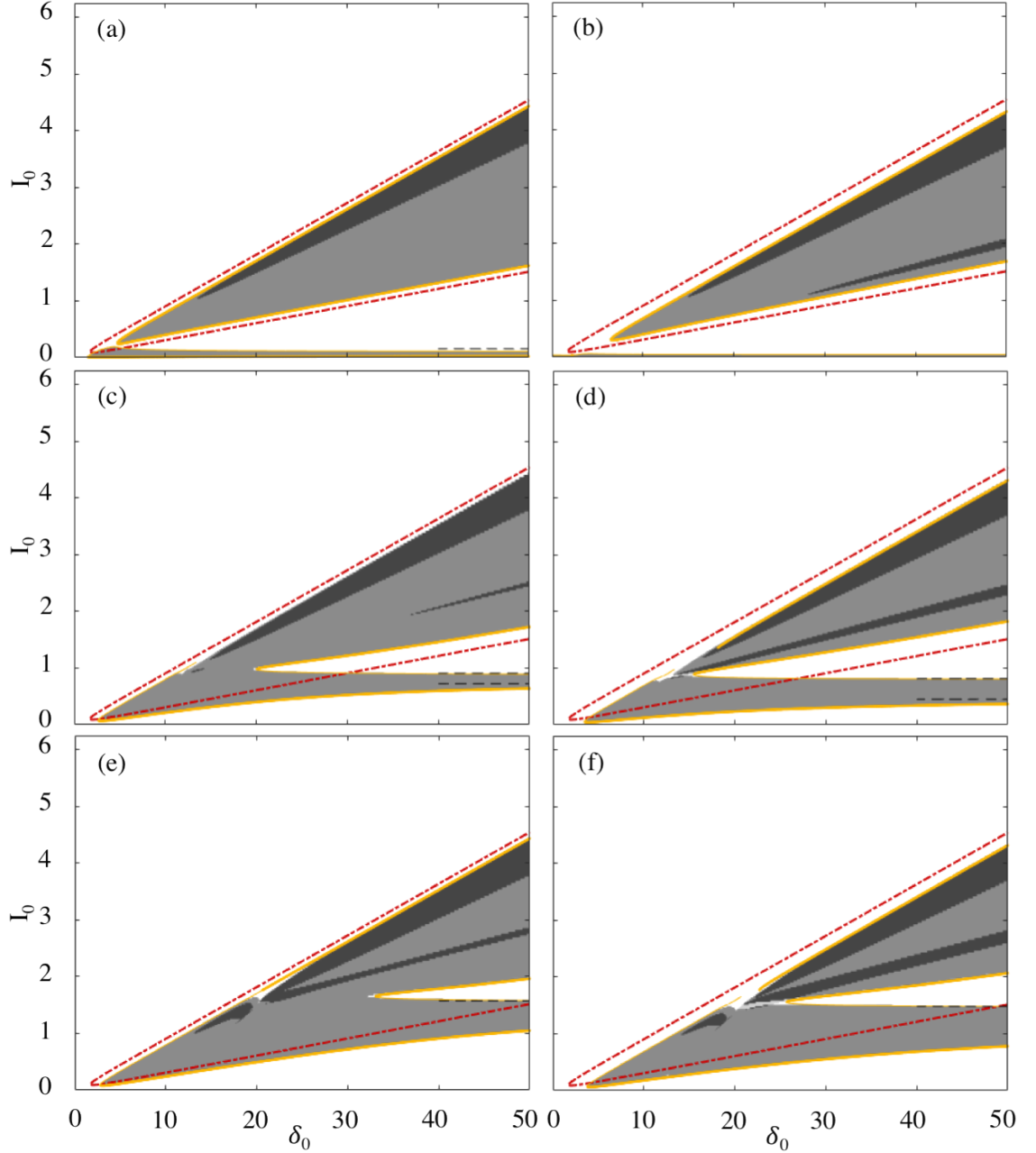
Figure 4.12. The stability regions of the system can be opportunely "adjusted" by tuning the signal detuning δ_1. We consider $\sigma = 50$, $\rho = 10$ and two values of $I_1 = 0.1, 0.2$ (left and right graphs respectively), for detuning $\delta_1 = 3, 12, 20$ in (a,b), (c,d) and (e,f) respectively. Variation of the signal detuning slightly change the equilibrium regions of the system, although SP regions are bounded to the U regions.
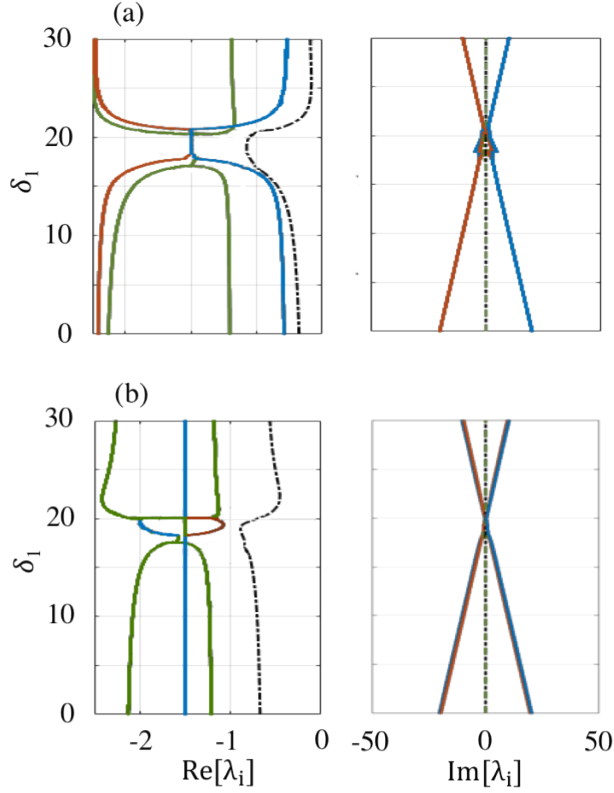
Figure 4.13. We consider $\sigma = 50$, $\rho = 10$, $\delta_0 = 20$ $I_0 = 1.5$ and $I_1 = 0.2$, including in (a) FWM contribution and neglecting its terms from Eqs. 4.1 in (b). The Jacobian matrix of the system Eq. 4.4 has three complex conjugate pairs and one real eigenvalues, shown in different colours. Imaginary parts of the same pair of complex conjugate eigenvalues are drawn with the same colours. By including the FWM contribution in (a), in the range $\delta_1 = [0, 17]$ we have a positive real leading eigenvalue (black dashed) and complex pairs with real positive parts and degenerate imaginary parts (we can observe only a single blue line, as there is an overlapping between different eigenvalues). Therefore, we have coexistence of self pulsing and unstable equilibria. We also observe a real eigenvalue (green), which is negative and non-leading. When $\delta_1 = [17, 20]$ all the eigenvalues have negative real parts. The system shows stable behaviour. When $\delta_1 > 20$, we have a similar situation, with SP/U regions overlapped. In (b), where the FWM is neglected, the system shows instability over the whole the range of δ_1 plotted, indeed there is only a real and positive leading eigenvalue (black dashed).

We may obtain SP solutions at low energy in the stable region by decreasing the ratio σ/ρ, hence, in materials with a slower thermal relaxation time, for instance, those having free carries like silicon. In Fig. 4.14 (a) are reported the stability map by setting $\sigma = 1.5$, $\rho = 10$, $\delta_1 = 10$ and $I_1 = 0.2$. From that, we can appreciate a substantial change with respect to the case with $\sigma = 50$. A wide SP region located above of the U region appears, but it is still related to the XPM rather than FWM at low energies (see the red dashed boundary). Indeed, from the plot of the nonlinear resonances in fake colours in Fig. 4.14 (b), we note that the idler has a strong enhancement only when the pump intra-cavity energy I_0 is above $I_0 \approx 3$, that is beyond the range of energy experimentally easily reachable.

These results are in perfect agreement with our considerations expressed in Section 4.4, where the map (σ, ρ) in Fig. 4.7 clearly excludes the possibility of observing SP when $|\sigma/\rho| >> 1$. Here, we come to a preliminary conclusion for which FWM has a strong influence in supporting nonlinear thermal dynamics in microcavities, having a negative thermo-optic coefficient, while a very marginal role in promoting such dynamics in materials with a positive thermo-optic coefficient. However, the situation can be improved as the ratio σ/ρ becomes smaller and smaller.
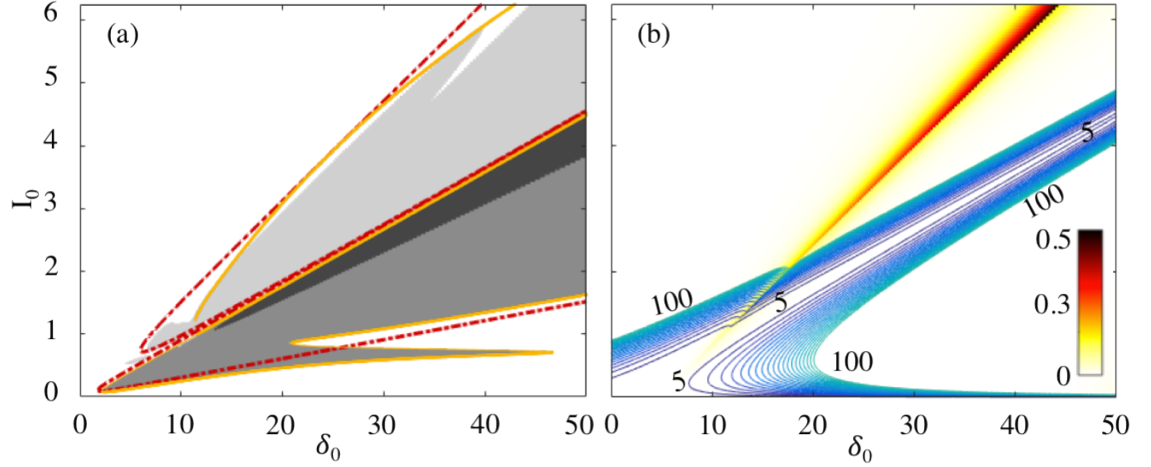
Figure 4.14. Stability map fixing $\sigma = 1.5$, $\rho > 0$, $\delta_1 = 10$, $I_1 = 0.2$. (a) A large SP region arises in the region where thee system equilibria were previously stable ($\sigma = 50$). However, the new region is produced manly by XPM at low energies (below $I_0 = 2$), while receiving contribution from FWM at higher energies. This can be observed from the stationary state values for the lowest I_1 in (b).

4.6 Dynamical Behaviour of the System

Now, we include all the terms of cascading FWM, responsible for the generation of a secondary idler a_2. This allows us to test the validity of our approach at higher pump and signal rates, which may arise in the SP regimes. Further cascaded generation is neglected here as the energies involved are low. The dynamical analysis of microcavities performed in this section will integrate the results achieved from the analysis of stability developed in the previous section. From Eqs.4.1, the system

that we study is the following:

$$
\begin{cases}
\frac{da_0}{dt} = -a_0 - i[\delta_0 + \Delta - (2I_T - |a_0|^2)]a_0 + 2ia_0^* a_1 a_{-1} + ia_1^2 a_2^* + 2ia_1^* a_2 a_{-1} - iS_0, \\[4pt]
\frac{da_0^*}{dt} = -a_0^* + i[\delta_0 + \Delta - (2I_T - |a_0|^2)]a_0^* - 2ia_0 a_1^* a_{-1}^* - ia_1^{*2} a_2 - 2ia_1 a_2^* a_{-1}^* + iS_0^*, \\[4pt]
\frac{da_1}{dt} = -a_1 - i[\delta_1 + \Delta - (2I_T - |a_1|^2)]a_1 + 2ia_1^* a_2 a_0 + ia_0^2 a_{-1}^* + 2ia_0^* a_2 a_{-1} - iS_1, \\[4pt]
\frac{da_1^*}{dt} = -a_1^* + i[\delta_1 + \Delta - (2I_T - |a_1|^2)]a_1^* - 2ia_1 a_2^* a_0^* - ia_0^{*2} a_{-1} - 2ia_0 a_2^* a_{-1}^* + iS_1^*, \\[4pt]
\frac{da_{-1}}{dt} = -a_{-1} - i[\delta_{-1} + \Delta - (2I_T - |a_{-1}|^2)]a_{-1} + ia_0^2 a_1^* + 2ia_2^* a_0 a_1, \\[4pt]
\frac{da_{-1}^*}{dt} = -a_{-1}^* + i[\delta_{-1} + \Delta - (2I_T - |a_{-1}|^2)]a_{-1}^* - ia_0^{*2} a_1 - 2ia_2 a_0^* a_1^*, \\[4pt]
\frac{da_2}{dt} = -a_2 - i[\delta_2 + \Delta - (2I_T - |a_2|^2)]a_2 + ia_1^2 a_0^* + 2ia_{-1}^* a_0 a_1, \\[4pt]
\frac{da_2^*}{dt} = -a_2^* + i[\delta_2 + \Delta - (2I_T - |a_2|^2)]a_2^* - i(a_1^2)^* a_0 - 2ia_{-1} a_0^* a_1^*, \\[4pt]
\sigma \frac{d\Delta}{dt} = -\Delta - \rho I_T,
\end{cases}
\tag{4.21}
$$

4.6.1 Case with $\rho < 0$

Assuming the stability map of Fig. 4.9, we carry out our analysis by varying the input pump power P_0, for $\sigma = 50$, $\rho = -10$ and $\delta_0 = -6.7$, so that we set the system initial conditions in order to reach an equilibrium at $t = 0$ located at lowest energy within the secondary SP tongue, where the idler has strong coupling. For such a detuning, SP is never observed when $S_1(t) = 0$. Indeed, from Eq. 4.14, the maximum detuning for SP $\delta_0^{SP} = -7.25$. Therefore, oscillations due to Hopf bifurcations cannot appear if only the pump is coupled into the system.

Suppose $S_1 \neq 0$, we study two different cases: $\delta_1 = -7$, $P_1 = 0.2$ in Fig. 4.15 and $\delta_1 = -12$, $P_1 = 0.9$ in Fig. 4.16. Either in Fig. 4.15 or Fig. 4.16, in (a) the bifurcation diagrams associated to a hard excitation by varying the pump power P_0 from low to high values have been plotted, in (b,d) the phase portraits of the trajectories of interests, in (c) the propagation in time of the intra-cavity fields. Although the two cases are obtained for the same pump parameters, they show a substantially different behaviour. We consider, firstly, the case of Fig. 4.15, with $\delta_1 = -7$ and $P_1 = 0.2$. Here the signal power and detuning have been chosen to observe a fold-Hopf bifurcation. Looking at the stationary state stability map in Fig. 4.8 (a), we see that the FWM-controlled SP and the U regions are in close proximity for $\delta_0 = -6.7$ and $I_0 \approx 1$: such a point belongs to the to the stationary curve with $P_0 \approx 5$ (Fig. 4.8 (b)), where we expect to find the fold-Hopf bifurcation. Fig. 4.15 (a) reports I_0 versus P_0 for the stationary state (magenta), for the dynamical response of the full system (in black for the stable case and in red and blue for the maxima and minima of the oscillating case),

for the system with $S_1(t) = 0$ (yellow curve) and neglecting the FWM terms from the system of equatoins 4.21 (green curve). Starting from low power, the system moves along the stationary state until it approaches the switching threshold at $P_0 > 5$. Here, for $S_1(t) = 0$ the system switches but, as expected, does not oscillate. Conversely, the full system exhibits the expected heteroclinic bifurcation from a saddle point to a saddle-focus trajectory (fold-Hopf) at $P_0 = 5$ and, eventually, a homoclinic bifurcation to a focus at $P_0 = 15$ (Fig. 4.15 (b)). The fold-Hopf bifurcation converges to a stable limit. Such a phase orbit is a homoclinic saddle-focus (Shilnikov) trajectory, which jumps between low and high values of the slow detuning Δ (Fig. 4.15 (d)). For a thermal nonlinearity, this means that the temperature of the system oscillates, mostly between two points. Such a trajectory results in the formation of large pulses (Fig. 4.15 (c)), typical of this type of bifurcation, featuring ripples due to the presence of the focus in the trajectory.
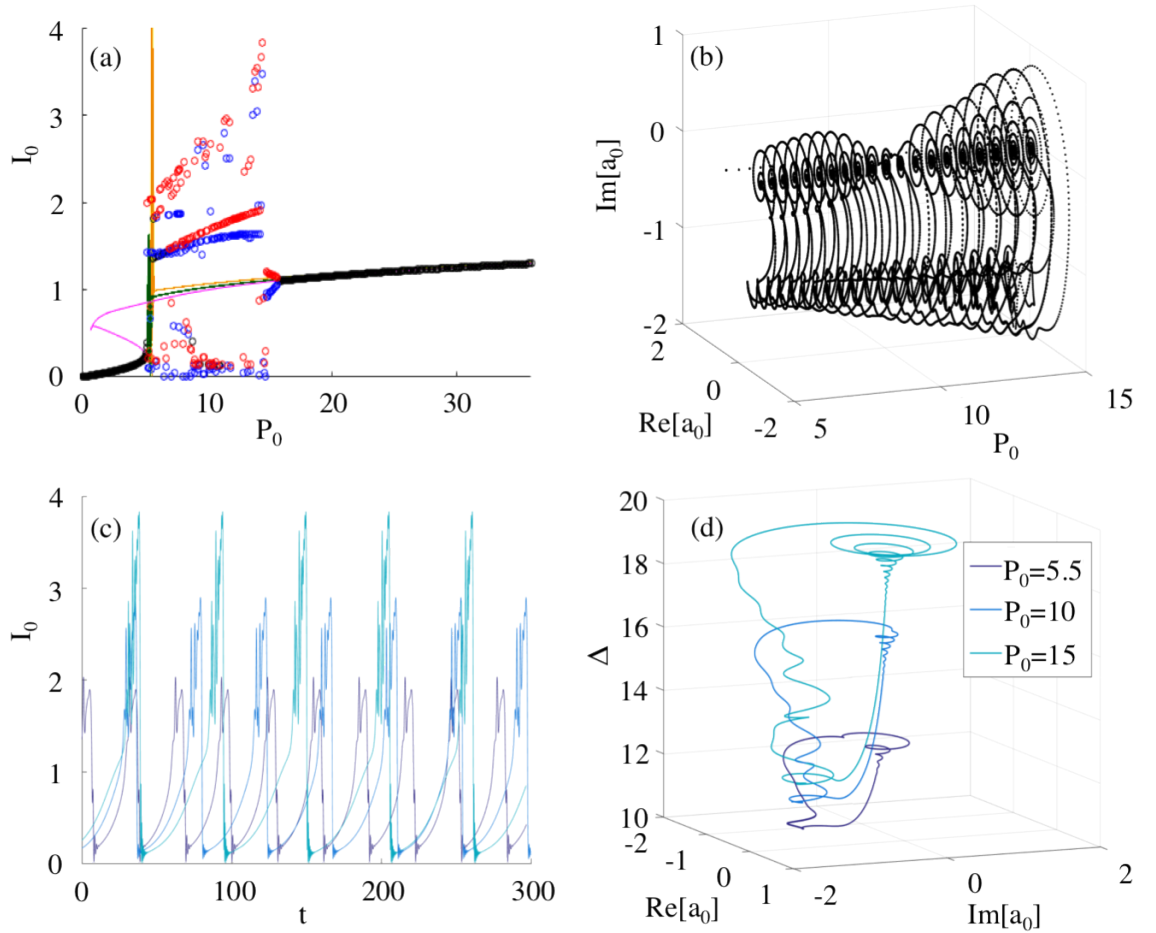
Figure 4.15. Dynamical response at increasing values of P_0 for $\sigma = 50$, $\rho = -10$, $\delta_0 = -6.7$, $\delta_1 = -7$, $P_1 = 0.2$. (a) Bifurcation diagram of I_0 versus P_0, stable outputs are in black, while the maxima and minima of the oscillatory output are in red and blue, respectively. The yellow plot is for $S_1 = 0$, green corresponds to $F_i = 0$ and magenta is for the stationary state. (b) Phase portrait of the bifurcation diagram for P_0 against $Re[a_0]$ and $Im[a_0]$. (c) Time evolution of I_0 at $P_0 = 5.5, 10, 15$ from dark to light blue, respectively, and (d) long term phase plots for Δ versus $Re[a_0]$ and $Im[a_0]$.

Giant pulse generation has recently been studied in thermal systems with two relaxation constants [80]. Such oscillating states are produced mainly by FMW contribution, as it appears by observing the yellow curve.

A completely different scenario is obtained in the case reported in Fig. 4.16 with $\delta_1 = -12$ and $P_1 = 0.9$, where the FWM controlled SP region is far from the U region (see Fig. 4.8 (b) for $\delta_0 = -6.7$).
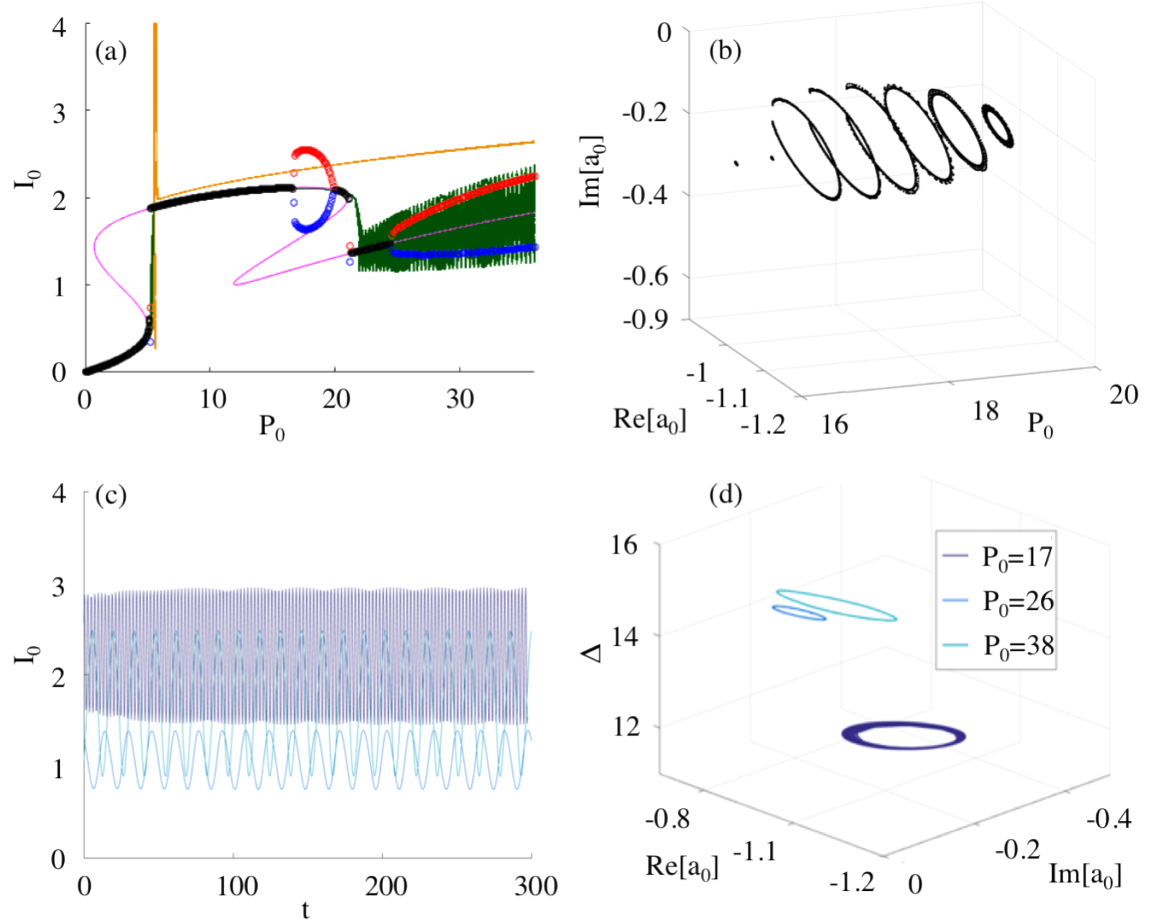
Figure 4.16. Dynamical response at increasing values of P_0 for $\sigma = 50$, $\rho = -10$, $\delta_0 = -6.7$, $\delta_1 = -12$, $P_1 = 0.9$ (a) Bifurcation diagram of I_0 versus P_0, stable outputs are in black, while the maxima and minima of the oscillatory output are in red and blue, respectively. The yellow plot is for $S_1 = 0$, green corresponds to $F_i = 0$ and magenta is for the stationary state. (b) Phase portrait of the bifurcation diagram for P_0 against $Re[a_0]$ and $Im[a_0]$. (c) Time evolution of I_0 at $P_0 = 17, 25, 38$ (dark to light blue, respectively) and (d) long term phase plots for Δ versus $Re[a_0]$ and $Im[a_0]$.

In this case, the system experiences first ($P_0 = 5$) a saddle-node bifurcation, characteristic of bi-stable systems and ruled by a single leading real eigenvalue that changes sign, similarly to the case with $S_1(t) = 0$. At higher powers ($P_0 = 15$) it goes to a Hopf (Andronov-Hopf) bifurcation. Here a couple of complex conjugate leading eigenvalues changes sign, resulting in a smooth cycle (Fig. 4.16 (b)). The real and imaginary parts ($Re[a_0]$, $Im[a_0]$) of the pump amplitude (Fig. 4.16

(d) dark blue) do not present significant oscillation in the detuning region, resulting in a clean periodical oscillation (Fig. 4.16 (c) dark blue). The system bifurcates again to a stable focus at $P_0 = 18$, while a new Hopf bifurcation appears for $P_0 > 25$ where the real part of another set of complex conjugate eigenvalues changes sign. In this case, the phase portraits (Fig. 4.16 (d), light blue) show an oscillation also in the detuning dimension. This last bifurcation belongs to an SP region that appears also when the effect of the FWM is disregarded (green curve in Fig. 4.16 (a)). The FWM, however, contributes to modifying its domain of existence.

Let us remind that the system has a hysteretic response, hence, to have a complete understanding of dynamic, we need to access to the solutions that are on either the lower equilibrium branch or the upper equilibrium branch of the bi-stable curve.
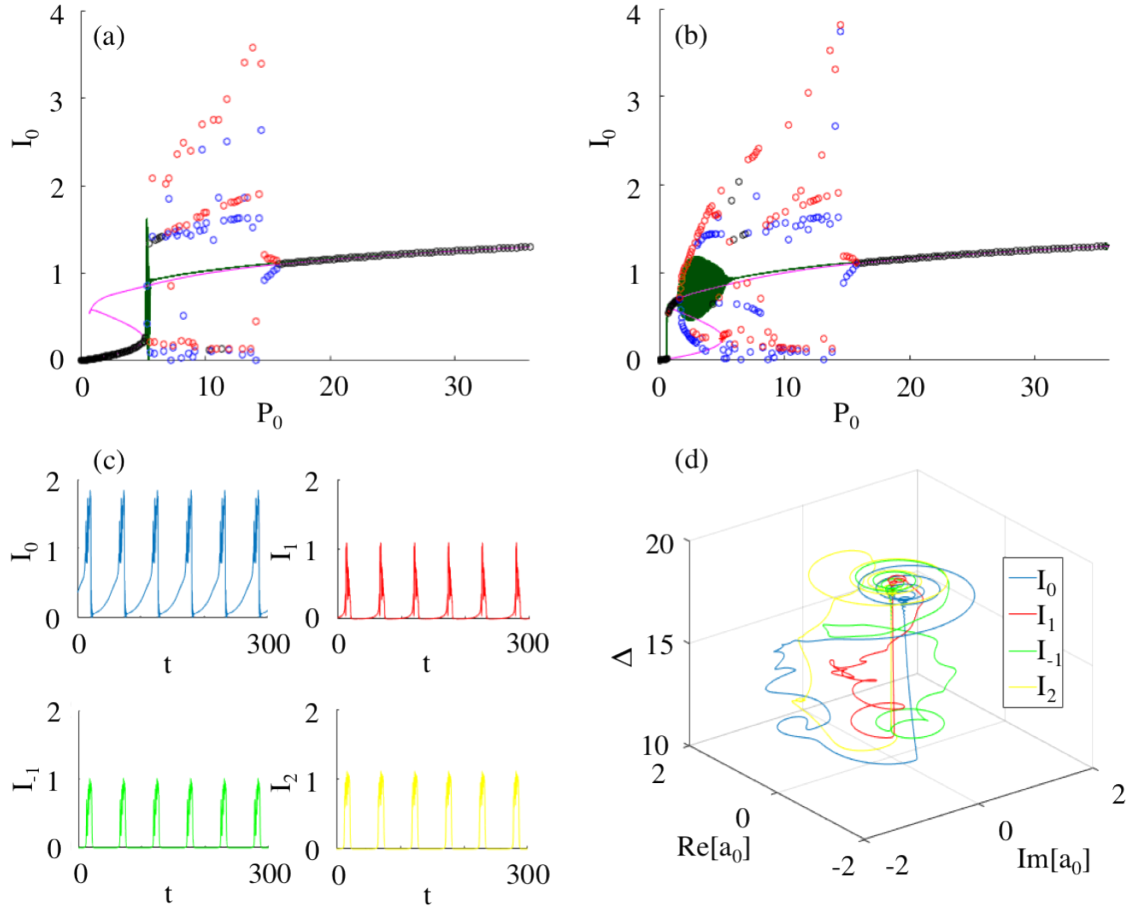
Figure 4.17. Effects of the bi-stability and FWM on the dynamics for $\sigma = 50$, $\rho = -10$, $\delta_0 = -6.7$, $\delta_1 = -7$, $P_1 = 0.2$. (a) Bifurcation diagram of I_0 versus P_0, stable outputs are in black, while the maxima and minima of the oscillatory output are in red and blue, respectively. The green plot corresponds to $F_i = 0$ and magenta is for the stationary state. The pump power is first increased in (a), then decreased in (b), in order to reproduce the hysteresis response of the system. The presence of the unstable branch "hide" some of the oscillating states that are not achievable when moving forward with pump power, but reachable when moving backward. Those oscillations are due to XPM in the range $P_0 = [1.5, 5]$ and to the FWM above the value of $P_0 = 5$. (c) and (d) report the dynamical output and the phase portraits respectively, for all the cavity fields, fixing $P_0 = 17$.

In order to reproduce the hysteresis loop, we simulate an increase of the circulating power followed by a decreasing[4] inside the microcavity and report the outcomes in Fig. 4.17 for the case of $\delta_0 = -6.7$, $\delta_1 = -7$ and $I_1 = 0.2$.

The stable states are represented in magenta colour while the green line considers the system 4.21 without FWM terms. In Fig. 4.17 (a) we note that there are oscillating states, as well as some stable states, that cannot be reached when moving forward because of the presence of the unstable branch. Conversely, such states are achievable when moving backwards in Fig. 4.17 (b), as they are located on the upper bi-stable branch. Moreover, we have to consider the further role played by the FWM, whose effects can be distinguished from those deriving from other nonlinearities, e.g. XPM. This appears clear having a look at the bifurcations diagrams (a) and (b) in Fig. 4.18, obtained for $\sigma = 50$, $\rho = -10$, $\delta_0 = -6.7$, $\delta_1 = -7$, $P_1 = 0.2$, in which we can observe the location of critical points on the equilibrium curve and how those are reallocated via FWM.

Figure 4.18. Bifurcation diagram I_0 versus P_0 of the stationary states for $\sigma = 50$, $\rho = -10$, $\delta_0 = -6.7$, $\delta_1 = -7$, $P_1 = 0.2$. FWM is able to relocate bifurcations into the parameter space, modifying the critical values (P_0, I_0) showing Fold and Hops bifurcations. In (a), including FWM contribution, we have two LP bifurcations (yellow marks) at $P_0^{LP_1} = 0.7$ and $P_0^{LP_2} = 5$, respectively and two Hopf bifurcations (red dots) at $P_0^{H_1} = 1.6$ and $P_0^{H_2} = 15.7$, respectively. In (b), by neglecting the FWM terms, the critical points for the Hopf bifurcations are $\tilde{P}_0^{H_1} = 1.5$ and $\tilde{P}_0^{H_2} = 5.4$, while the LP critical points remain practically unchanged.

In details, in Fig. 4.18 (a), where the FWM is taken into account, we have two-fold bifurcations, LPs, at $P_0^{LP_1} = 0.7$ and $P_0^{LP_2} = 5$ respectively, delimiting the unstable branch; a first Hopf bifurcation at $P_0^{H_1} = 1.6$ and the second one at $P_0^{H_2} = 15.7$, so that the system achieves SP in the range of $P_0 = [1.6, 15.7]$. On the other hand, when we have only XPM contribution, as in Fig. 4.18 (b), one of the critical point for Hopf bifurcation is located at $\tilde{P}_0^{H_1} = 1.5$ (very close to the previous value, $P_0^{H_1} = 1.6$), while the second critical point for another Hopf bifurcation is located at $\tilde{P}_0^{H_2} = 5.4$,

---

[4]we use the terminology "forward" or "backwards" to indicate an increase or a decrease of circulating power

so that the system achieves the oscillating states in the range of $P_0 = [1.5, 5.4]$. Therefore, the self-pulsing branch is substantially modified by the presence of the FWM, while the unstable one remains pretty much unchanged. However, in both cases (Fig. 4.18 (a) and (b)), there are critical points for Hopf bifurcations that fall between LPs, making the dynamics more interesting. Notably is that the cavity fields show a very similar dynamical response, i.e. the dynamics are transferred from one mode to the other. This can be appreciated in fig 4.17 (c) and (d), in which the output (c) and the relative phase portraits (d) are plotted for $P_0 = 17$.

4.6.2 Case with $\rho > 0$

The analysis of stability presented in Fig. 4.11 and 4.12 of Section 4.5.2, has shown that the overlap between the self-pulsing and the unstable region affects the achievement of self oscillating dynamics for the set of parameter chosen ($\sigma = 50$, $\rho = 10$, $\delta_0 = 12$, $\delta_1 = 14$ and $I_1 = 0.1, 0.2$). For the same case, in Fig. 4.19 the bifurcations diagram is plotted by setting $P_1 = 0.2$ and varying the pump power P_0.

Figure 4.19. Bifurcation diagram I_0 versus P_0 of the stationary states for $\sigma = 50$, $\rho = 10$, $\delta_0 = 12$, $\delta_1 = 14$, $P_1 = 0.2$, reporting the stationary states curve of the full system in dashed magenta line, the equilibria when $F_i = 0$ in green. By varying the pump power P_0 there are two critical points corresponding to Hopf bifurcations (red dots) at $P_0^{H_1} = 4$ and $P_0^{H_2} = 9$ respectively. The latter bifurcations lie on the unstable branch, identified through LP bifurcations (yellow marks) at $P_0^{LP_1} = 1$ and $P_0^{LP_2} = 23$ respectively. Therefore, the critical points of the Hopf bifurcations are not accessible through hysteresis, while stationary solutions are achieved (black circles). For this set of parameter the FWM is not able to trigger SP (see green line).

We observe two Hopf bifurcations located at $P_0^{H_1} = 4$ and $P_0^{H_2} = 9$ respectively, on the unstable branch defined by LP bifurcations at $P_0^{LP_1} = 1$ and $P_0^{LP_2} = 23$, respectively. That's the reason for which oscillating states cannot be transferred onto the output, as the system immediately collapse to stable steady states on the lower energy branch (observe the black circles in Fig. 4.19). Neither exploiting the hysteresis and pumping backward nor increasing the signal intensity helps to reallocate the bifurcations to produce non trivial dynamics.

According to the stability map of Fig 4.14, we consider $\sigma = 1.5$, $\rho = 10$, $\delta_0 = 10.5$, $\delta_1 = 10$ and $P_1 = 0.6$ and realise the bifurcation diagrams I_0 versus P_0 in Fig. 4.20, in presence (a) and in absence (b) of FWM. In details, in Fig. 4.20 (a) we have two LP bifurcations at $P_0^{LP_1} = 0.4$ and $P_0^{LP_2} = 15$, and two Hopf bifurcations at $P_0^{H_1} = 3.3$ and $P_0^{H_2} = 47$. In Fig. 4.20 (b), the locations of the critical points for LPs remain pretty much the same as in (b), where we achieve two LP bifurcations at $\tilde{P}_0^{LP_1} = 0.3$ and $\tilde{P}_0^{LP_2} = 15$ respectively, while for the Hopf bifurcations we have a slightly change of the critical points, being $\tilde{P}_0^{H_1} = 5.2$ and $\tilde{P}_0^{H_2} = 53.2$, respectively.
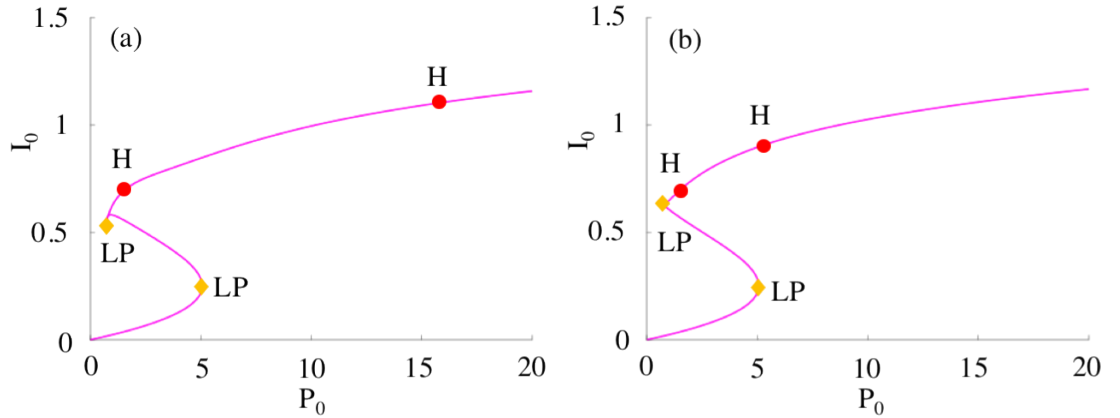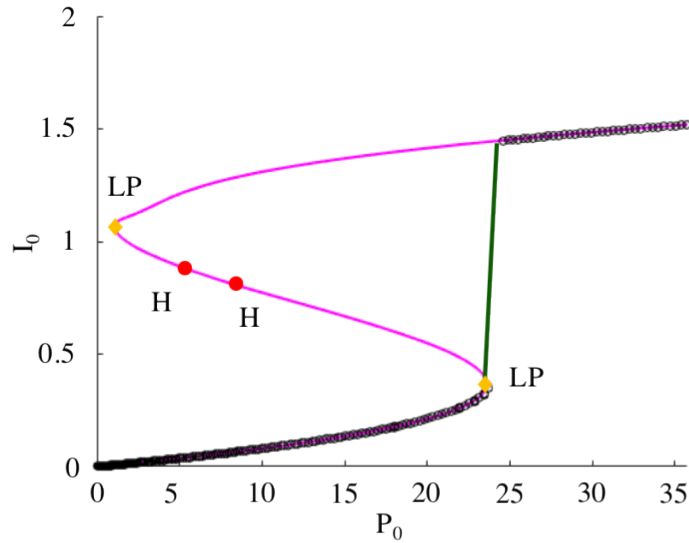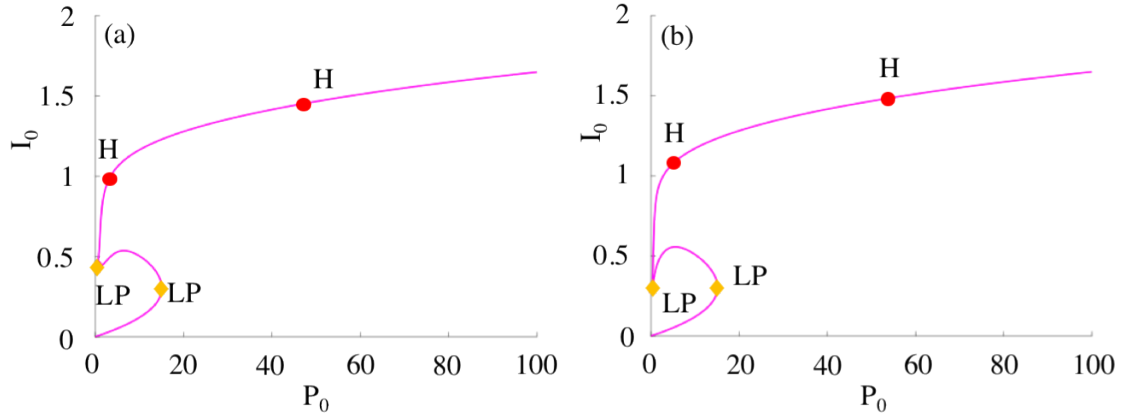

Figure 4.20. Bifurcation diagram I_0 versus P_0 of the stationary states for $\sigma = 1.5$, $\rho = 10$, $\delta_0 = 10.5$, $\delta_1 = 10$, $P_1 = 0.6$. In (a), including FWM contribution, we have two LP bifurcations (yellow marks) at $P_0^{LP_1} = 0.4$ and $P_0^{LP_2} = 15$, and two Hopf bifurcations (red dots) at $P_0^{H_1} = 3.3$ and $P_0^{H_2} = 47$. In (b), neglecting FWM terms, the critical point for the Hopf bifurcation are $\tilde{P}_0^{H_1} = 5.2$ and $\tilde{P}_0^{H_2} = 53.2$, while the LP critical point are $\tilde{P}_0^{LP_1} = 0.3$ and $\tilde{P}_0^{LP_2} = 15$. FWM slightly relocates the bifurcations into the parameter space, modifying the critical values (P_0, I_0).

For the same set of parameters ($\sigma = 1.5$, $\rho = 10$, $\delta_0 = 10.5$, $\delta_1 = 10$ and $P_1 = 0.6$), in Fig. 4.21 (a) the bifurcation diagram is shown, including the equilibrium solutions in magenta, the stationary solutions with $S_1(t) = 0$ in yellow, the stationary solution states without FWM terms in green. Self-pulsing regimes are achievable for energies still comparable with the bi-stability threshold energy, which is ≈ 0.12. The phase portraits of the bifurcation diagrams for P_0 against $Re[a_0]$ and $Im[a_0]$ in Fig. 4.21 (b) and (d) show that the Hopf bifurcation at $P_0 \approx 3.3$ gives birth to a stable

limit cycle, whose size decrease as the power increases. Consequently, oscillations are observed on the output in Fig. 4.21 (c), whose amplitudes and periods correspond to those of the limit cycle. The latter is represented in Fig. 4.21 (d) for different values of P_0. The limit cycle is extinguished at $P_0 \approx 47$ (corresponding to $P_0 = P_0^{H_2}$). It it noteworthy that when $S_1(t) = 0$ (only considering the pump) the SP states disappears at $P_0 \approx 80$, rather than $P_0 = 47$.
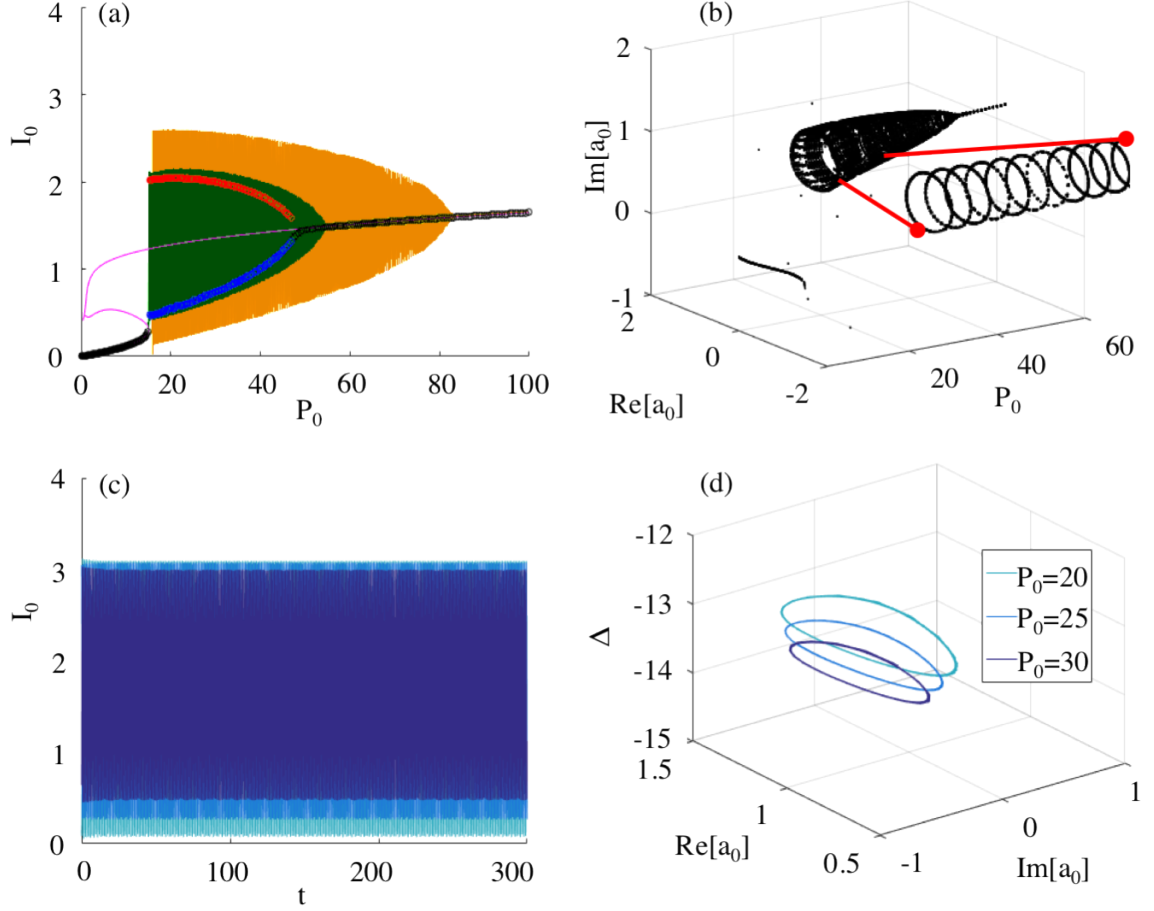
Figure 4.21. Dynamical response at increasing values of P_0 for $\sigma = 1.5, \rho = 10$, $\delta_0 = 10.5$, $\delta_1 = 10$, $P_1 = 0.6$. (a) Bifurcation diagram of I_0 versus P_0, stable outputs are in black, while the maxima and minima of the oscillatory output are in red and blue, respectively. The yellow plot is for $S_1 = 0$, green corresponds to $F_i = 0$ and magenta is for the stationary state. (b) Phase portrait of the bifurcation diagram for P_0 against $Re[a_0]$ and $Im[a_0]$. (c) Time evolution of I_0 at $P_0 = 20, 25, 30$ from dark to light blue, respectively, and (d) long term phase plots for Δ versus $Re[a_0]$ and $Im[a_0]$.

Now, we analyse how the hysteresis may affect the response. In Fig. 4.22 (a), as we move forward with P_0, initially, the system reaches stationary stable states, then approaches the switching threshold given by the LP point at $P_0 = 15$. If we further increase the power, the system jumps from the lower stable branch to the upper self-stable branch. Here, there is a heteroclinic orbit that connects the saddle points of the unstable branch to the limit cycle, produced through the Hopf bifurcation at $P_0 = 3.3$. Finally, the system reaches again stable equilibria for $P_0 > 47$, where the limit cycle

disappears. On the other hand, starting from equilibria located on the upper stable branch, when we decrease the power P_0 (backward) in Fig. 4.22 (b), the output is first stable, then self-stable, corresponding to the portion of branch between the Hopf bifurcations ($P_0 = [3.3, 47]$). Following, the system becomes stable again before reaching the LP bifurcation at $P_0 = 0.4$ and switching to the lower stable branch.
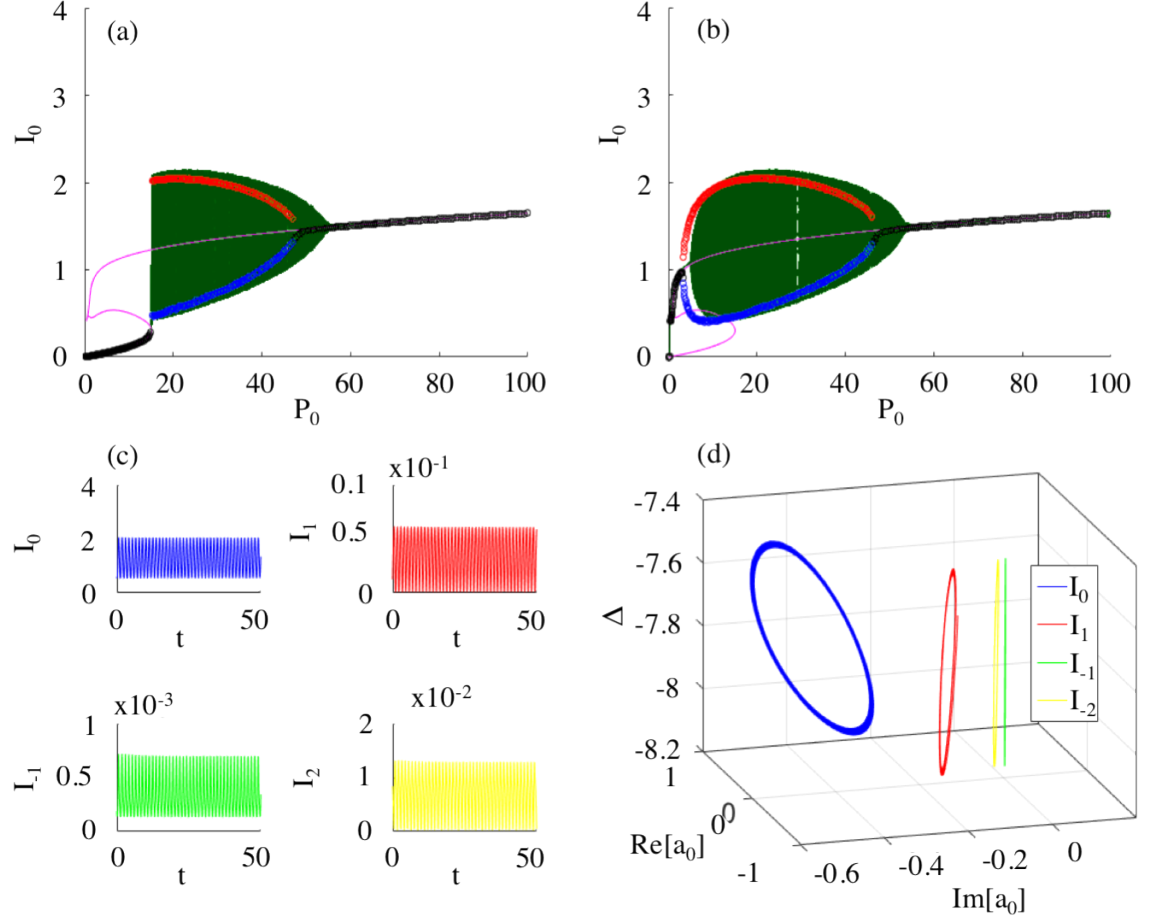
Figure 4.22. Effects of the bi-stability response and FWM on the dynamics for $\sigma = 1.5$, $\rho = 10$, $\delta_0 = 10.5$, $\delta_1 = 10$, $P_1 = 0.6$. (a) Bifurcation diagram of I_0 versus P_0, stable outputs are in black, while the maxima and minima of the oscillatory output are in red and blue, respectively. The green plot corresponds to $F_i = 0$ and magenta is for the stationary state. The pump power is increased in (a), then decreased in (b), in order to reproduce the hysteresis response of the system. Notable the influence of the FWM on the hysteresis region by comparing (a) with (b). (c) and (d) report the dynamical output and the phase portraits respectively, for all the cavity fields, with $P_0 = 20$.

4.7 Controlling and Transferring Nonlinear Regimes

To fully understand the possibility of controlling thermally-induced dynamics in our microresonator, we study the system's response in relation to an on/off signal, for different signal input powers. The results are shown in Fig. 4.23. We consider $\sigma = 50$, $\rho = -10$, $\delta_0 = -6.7$ and chose $\delta_1 = -7$

and $P_0 = 6$, for Fig. 4.23 (a) and (c) (corresponding to the case of Fig. 4.15), while $\delta_1 = -12$ and $P_0 = 18$ for Fig. 4.23 (b), (d) (corresponding to the case of Fig. 4.16). A homoclinic saddle-focus (Shilnikov orbits) and circular orbits (limit cycles) are observed, respectively, for a range of values of P_1. The system can repeatedly switch between stable and self-pulsing states, as the signal is turned on–off.
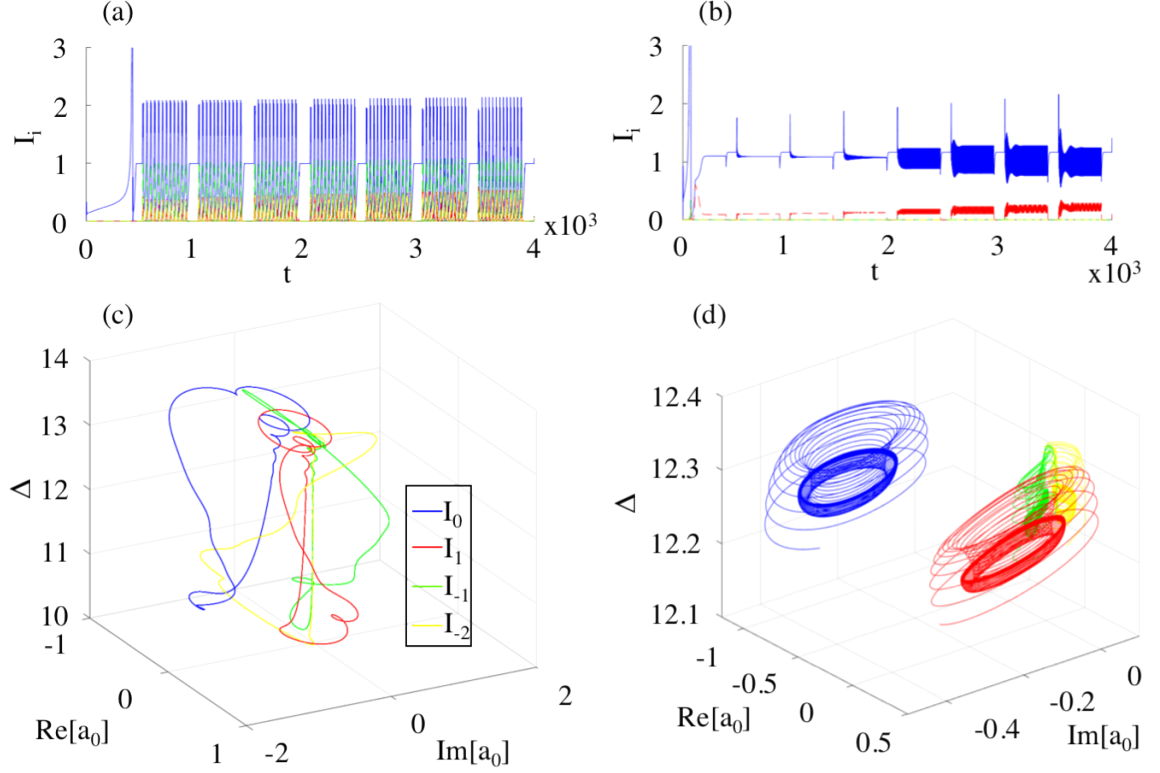
Figure 4.23. Time evolution for repeatedly on/off P_1 signal for $\sigma = 50$, $\rho = -10$, $\delta_0 = -6.7$. The range of parameters is chosen in the SP regions of Fig. 4.15 for (a), (c) $P_0 = 6$, $\delta_1 = -7$ and of 4.16 for (b), (d) $P_0 = 18$, $\delta_1 = -12$. Blue, red, green, and yellow are for the pump and signal first and second idler, respectively. (a) and (b) show the time response for the intra-cavity energies. P_1 is turned on and off repeatedly with power linearly increasing from 0.1 to 0.4 and from 0.1 to 0.6 in (a) and (b), respectively. (c) and (d) show a typical long-term phase portrait for P_1 0.3 and 0.5, respectively, showing the homoclinic saddle-focus (Shilnikov) and circular trajectories.

Finally, we study the role played by the FWM in a case involving chaotic dynamics, which can be observed by setting $\sigma = 1.5$, $\rho = -10$, $\delta_0 = -12$, $\delta_1 = -15$ and $P_1 = 0.6$. We obtain the graphs reported in Fig. 4.24, showing bifurcation diagrams in (a) and (b), phase portraits of the bifurcation diagram for P_0 against $Re[a_0]$ and $Im[a_0]$ in (c) and (d), the 2-d transverse sections of the phase portraits onto the plane $Re[a_0]$, $Im[a_0]$ for all P_0 values in (e) and (f). We consider the FWM contribution in the left graphs of Fig. 4.24, while neglecting FWM in the right graphs.

Let us assume the presence of the FWM and increase the pump power, moving on the equilibrium curve represented in Fig. 4.24 (a) from low to high values of P_0. As we see, the system has

stable solutions at low power until approaching an LP bifurcation at $P_0 = 28.8$. The latter produces saddles-nodes/foci equilibria, hence the unstable branch, delimited by the second LP bifurcation at $P_0 = 1.34$. Moreover, on the upper bi-stable branch, we have several Hopf bifurcations, in particular, some of them are very close to LPs (e.g the Hopf at $P_0 = 26.5$). Thus, in correspondence of the first LP point at $P_0 = 28.8$, the system becomes unstable. Consequently, its trajectory in the phase space tries to reach the nearest stable equilibrium with the closest energy value possible. The only accessible states, at this point, lie on the upper branch, where we have a Hopf bifurcation at about the same power value ($P_0 = 26.5$). What we achieve is an apparent chaotic behaviour, as shown in the phase portrait of the bifurcation diagram for P_0 against $Re[a_0]$ and $Im[a_0]$ in Fig. 4.24 (c). The theoretical background of Chapter 2 can support our analysis at this point: at the critical point for a LP ($P_0 = 28.8$), the unstable manifold of the saddle point approach the manifold of the limit cycle, as consequence of the bi-stability. When those manifolds with different stability are close enough (without intersect) can interact and repeatedly attract and repel nearby trajectories in a confined region of the phase space, producing bursts of chaos that may possibly settle down to a non-chaotic attractor after a very long transient. This particular behaviour is the typical signature of *intermittency*, that is one of the routes to reach chaos in a dynamical system. This phenomenon can involve local bifurcations, in our case saddle-node bifurcations. On the other hand, if we increase the power, the system gradually become periodic, as it appears in Fig. 4.24 (a) and (c). Specifically, from $P_0 \approx 67$ to $P_0 \approx 100$, we observe from Fig. 4.24 (a) the clear presence of multiple oscillating components, before reassembling a single-period limit cycle in the phase portrait (Fig. 4.24 (c)). This is known as *inverse-period doubling* bifurcation, which allows switching from chaotic regimes to periodic ones. The mechanism of period-doubling represents another route to chaos. If we plot the transverse sections for all P_0 values of the diagram (4.24 (c)), we can obtain the diagram of Fig. 4.24 (e), which includes all of the 3D phase portraits of Fig. (4.24 (c) projected onto the plane ($Re[a_0]$,$Im[a_0]$). We note that the trajectories are confined in a circular region of the phase space, bonded to the limit cycle of the Hopf bifurcation and chaotically distributed within.

At this point, let's investigate the dynamical response of the system at a specific P_0 value. Therefore, we set $P_0 = 60$ and consider the left graphs of Fig. 4.25. In Fig. 4.25 (a), the specific section of interest of the phase portrait is shown in red, while the output and long-term phase portraits are plotted in 4.25 (c) and (e) respectively. As the initial equilibrium that we chose is in the chaotic region, the output in Fig. 4.25 (c), and the relative 2D phase portraits in Fig. 4.25 (e), have irregular oscillations alternated by periodicity. This effect involves all cavity modes, resulting in

bursts of chaos modulated by a periodic component, according to the confinement of the trajectories in a region of the phase space, as we pointed out before. It is worthwhile to note that there is a "gradual" transition from chaos to periodicity, as the power approaches the LP point. This is a signature of period doubling mechanism.

By opportunely adjusting the coupling of the signal, the previous scenario can be modified. The exclusion of the FWM terms from Eqs. 4.21 strongly affects the bifurcations in the parameter space, as shown in Fig. 4.24 (b). Here, we observe a Hopf bifurcation at $P_0 = 14.3$, therefore the chaotic region is confined in a smaller region of the parameter space with respect to the previous case, as it appears in Fig. 4.24 (d). This can be further proved by comparing the diagrams of Fig. 4.24 (e) with Fig. 4.24 (f).

In Fig. 4.25 (d), the equilibrium chosen at $P_0 = 60$, previously chaotic, shows a periodic behovior now. It resembles a period-2 output on the pump (blue curve), while it appears to have single period on the signal (red curve). By looking at the 3D phase portrait in Fig. 4.25 (f), we realise that the signal actually has a period-2 orbit, as the attractor presents a folded part. However, such a folding is very small compared to rest of the attractor. On the contrary, the pump attractor has a well-defined *figure-eight* shape, like the Lorenz attractor [182]. This is a remarkable example that shows the FWM affecting chaotic dynamics, allowing to switch from chaos to periodicity.

If we keep unchanged all parameters of the previous examples, except the pump power and assume another initial equilibrium, having $P_0 = 84$, we obtain the graphs reported in Fig. 4.26. Comparing the left with the right diagrams, we observe that the system can switch from a chaotic to a periodic regime, with period-1 output.

From the results we may conclude that chaotic regimes are more likely to be achieved with a small value of σ, which regulates the damping of thermal oscillation. Therefore, when the damping on the thermal oscillations is weak, chaotic dynamics take place. We considered the case of Kerr and thermo-optic coefficients of the opposite sign, however, chaotic regimes might be reached even in systems with positive ρ values.
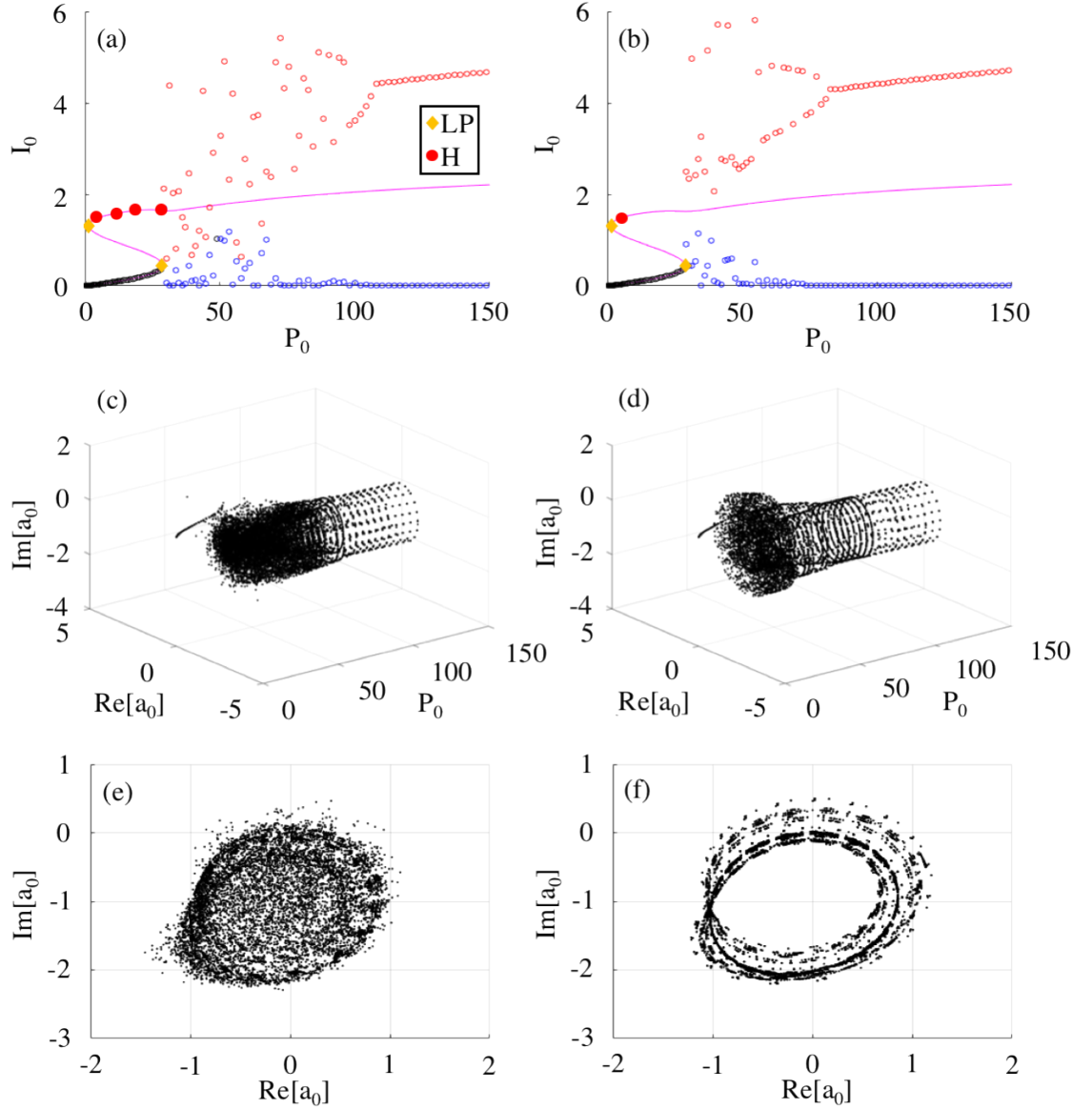
Figure 4.24. Chaotic dynamics controlled by FWM for $\sigma = 1.5$, $\rho = -10$, $\delta_0 = -12$, $\delta_1 = -15$, $P_1 = 0.6$. The situation depicted in the left graphs (a), (c) and (e) takes into account the effects of the FWM, conversely to the right graphs (b), (d) and (f), in which the FWM contribution is neglected. Bifurcation diagrams I_0 versus P_0 are plotted in (a) and (b), reporting stable outputs in black, while the maxima and minima of the oscillatory output in red and blue, respectively. The curve of the stationary states is in magenta. Phase portrait of the bifurcation diagrams are represented in (c) and (d), their transverse sections onto the plane ($Re[a_0]$,$Im[a_0]$) for all P_0-values, in (e) and (f). In presence of FWM, chaotic behaviour is observed in the range $P_0 = [30, 67]$, while in absence of FWM the range is reduced to $P_0 = [30, 52]$. This corresponds to a reajustment of the bifurcation into the space parameter.
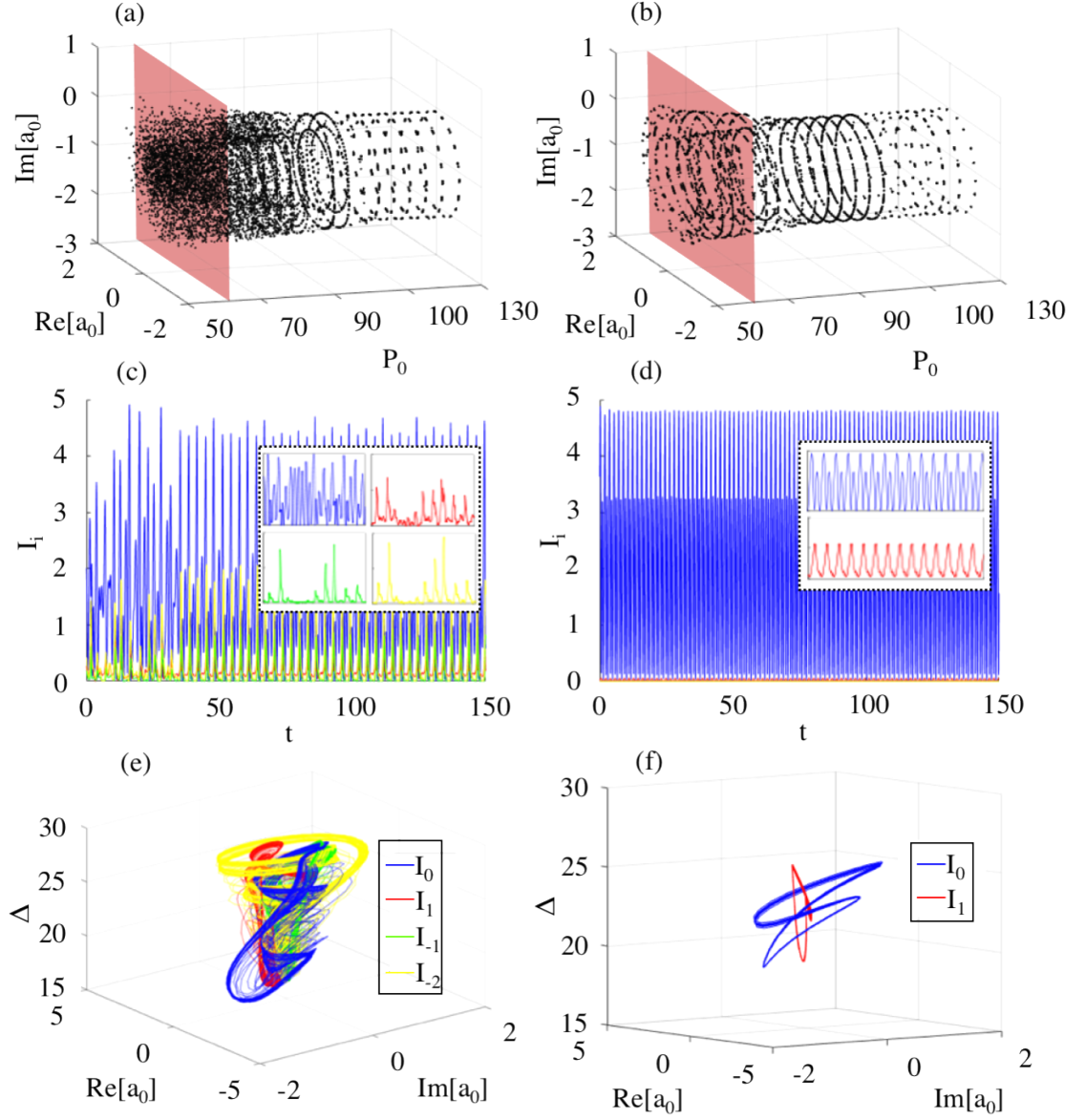
Figure 4.25. Chaotic dynamics controlled by FWM, specific case for $\sigma = -1.5$, $\rho = -10$, $\delta_0 = -12$, $\delta_1 = -15$, $P_0 = 60$, $P_1 = 0.6$. The situation depicted in the left graphs (a,c,e) takes into account the effects of the FWM, conversely to the right graphs (b,d,f) in which the FWM contribution is neglected. In (a) and (b) bifurcation diagrams I_0 versus P_0 show the correspondent sections of interest of the phase space $(Re[a_0], Im[a_0])$. Correspondent dynamic of the intra-cavity energy associated to the output fields in (c) and (d), with inserts reporting the detail of the oscillations. Long term phase plots for Δ versus $Re[a_0]$ and $Im[a_0]$ in (e) and (f).
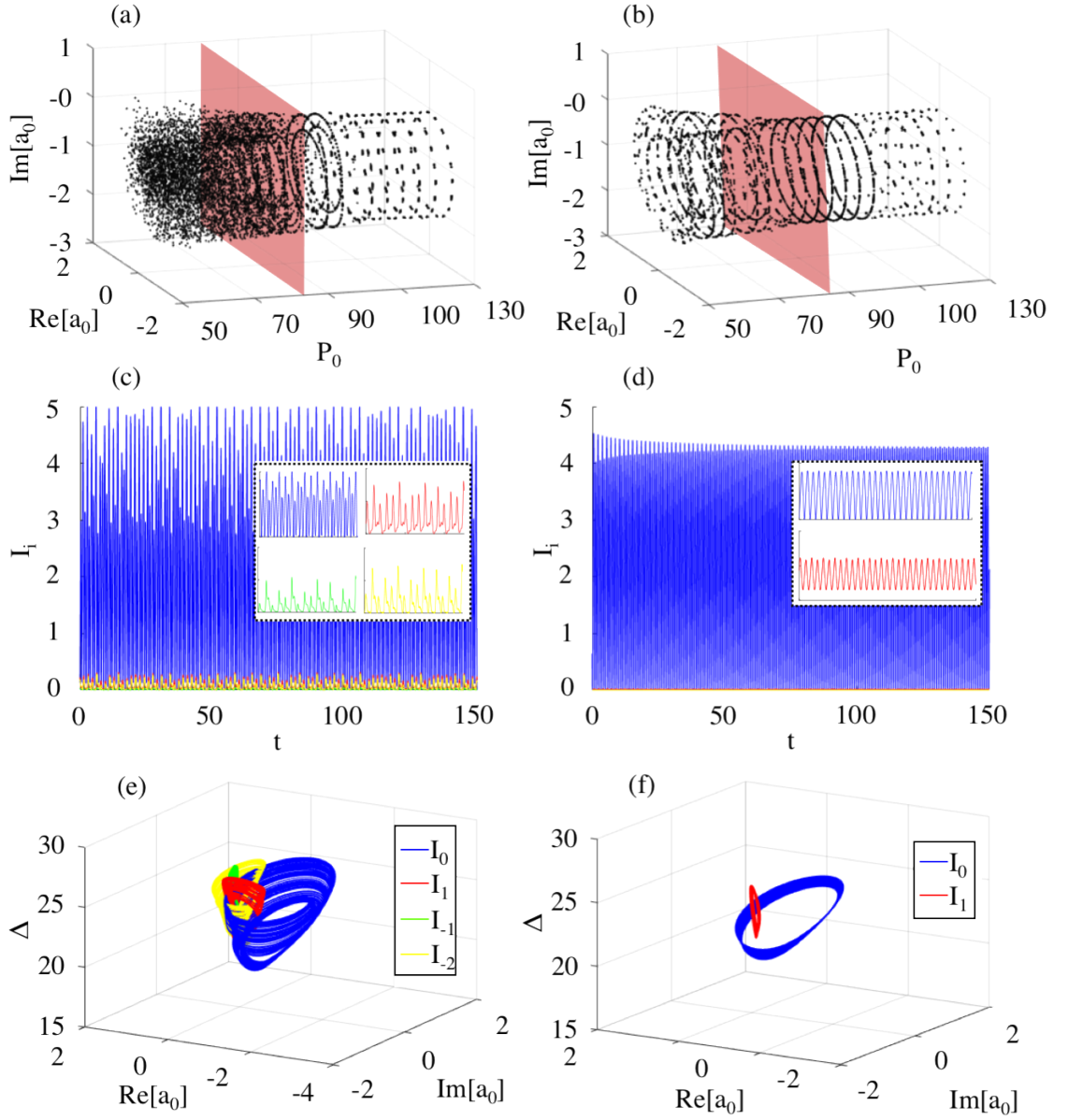
Figure 4.26. Chaotic dynamics controlled by FWM, specific case for $\sigma = -1.5$, $\rho = -10$, $\delta_0 = -12$, $\delta_1 = -15$, $P_0 = 84$, $P_1 = 0.6$. The situation depicted in the left graphs (a,c,e) takes into account the effects of the FWM, conversely to the right graphs (b,d,f) in which the FWM contribution is neglected. In (a) and (b) bifurcation diagrams I_0 versus P_0 show the correspondent sections of interest of the phase space $(Re[a_0], Im[a_0])$. Correspondent dynamic of the intra-cavity energy associated to the output fields in (c) and (d), with inserts reporting the detail of the oscillations. Long term phase plots for Δ versus $Re[a_0]$ and $Im[a_0]$ in (e) and (f).

Chapter 5

Conclusions

The aim of this work was to demonstrate a novel approach to control nonlinear regimes in optical microcavities, exhibiting a time-dependent nonlinearity with a first-order time response, such as a thermo-optical nonlinearity, in presence of Kerr effect. In order to achieve our goal, in Chapter 1, the concept of whispering-gallery-mode, which laid the basis for the development of optical microcavities, has been introduced. An overview of the fabrication techniques, suitable to produce the state of the art microresonators, either in monolithic bulk technology or on-chip for integrated photonics platforms, has been provided. Improvements over the years and new materials, shapes and geometries have produced a number of advantages in terms of performance, compactness/portability and costs. Those aspects are strictly connected with a wide range of applications achievable with microcavities. Therefore, it is essential to perform a study of the stability of the equilibria of the system in terms of significant parameters, in order to predict its operational regimes.

It is possible to define the boundaries of the equilibrium regions and locate critical points at which the system shows a drastic change of its dynamical pattern, hence bifurcations in the parameter space. This falls under the domain of the "Dynamical System Theory" for parameter-dependent multidimensional nonlinear dynamical systems, which has been qualitatively discussed in Chapter 2.

The model equations describing our microresonator has been derived in Chapter 3, within the framework of the coupled-mode theory for homogeneous, isotropic, dispersionless microresonators, including nonlinear contributions of energy exchange among cavity modes due to the Kerr effect and a slow response nonlinearity, in the specific, the thermo-optical nonlinearity.

In Chapter 4, the results of our approach have been presented and the model tested, considering, initially, the simple situation of a single frequency continuous-wave pumping. In this regards,

analytic expressions for the energy boundaries of the unstable and self-pulsing region have been defined. Critical detuning values, corresponding to specific codim-1 bifurcations occurring in the parameter space (e.g. Hopf, Shilnikov), have been found. Noteworthy is that the ratio between the characteristic relaxation time and the nonlinear coefficients of Kerr and thermo-optic effect (σ/ρ) is fundamental to adjust the overlap and boundaries of the equilibrium regions.

When a configuration involving two-frequency continuous-wave optical fields is achieved, it has been proven that a weak signal governs the nonlinear behaviour of a strong pump, through the presence of four-wave mixing. Desirable dynamics can be triggered and controlled at low power by coupling an additional continuous-wave field (signal) into the microcavity. The latter's presence can effectively influence the interaction among different nonlinearities (in our case Kerr and thermo-optical) through the four-wave mixing action. Hence, the effect of a week signal onto the system, within different regions of the parameter space, has been investigated considering, in particular, either negative or positive thermo-optical coefficients, and taking into account potential materials that might be employed for the fabrication of the cavity. The stability maps and bifurcation diagrams produced, as well as the phase portraits of the cavity fields plotted, are strongly affected when the idler is resonantly coupled, therefore when the four-wave mixing has high efficiency. This can be exploited to transfer dynamics between cavity modes as well.

With practical examples, it has been demonstrated that, by acting on the intensity of the signal, thermal instabilities can be modulated, allowing self-oscillations to be turned off and on, as well as controlled in amplitude and shape. Chaotic regimes in a confined region of the phase space, under particular conditions, can be observed.

The outcomes of this work prove that new strategies for designing efficient microcavity-based oscillators and sensors for metrology [87], biology [183] are achievable. The possibility of changing the equilibria of a microcavity and trigger specific dynamics at will has profound implications. For instance, an effective control of the thermal instabilities through our scheme "pump/signal" could have applications for the next-generation of communication and information processing devices [184], including all-optical switches [55, 185, 186], modulators [64] and filters [15]. The coupled signal can adjust LP bifurcations defining the bi-stable branch, hence change the bi-stability threshold. The latter effect might be exploited to build single-wavelength optical memories for all-optical signal processing using microcavities [187].

The dynamics of coherent regimes, such as temporal cavity solitons in passive microcavities [82, 188, 189], are affected by thermal instabilities. Therefore, it is essential governing such effect

when realising devices for parallel wavelength-division multiplexing in high-speed communications [190, 191] and for the generation of highly stable broadband frequency combs [192, 175].

Our approach could be also implemented for chaos-based communication systems, where the control of chaotic regimes is a relevant subject of study. As the chaotic signals are noiselike and broadband [193], they are difficult to predict, thus they appear to be potentially useful for secure data communication, in which the synchronization of nonlinear and chaotic systems provide a way to encode data packets over fibre transmission for optical cryptography [194–196], as well as for wireless radio frequency transmission [197]. This is possible through opportune encryption schemes, such as chaos masking [198], chaos shift keying [199] and chaos modulation [200, 201].

Bibliography

[1] T. Carmon, Lan Yang, and K. J. Vahala. Dynamical thermal behavior and thermal self-stability of microcavities. In *Opt. Express*, volume 3, pages 2019–2021 Vol. 3, May 2005.

[2] Stefania Malaguti, Gaetano Bellanca, Alfredo de Rossi, Sylvain Combrié, and Stefano Trillo. Self-pulsing driven by two-photon absorption in semiconductor nanocavities. *Physical Review A*, 83.

[3] Özdal Boyraz, Prakash Koonath, Varun Raghunathan, and Bahram Jalali. All optical switching and continuum generation in silicon waveguides. *Opt. Express*, 12:4094.

[4] Pramod Kumar, Awadhesh Prasad, and R. Ghosh. Strange bifurcation and phase-locked dynamics in mutually coupled diode laser systems. *Journal of Physics B*, 42:145401, 2009.

[5] V.S. Il'chenlo and M.L. Gorodetskii. Thermal nonlinear effects in optical whispering gallery microresonators. *Laser Physics*, 2(6), 1992.

[6] Alexey E. Fomin, Michael L. Gorodetsky, Ivan S. Grudinin, and Vladimir S. Ilchenko. Nonstationary nonlinear effects in optical microspheres. *J. Opt. Soc. Am. B*, 22:459, 2005.

[7] Ivan S. Grudinin and Kerry J. Vahala. Thermal instability of a compound resonator. 17: 14088, 2009.

[8] A.C. Turner, M.A. Foster, A.L. Gaeta, and M Lipson. Ultra-low power parametric frequency conversion in a silicon microring resonator. *Optics Express*, 16:4881–4887, 2008.

[9] M. Ferrera, L. Razzari, D. Duchesne, R. Morandotti, Z. Yang, M. Liscidini, J. E. Sipe, S. Chu, B. E. Little, and D. J Moss. Low-power continuous-wave nonlinear optics in doped silica glass integrated waveguide structures. *Nature Photonics*, 2:737–740, 2008.

[10] L Rayleigh. *Scientific Papers*, 1900.

[11] D. Colladon. On the reflections of a ray of light inside a parabolic liquid stream. *Compt. Rend*, 15:800–802, 1842.

[12] L. Brekhovskikh. Reflection of spherical waves at weak interfaces. *Sov. Phys. Acoust.*, 13 (462), 1968.

[13] D. W. McLaughlin, J. V. Moloney, and A. C. Newell. New class of instabilities in passive optical cavities. *Physical review letters*, 54(7):681, 1985.

[14] S.L. McCall, A.F.J. Levi, R.E. Slusher, S.J. Pearton, and R.A Logan. Whispering-gallery mode microdisk lasers. *Applied Physics Letters*, 60:289–291, 1992.

[15] K. Djordjev, S.-J. Choi, S.-J. Choi, and P.D Dapkus. Microdisk tunable resonant filters and switches. *IEEE Photonics Technology Letters*, 14:828–830, 2002.

[16] Borselli, Matthew, Srinivasan, Kartik, Barclay, Paul E, Painter, and Oskar. Rayleigh scattering, mode coupling, and optical loss in silicon microdisks. *Applied Physics Letters*, 85(17): 3693–3695, 2004.

[17] D.K. Armani, T.J. Kippenberg, S.M. Spillane, and K.J Vahala. Ultra-high-q toroid microcavity on a chip. *Nature*, 421:925–928, 2003.

[18] Armani, Deniz, Min, Bumki, Martin, Andrea, Vahala, and Kerry J. Electrical thermo-optic tuning of ultrahigh-q microtoroid resonators. *Applied physics letters*, 85(22):5439–5441, 2004.

[19] Kippenberg, TJ, Spillane, SM, Vahala, and KJ. Kerr-nonlinearity optical parametric oscillation in an ultrahigh-q toroid microcavity. *Physical review letters*, 93(8):083904, 2004.

[20] M. Hossein-Zadeh and K.J Vahala. Free ultra-high-q microtoroid: A tool for designing photonic devices. *Optics Express*, 15:166–175, 2007.

[21] Han-Youl Ryu, Kim, Se-Heon, Park, Hong-Gyu, Hwang, Jeong-Ki, Lee, Yong-Hee, and Jeong-Soo Kim. Square-lattice photonic band-gap single-cell laser operating in the lowest-order whispering gallery mode. *Applied physics letters*, 80(21):3883–3885, 2002.

[22] Srinivasan, Kartik, Barclay, Paul E, Painter, Oskar, Chen, Jianxin, Cho, Alfred Y, Gmachl, and Claire. Experimental demonstration of a high quality factor photonic crystal microcavity. *Applied Physics Letters*, 83(10):1915–1917, 2003.

[23] Lee, Po-Tsung, Lu, Tsan-Wen, Fan, Jyun-Hao, Tsai, and Feng-Mao. High quality factor microcavity lasers realized by circular photonic crystal with isotropic photonic band gap effect. *Applied physics letters*, 90(15):151125, 2007.

[24] M Sumetsky. Whispering-gallery-bottle microcavities: the three-dimensional etalon. *Optics letters*, 29(1):8–10, 2004.

[25] Ganapathy Senthil Murugan, Wilkinson, James S, Zervas, and Michalis N. Optical excitation and probing of whispering gallery modes in bottle microresonators: potential for all-fiber add–drop filters. *Optics letters*, 35(11):1893–1895, 2010.

[26] Sumetsky, M, Dulashko, Y, Windeler, and RS. Super free spectral range tunable optical microbubble resonator. *Optics letters*, 35(11):1866–1868, 2010.

[27] Sumetsky, Misha, Dulashko, Y, Windeler, and RS. Optical microbubble resonator. *Optics letters*, 35(7):898–900, 2010.

[28] Li, Hao, Guo, Yunbo, Sun, Yuze, Reddy, Karthik, and Xudong Fan. Analysis of single nanoparticle detection by using 3-dimensionally confined optofluidic ring resonators. *Optics express*, 18(24):25081–25088, 2010.

[29] G. C. Righini, Y.Dumeige, P. F'eron, M. Ferrariand G. Nunzi Conti, D. Ristic, and S. Soria. Whispering gallery mode microresonators: Fundamentalsand applications. *Rivista del Nuovo Cimento*, 34(7), 2011.

[30] Anatoliy A. Savchenkov, Andrey B. Matsko, Vladimir S. Ilchenko, and Lute Maleki. Optical resonators with ten million finesse. *Optics Express*, 15:6768–6773, 2007.

[31] Amnon Yariv. Coupled-mode theory for guided-wave optics. *IEEE Journal of Quantum Electronics*, 9(9):919–933, 1973.

[32] Birks, TA, Knight, JC, Dimmick, and TE. High-resolution measurement of the fiber diameter variations using whispering gallery modes and no optical alignment. *IEEE Photonics Technology Letters*, 12(2):182–183, 2000.

[33] Sumetsky, Misha, Dulashko, and Yury. Sensing an optical fiber surface by a microfiber with angstrom accuracy. In *Optical Fiber Communication Conference*, page OTuL6. Optical Society of America, 2006.

[34] Andrew W. Poon, Richard K. Chang, and James A. Lock. Spiral morphology-dependent resonances in an optical fiber: effects of fiber tilt and focused gaussian beam illumination. 23:1105, 1998.

[35] V. B. Braginsky, M. L. Gorodetsky, and V. S. Ilchenko. Quality-factor and nonlinear properties of optical whispering-gallery modes. *Physics Letters A*, 137:393–397, 1989.

[36] Mikhail L. Gorodetsky, Anatoly A. Savchenkov, and Vladimir S Ilchenko. Ultimate q of optical microsphere resonators. *Optics Letters*, 21:453–455, 1996.

[37] G. Nunzi Conti, A. Chiasera, L. Ghisa, S. Berneschi, M. Brenci, Y. Dumeige, S. Pelli, S. Sebastiani, P. Feron, M. Ferrari, and G. C. Righini. Spectroscopic and lasing properties of er3+-doped glass microspheres. 352:2360–2363, 2006.

[38] Ioan Bica. Formation of glass microspheres with rotating electrical arc. 77:210–212, 2000.

[39] Ming Cai, Oskar Painter, and Kerry J. Vahala. Observation of critical coupling in a fiber taper to a silica-microsphere whispering-gallery mode system. 85:74–77. ISSN 0031-9007. doi: 10.1103/physrevlett.85.74.

[40] Scott B. Papp, Pascal Del'Haye, and Scott A Diddams. Mechanical control of a microrod-resonator optical frequency comb. *Physical Review X*, 3:031003, 2013.

[41] M. L. Gorodetsky, A. A. Savchenkov, and V. S. Ilchenko. Ultimate q of optical microsphere resonators. *Opt. Lett.*, 21:453, 1996.

[42] D. W. Vernooy, A. Furusawa, N. P. Georgiades, V. S. Ilchenko, and H. J Kimble. Cavity QED with high-q whispering gallery modes. *Physical Review A*, 57:R2293–R2296, 1998.

[43] V.S. Ilchenko, A.A. Savchenkov, A.B. Matsko, and L Maleki. Nonlinear optics and crystalline whispering gallery mode cavities. *Physical Review Letters*, 92:439031–439034, 2004.

[44] Aurélien Coillet, Rémi Henriet, Kien Phan Huy, Maxime Jacquot, Luca Furfaro, Irina Balakireva, Laurent Larger, and Yanne K Chembo. Microwave photonics systems based on whispering-gallery-mode resonators. *Journal of Visualized Experiments : JoVE*, 78:50423, 2013.

[45] Anatoliy A. Savchenkov, Andrey B. Matsko, Vladimir S. Ilchenko, and Lute Maleki. On the fundamental limits of q factor of crystalline dielectric resonators. *Optics Express*, 15:6768, 2007.

[46] R. Won and M. Paniccia. Integrating silicon photonics. *Nature Photonics*, 4:498–499, 2010.

[47] Tom Baehr-Jones, Thierry Pinguet, Patrick L. Guo-Qiang, Steven Danziger, Dennis Prather, and Michael Hochberg. Myths and rumours of silicon photonics. *Nature Photonics*, 6: 206–208, 2012.

[48] F. Gholami, S. Zlatanovic, A. Simic, L. Liu, D. Borlaug, N. Alic, M. P. Nezhad, Y. Fainman, and S Radic. Third-order nonlinearity in silicon beyond 2350 nm. *Applied Physics Letters*, 99:081102, 2011.

[49] Q. Lin, J. Zhang, G. Piredda, R. W. Boyd, P. M. Fauchet, and G. P. Agrawal. Dispersion of silicon nonlinearities in the near infrared region. *Applied Physics Letters*, 91:021111, 2007.

[50] M. Dinu, F. Quochi, and H Garcia. Third-order nonlinearities in silicon at telecom wavelengths. *Applied Physics Letters*, 82:2954–2956, 2003.

[51] D. J. Moss, R. Morandotti, A. L. Gaeta, and M. Lipson. New cmos-compatible platforms based on silicon nitride and hydex for nonlinear optics. *Nature Photonics*, 7:597–607, 2013.

[52] David J. Moss, Alessia Pasquazi, Marco Peccianti, Luca Razzari, David Duchesne, Marcello Ferrera, S. Chu, B. E. Little, and Roberto Morandotti. Hydex waveguides for nonlinear optics. doi: 10.1117/12.876964.

[53] M. Ferrera, L. Razzari, D. Duchesne, R. Morandotti, Z. Yang, M. Liscidini, J. E. Sipe, S. Chu, B. E. Little, and D. J. Moss. Low-power continuous-wave nonlinear optics in doped silica glass integrated waveguide structures. 2:737–740, 2008. ISSN 1749-4885. doi: 10.1038/nphoton.2008.228.

[54] H. A. Haus. *Waves and Fields in Optoelectronics*. Series in Solid State Physical Electronics. 1984.

[55] P. Rabiei, W.H. Steier, C. Zhang, and L.R Dalton. Polymer micro-ring filters and modulators. *Journal of Lightwave Technology*, 20:1968–1975, 2002.

[56] Jiang Li, Scott Diddams, and Kerry J. Vahala. Pump frequency noise coupling into a microcavity by thermo-optic locking. 22:14559, 2014.

[57] Bo Zhang, David Leuenberger, Ming-Chang M. Lee, Alan E. Willner, and Ming C. Wu. Experimental demonstration of dynamic bandwidth allocation using a mems-actuated bandwidth-tunable microdisk resonator filter. 19:1508–1510, 2007.

[58] M. Mancinelli, P. Bettotti, J.M. Fedeli, and L. Pavesi. Reconfigurable optical routers based on coupled resonators induced transparencey resonances. 20:23856, 2012.

[59] W. Yoshiki, Y.Honda, T. Tetsumoto, K. Furusawa, N. Sekine, and T. Tanabe. All-optical tunable buffering with coupled ultra-high q whispering gallery mode microcavities. *Scientific Reports*, 7(10688), 2017.

[60] A. E. Willner, S. Khaleghi, M. R. Chitgarha, and O. F. Yilmaz. All-optical signal processing. *Journal of Lightwave Technology*, 32(4):660–680, 2014.

[61] Saleh and Simmons. Evolution toward the next-generation core optical network. 24:3303–3321, 2006.

[62] B.E. Little, S.T. Chu, P.P. Absil, J.V. Hryniewicz, F.G. Johnson, F. Seiferth, D. Gill, V. Van, O. King, and M Trakalo. Very high-order microring resonator filters for wdm applications. *Photonics Technology Letters, IEEE*, 16:2263–2265, 2004.

[63] Shijun Xiao, Maroof H. Khan, Hao Shen, and Minghao Qi. Multiple-channel silicon micro-resonator based filters for wdm applications. 15:7489, 2007.

[64] Yurii A. Vlasov, William M. J. Green, Solomon Assefa, Joris van Campenhout, Young-Hee Kim, and Fengnian Xia. Silicon integrated nanophotonics for on-chip optical interconnects, 2008.

[65] Xiyuan Lu, Steven Rogers, Thomas Gerrits, Wei C. Jiang, Sae Woo Nam, and Qiang Lin. Heralding single photons from a high-q silicon microdisk. 3:1331, 2016.

[66] T. Herr, K. Hartinger, and J Riemensberger. Universal formation dynamics and noise of kerr-frequency combs in microresonators. *Nature Photonics*, 6:480–487, 2012.

[67] P. Del'Haye, T. Herr, E. Gavartin, M.L. Gorodetsky, R. Holzwarth, and T.J Kippenberg. Octave spanning tunable frequency comb from a microresonator. *Physical Review Letters*, 107:063901, 2011.

[68] Kasturi Saha, Yoshitomo Okawachi, Bonggu Shim, Jacob S. Levy, Reza Salem, Adrea R. Johnson, Mark A. Foster, Michael R. E. Lamont, Michal Lipson, and Alexander L Gaeta. Modelocking and femtosecond pulse generation in chip-based frequency combs. *Optics Express*, 21:1335–1343, 2013.

[69] T. Herr, V. Brasch, J. D. Jost, C. Y. Wang, N. M. Kondratiev, M. L. Gorodetsky, and T. J. Kippenberg. Temporal solitons in optical microresonators. *Nature Photonics*, 8:145–152, 2014.

[70] Faraz Monifi, Jing Zhang, Şahin Kaya Özdemir, Bo Peng, Yu xi Liu, Fang Bo, Franco Nori, and Lan Yang. Optomechanically induced stochastic resonance and chaos transfer between optical fields. *Nature Photonics*, 10:399–405, 2016.

[71] Christophe Baker, Sebastian Stapfner, David Parrain, Sara Ducci, Giuseppe Leo, Eva M. Weig, and Ivan Favero. Optical instability and self-pulsing in silicon nitride whispering gallery resonators. *Opt. Express*, 20:29076, 2012.

[72] R Holzwarth, T Udem, Tw Hänsch, Jc Knight, Wj Wadsworth, and Ps Russell. Optical frequency synthesizer for precision spectroscopy. *Physical Review Letters*, 85:2264–7, 2000.

[73] D. J. Kaup and A. C. Newell. Theory of nonlinear oscillating dipolar excitations in one-dimensional condensates. *Physical Review B*, 18(10):5162, 1978.

[74] K. Nozaki and N. Bekki. Chaos in a perturbed nonlinear schrödinger equation. *Physical review letters*, 50(17):1226, 1983.

[75] K. Nozaki and N. Bekki. Low dimensional chaos in a driven damped nonlinear schrödinger equation. *Physica D*, 21:381–393, 1986.

[76] M. Haelterman, S. Trillo, and S Wabnitz. Dissipative modulation instability in a nonlinear dispersive ring cavity. *Optics Communications*, 91:401–407, 1992.

[77] S.A. Diddams, Th. Udem, J.C. Bergquist, E.A. Curtis, R.E. Drullinger, L. Hollberg, W.M. Itano, W.D. Lee, C.W. Oates, K.R. Vogel, and D.J Wineland. An optical clock based on a single trapped $^{199}Hg^+$ ion. *Science*, 293:825–828, 2001.

[78] A. Foltynowicz, P. Masowski, T. Ban, F. Adler, K. C. Cossel, T. C. Briles, and J. Ye. Optical frequency comb spectroscopy. *Faraday Discussions*, 150:23–31, 2011.

[79] Young-Shin Park and Hailin Wang. Regenerative pulsation in silica microspheres. *Opt. Lett*, 32:3104, 2007.

[80] Souleymane Diallo, Guoping Lin, and Yanne K. Chembo. Giant thermo-optical relaxation oscillations in millimeter-size whispering gallery mode disk resonators. *Opt. Lett.*, 40:3834, 2015.

[81] Chaitanya Joshi, Jae K. Jang, Kevin Luke, Xingchen Ji, Steven A. Miller, Alexander Klenner, Yoshitomo Okawachi, Michal Lipson, and Alexander L. Gaeta. Thermally controlled comb generation and soliton modelocking in microresonators. *Opt. Lett.*, 41:2565, 2016.

[82] V. E. Lobanov, G. V. Lihachev, N. G. Pavlov, A. V. Cherenkov, T. J. Kippenberg, and M. L. Gorodetsky. Harmonization of chaos into a soliton in kerr frequency combs. *Opt. Express*, 24:27382, 2016.

[83] S. Arnold, M. Khoshsima, I. Teraoka, S. Holler, and F. Vollmer. Shift of whispering-gallery modes in microspheres by protein adsorption. 28:272, 2003. ISSN 0146-9592. doi: 10.1364/ol.28.000272.

[84] Frank Vollmer and Stephen Arnold. Whispering-gallery-mode biosensing: label-free detection down to single molecules. 5:591–596, 2008. ISSN 1548-7091. doi: 10.1038/nmeth.1221.

[85] L. Collot, V. Lefevre-Seguin, M. Brune, J.M. Raimond, and S Haroche. Very high-q whispering-gallery mode resonances observed on fused silica microspheres. *Europhysics Letters*, 23:327–334, 1993.

[86] P.R Berman. *Cavity Quantum Electrodynamics*, 1994.

[87] Yang Deng, Fenfei Liu, Zayd C. Leseman, and Mani Hossein-Zadeh. Thermo-optomechanical oscillator for sensing applications. *Opt. Express*, 21:4653, 2013.

[88] Philip Holmes. Poincaré, celestial mechanics, dynamical-systems theory and "chaos". *Physics Reports*, 193(3):137 – 163, 1990.

[89] B. Van Der Pol and J. Van Der Mark. Frequency demultiplication. *Nature*, 120:363–364, 1927.

[90] M. L. Cartwright. On non-linear differential equations of the second order. *Mathematical Proceedings of the Cambridge Philosophical Society*, 45(4):495–501, 1949.

[91] M. L. CARTWRIGHT, E. A. CODDINGTON, H. F. DeBAGGIS, N. LEVINSON, J. Mc-Carthy, and H. L. TURRITTIN. *Contributions to the Theory of Nonlinear Oscillations (AM-29), Volume II*. Princeton University Press, 1952.

[92] Norman Levinson. A second order differential equation with singular solutions. *Annals of Mathematics*, 50(1):127–153, 1949.

[93] Kenneth R. Meyer. Qualitative theory of second-order dynamic systems (a. a. andronov, e. a. leontovich, i. i. gordon and a. g. maier); theory of bifurcations of dynamic systems on a plane (a. a. andronov, e. a. leontovich, i. i. gordon and a. g. maier). *SIAM Review*, 17(1): 183–184, 1975.

[94] Stephen Smale. Differentiable dynamical systems. *Bulletin of the American mathematical Society*, 73(6):747–817, 1967.

[95] IE Fermi, P Pasta, S Ulam, and M Tsingou. Studies of the nonlinear problems. Technical report, Los Alamos Scientific Lab., N. Mex., 1955.

[96] Thierry Dauxois. Fermi, pasta, ulam and a mysterious lady.

[97] Norman J Zabusky and Martin D Kruskal. Interaction of" solitons" in a collisionless plasma and the recurrence of initial states. *Physical review letters*, 15(6):240, 1965.

[98] Edward N Lorenz. Deterministic nonperiodic flow. *Journal of the atmospheric sciences*, 20 (2):130–141, 1963.

[99] Mitchell J Feigenbaum. Quantitative universality for a class of nonlinear transformations. *Journal of statistical physics*, 19(1):25–52, 1978.

[100] Philip Hartman. A lemma in the theory of structural stability of differential equations. *Proceedings of the American Mathematical Society*, 11(4):610–620, 1960.

[101] Yuri A Kuznetsov. *Elements of applied bifurcation theory*, volume 112. Springer Science & Business Media, 2013.

[102] Steven H. Strogatz. Nonlinear dynamics and chaos: With applications to physics, biology, chemistry, and engineering (steven h. strogatz). *SIAM Review*, 37:280–281, 1995.

[103] Vito Volterra. Variations and fluctuations of the number of individuals in animal species living together. *ICES Journal of Marine Science*, 3(1):3–51, 1928.

[104] John Rinzel and G Bart Ermentrout. Analysis of neural excitability and oscillations. *Methods in neuronal modeling*, pages 135–169, 1989.

[105] John Michael Tutill Thompson and H Bruce Stewart. *Nonlinear dynamics and chaos*. John Wiley & Sons, 1986.

[106] PHILIP GERALD Drazin and William Hill Reid. Hydrodynamic stability, 1981.

[107] Leonid Pavlovich Shilnikov. A case of the existence of a denumerable set of periodic motions. In *Sov. Math. Dokl.*, pages 163–166, 1965.

[108] John Robinson Pierce. Coupling of modes of propagation. *Journal of Applied Physics*, 25 (2):179–183, 1954.

[109] SE Miller. Coupled wave theory and waveguide applications. *Bell Labs Technical Journal*, 33(3):661–719, 1954.

[110] WH Louisell. Analysis of the single tapered mode coupler. *Bell Labs Technical Journal*, 34 (4):853–870, 1955.

[111] Talal Findakly and Chin-Lin Chen. Optical directional couplers with variable spacing. *Appl. Opt.,*, 17:769, 1978.

[112] Dietrich Marcuse. The coupling of degenerate modes in two parallel dielectric waveguides. *Bell Labs Technical Journal*, 50(6):1791–1816, 1971.

[113] Allan W Snyder. Coupled-mode theory for optical fibers. *JOSA*, 62(11):1267–1277, 1972.

[114] Allan W Snyder. Coupling of modes on a tapered dielectric cylinder. *IEEE transactions on microwave theory and techniques*, 18(7):383–392, 1970.

[115] H. F. Taylor and A. Yariv. Guided wave optics. *Proceedings of the IEEE*, 62(8):1044–1060, August 1974.

[116] H. F. Taylor. Optical switching and modulation in parallel dielectric waveguides. 44:3257–3262, 1973. ISSN 0021-8979.

[117] H. Kogelnik and R. Schmidt. Switched directional couplers with alternating ΔBcross-talk problems in optical directional couplers. 12:396–401, 1976.

[118] Juichi Noda, Masaharu Fukuma, and Osamu Mikami. Design calculations for directional couplers fabricated by ti-diffused $LiNbO_3$ waveguides. 20:2284, 1981. ISSN 0003-6935.

[119] H. Haus and C. Fonstad. Three-waveguide couplers for improved sampling and filtering. *IEEE Journal of Quantum Electronics*, 17(12):2321–2325, December 1981.

[120] Peter D. McIntyre and Allan W. Snyder. Power transfer between optical fibers. *J. Opt. Soc. Amer*, 63:1518, 1973.

[121] C. Yeh, F. Manshadi, K. F. Casey, and A. Johnston. Accuracy of directional coupler theory in fiber or integrated optics applications. *J. Opt. Soc. Amer*, 68:1079, 1978.

[122] M. Digonnet and H. Shaw. Analysis of a tunable single mode optical fiber coupler. *IEEE Journal of Quantum Electronics*, 18(4):746–754, April 1982.

[123] K. Thyagarajan and R. Tewari. Accurate analysis of single-mode graded-index fiber directional couplers. *Journal of Lightwave Technology*, 3(1):59–62, February 1985.

[124] M. Zhang and E. Garmire. Single-mode fiber-film directional coupler. *Journal of Lightwave Technology*, 5(2):260–267, February 1987.

[125] H. Haus and L. Molter-Orr. Coupled multiple waveguide systems. *IEEE Journal of Quantum Electronics*, 19(5):840–844, May 1983.

[126] H.A Haus, L. MOlter-Orr, and F.J. Leonberger. Multiple waveguide lens. *Appl. Phys. Lett.*, 45:19–21, 1984.

[127] J. Butler, D. Ackley, and M. Ettenberg. Coupled-mode analysis of gain and wavelength oscillation characteristics of diode laser phased arrays. *IEEE Journal of Quantum Electronics*, 21(5):458–464, May 1985.

[128] C. Elachi and C. Yeh. Frequency selective coupler for integrated optics systems. *Opt. Commun.*, 7:201–204, 1973.

[129] Harold Stoll and Amnon Yariv. Coupled-mode analysis of periodic dielectric waveguides. *Opt. Commun.*, 8:5–8, 1973.

[130] Pochi Yeh and H. F. Taylor. Contradirectional frequency-selective couplers for guided-wave optics. *Appl. Opt.*, 19:2848, 1980. ISSN 0003-6935. doi: 10.1364/ao.19.002848.

[131] R. R. A. Syms. Optical directional coupler with a grating overlay. *Appl. Opt.*, 24:717, 1985.

[132] D. Marcuse. Directional couplers made of nonidentical asymmetric slabs. part ii: Grating-assisted couplers. *Journal of Lightwave Technology*, 5(2):268–273, February 1987.

[133] Peter D. McIntyre and Allan W. Snyder. Power transfer between nonparallel and tapered optical fibers. *J. Opt. Soc. Amer.*, 64:285, 1974.

[134] Masanori Matsuhara and A. Watanabe. Coupling of curved transmission lines, and application to optical directional couplers. *J. Opt. Soc. Amer*, 65:163, 1975.

[135] M. G. F. Wilson and G. A. Teh. Tapered optical directional coupler. *IEEE Transactions on Microwave Theory and Techniques*, 23(1):85–92, January 1975.

[136] A. F. Milton and W. K. Burns. Tapered velocity couplers for integrated optics: Design. *Appl. Opt.*, 14:1207, 1975.

[137] R. Alferness and P. Cross. Filter characteristics of codirectionally coupled waveguides with weighted coupling. *IEEE Journal of Quantum Electronics*, 14(11):843–847, November 1978.

[138] Iain Anderson. On the coupling of degenerate modes on nonparallel dielectric waveguides. *Microwave, Opt., Acoust*, 3:56, 1979.

[139] M. Abouzahra and L. Lewin. Theory and application of coupling between curved transmission lines. *IEEE Transactions on Microwave Theory and Techniques*, 30(11):1988–1995, November 1982.

[140] M. A. McHenry and D. C. Chang. Coupled-mode theory of two nonparallel dielectric waveguides. *IEEE Transactions on Microwave Theory and Techniques*, 32(11):1469–1475, November 1984.

[141] F. de Fornel, C. M. Ragdale, and R. J. Mears. Analysis of single-mode fused tapered fibre couplers. *IEE Proceedings H Microwaves, Optics and Antennas*, 131(4):221–227, August 1984.

[142] J. Sakai and T. Kimura. Birefringence and polarization characteristics of single-mode optical fibers under elastic deformations. *IEEE J. Quantum Electron*, 17:1041–1051, 1981.

[143] J. Sakai and T. Kimura. Polarization behavior in multiply perturbed single-mode fibers. *IEEE Journal of Quantum Electronics*, 18(1):59–65, January 1982.

[144] K. Okamoto, Y. Sasaki, and N. Shibata. Mode coupling effects in stress-applied single polarization fibers. *IEEE Journal of Quantum Electronics*, 18(11):1890–1899, November 1982.

[145] J. A. Armstrong, N. Bloembergen, J. Ducuing, and P. S. Pershan. Interactions between light waves in a nonlinear dielectric. *Phys. Rev.*, 127:1918–1939.

[146] J. E. Sipe and G. I. Stegeman. Comparison of normal mode and total field analysis techniques in planar integrated optics. *J. Opt. Soc. Amer*, 69:1676, 1979.

[147] George I. Stegeman and Colin T. Seaton. Nonlinear integrated optics. *J. Appl. Phys.*, 58: R57–R78, 1985.

[148] Y. R. Shen. *Principles of Nonlinear Optics*. 1984.

[149] H. A. Haus and W. Huang. Coupled-mode theory. *Proceedings of the IEEE*, 79(10): 1505–1518, October 1991.

[150] B. Crosignani, P. Di Porto, and C. H. Papas. Coupled-mode theory approach to nonlinear pulse propagation in optical fibers. *Opt. Lett.*, 6:61, 1981.

[151] Bruno Crosignani, Antonello Cutolo, and Paolo Di Porto. Coupled-mode theory of nonlinear propagation in multimode and single-mode fibers: envelope solitons and self-confinement. *J. Opt. Soc. Amer.*, 72:1136, 1982.

[152] D. R. Andersen, S. Datta, and R. L. Gunshor. A coupled mode approach to modulation instability and envelope solitons. *Appl. Phys.*, 54:5608–5612, 1983.

[153] Kuo-Liang Chen and Shyh Wang. Cross-talk problems in optical directional couplers. *Appl. Phys.*, 44:166–168, 1984.

[154] A. Hardy and W. Streifer. Coupled mode theory of parallel waveguides. *Journal of Lightwave Technology*, 3(5):1135–1146, October 1985.

[155] A. Hardy and W. Streifer. Coupled modes of multiwaveguide systems and phased arrays. *Journal of Lightwave Technology*, 4(1):90–99, January 1986.

[156] E. A. J. Marcatili, L. L. Buhl, and R. C. Alferness. Experimental verification of the improved coupled-mode equations. *Appl. Phys. Lett.*, 49:1692–1693, 1986.

[157] H. Haus, W. Huang, S. Kawakami, and N. Whitaker. Coupled-mode theory of optical waveguides. *Journal of Lightwave Technology*, 5(1):16–23, January 1987.

[158] W. Streifer, M. Osinski, and A. Hardy. Reformulation of the coupled-mode theory of multiwaveguide systems. *Journal of Lightwave Technology*, 5(1):1–4, January 1987.

[159] W. Streifer. Coupled mode theory. *Electron. Lett.*, 23:315, 1987.

[160] William Streifer, Marek Osinski, and Amos Hardy. A critical review of coupled mode theory, 1987.

[161] Shun-Lien Chuang. A coupled-mode theory for multiwaveguide systems satisfying the reciprocity theorem and power conservation. *Journal of Lightwave Technology*, 5(1):174–183, January 1987.

[162] J. P. Donnelly, H.A. Haus, and L.A. Molter. Cross power and crosstalk in waveguide couplers. *Journal of Lightwave Technology*, 6(2):257–268, February 1988.

[163] Amos Hardy, William Streifer, and Marek Osinski. Weak coupling of parallel waveguides. *Opt. Lett.*, 13:161, 1988.

[164] H. A. Haus, A. W. Snyder, and W. P. Huang. Coupled-mode formulations. *Opt. Lett.*, 14:1222, 1989.

[165] W. P. Huang and H. A. Haus. Power exchange in grating-assisted couplers. *Journal of Lightwave Technology*, 7(6):920–924, June 1989.

[166] G. Agrawal. *Nonlinear Fiber Optics (Fifth Edition)*. 2013.

[167] W. P. Huang and H. A. Haus. Self-consistent vector coupled-mode theory for tapered optical waveguides. *Journal of Lightwave Technology*, 8(6):922–926, June 1990.

[168] A. Berzanskis, K.-H. Feller, and A. Stabinis. Squeezed light generation by means of cascaded second-order nonlinearity. *Optics Communications*, 118:438–446, 1995.

[169] M. Sebawe Abdalla, Faisal A. A. El-Orany, and J. Perina. Quantum statistical properties of nondegenerate optical parametric symmetric coupler. *Journal of Physics A: Mathematical and General*, 32:3457–3483, 1999.

[170] J. E. Sipe, N. Bhat, P. Chak, and S. Pereira. Effective field theory for pulse propagation in nonlinear photonic crystals. In *Proc. CLEO/Pacific Rim 2003. The 5th Pacific Rim Conf. Lasers and Electro-Optics (IEEE Cat. No.03TH8671)*, volume 1, pages 369 Vol.1–, December 2003.

[171] D. Michaelis, U. Peschel, C. Wächter, and A. Bräuer. Reciprocity theorem and perturbation theory for photonic crystal waveguides. *Phys. Rev. E*, 68.

[172] S. N. Volkov and J. E. Sipe. Nonlinear optical interactions of wave packets in photonic crystals: Hamiltonian dynamics of effective fields. *Phys. Rev. E*, 70.

[173] S. A. Schelkunoff. Conversion of Maxwell's equations into generalized telegraphist's equations. *The Bell System Technical Journal*, 34(5):995–1043, September 1955.

[174] H. Nishihara, M. Haruna, and T. Suhara. *Optical Integrated Circuits*. McGraw-Hill optical and electro-optical engineering series. McGraw-Hill, 1989.

[175] Alessia Pasquazi, Marco Peccianti, Luca Razzari, David J. Moss, Stéphane Coen, Miro Erkintalo, Yanne K. Chembo, Tobias Hansson, Stefan Wabnitz, Pascal Del'Haye, Xiaoxiao Xue, Andrew M. Weiner, and Roberto Morandotti. Micro-combs: A novel generation of optical sources. *Physics Reports*, 729:1–81, 2018.

[176] D. M. Pozar. *Microwave Engineering, 4th edition*. Wiley, 2009.

[177] Kerry J. Vahala. Optical microcavities. *Nature*, 424:839–846, 2003.

[178] A. B. Matsko and V. S. Ilchenko. Optical resonators with whispering-gallery modes-part i: basics. *IEEE Journal of Selected Topics in Quantum Electronics*, 12(1):3–14, January 2006.

[179] Hossein Rokhsari and Kerry J. Vahala. Observation of kerr nonlinearity in microcavities at room temperature. *Opt. Lett.*, 30:427, 2005.

[180] C. Y. Wang, T. Herr, P. Del'Haye, A. Schliesser, J. Hofer, R. Holzwarth, T. W. Hänsch, N. Picqué, and T. J. Kippenberg. Mid-infrared optical frequency combs at 2.5 um based on crystalline microresonators. *Nat Commun.*, 4:1345.

[181] Luigi Di Lauro, Jin Li, David J. Moss, Roberto Morandotti, Sai T. Chu, Marco Peccianti, and Alessia Pasquazi. Parametric control of thermal self-pulsation in micro-cavities. *Opt. Lett.*, 42:3407, 2017.

[182] Julien Clinton Sprott. *Chaos and Time-Series Analysis*. Oxford University Press, 2003.

[183] Víctor M. Perez-García, Gabriel F. Calvo, Juan Belmonte-Beitia, David Diego, and Luis Perez-Romasanta. Bright solitary waves in malignant gliomas. 84.

[184] D. O'Shea, C. Junge, S. Nickel, M. Poellinger, and A. Rauschenbeutel. Ultra-high q whispering-gallery-mode bottle microresonators: properties and applications. . doi: 10.1117/ 12.876790.

[185] D. O'Shea, C. Junge, M. Poellinger, A. Vogler, and A. Rauschenbeutel. All-optical switching and strong coupling using tunable whispering-gallery-mode microresonators. . doi: 10.1007/ s00340-011-4714-x.

[186] Peter Bermel, Alejandro Rodriguez, Steven G. Johnson, John D. Joannopoulos, and Marin Soljačić. Single-photon all-optical switching using waveguide-cavity quantum electrody-namics. 74. ISSN 1050-2947. doi: 10.1103/physreva.74.043818.

[187] Vilson R. Almeida, Carlos A. Barrios, Roberto R. Panepucci, and Michal Lipson. All-optical control of light on a silicon chip. 431:1081–1084, 2004. ISSN 0028-0836. doi: 10.1038/nature02921.

[188] T. Herr, V. Brasch, J. D. Jost, C. Y. Wang, N. M. Kondratiev, M. L. Gorodetsky, and T. J Kippenberg. Temporal solitons in optical microresonators. *Nature Photonics*, 8:145–152, 2014.

[189] Chaitanya Joshi, Jae K. Jang, Kevin Luke, Xingchen Ji, Steven A. Miller, Alexander Klenner, Yoshitomo Okawachi, Michal Lipson, and Alexander L. Gaeta. Thermally controlled comb generation and soliton modelocking in microresonators. 41:2565, 2016. ISSN 0146-9592. doi: 10.1364/ol.41.002565.

[190] Pablo Marin-Palomo, Juned N. Kemal, Maxim Karpov, Arne Kordts, Joerg Pfeifle, Martin H. P. Pfeiffer, Philipp Trocha, Stefan Wolf, Victor Brasch, Miles H. Anderson, Ralf Rosen-berger, Kovendhan Vijayan, Wolfgang Freude, Tobias J. Kippenberg, and Christian Koos. Microresonator-based solitons for massively parallel coherent optical communications. 546: 274–279.

[191] Akira Hasegawa. Optical solitons in fibers: theoretical review.

[192] T.J. Kippenberg, R. Holzwarth, and S.A Diddams. Microresonator-based optical frequency combs. *Science*, 332:555–559, 2011.

[193] K. M. Cuomo, A. V. Oppenheim, and S. H. Strogatz. Synchronization of lorenz-based chaotic circuits with applications to communications. 40:626–633, 1993. ISSN 1057-7130. doi: 10.1109/82.246163.

[194] I. S. Amiri, M. Ranjbar, A. Nikoukar, A. Shahidinejad, J. Ali, and P. P. Yupapin. Multi optical soliton generated by panda ring resonator for secure network communication, 2012.

[195] C. Kurtsiefer, P. Zarda, M. Halder, H. Weinfurter, P. M. Gorman, P. R. Tapster, and J. G. Rarity. A step towards global key distribution. 419:450–450, 2002. ISSN 0028-0836. doi: 10.1038/419450a.

[196] R. Ursin, F. Tiefenbacher, T. Schmitt-Manderbach, H. Weier, T. Scheidl, M. Lindenthal, B. Blauensteiner, T. Jennewein, J. Perdigues, P. Trojek, B. Oemer, M. Fuerst, M. Meyenburg, J. Rarity, Z. Sodnik, C. Barbieri, H. Weinfurter, and A. Zeilinger. Free-space distribution of entanglement and single photons over 144 km.

[197] Georges Kaddoum. Wireless chaos-based communication systems: A comprehensive survey. 4:2621–2648, 2016. ISSN 2169-3536. doi: 10.1109/access.2016.2572730.

[198] G. D. VanWiggeren. Communication with chaotic lasers. 279:1198–1200, 1998. ISSN 0036-8075. doi: 10.1126/science.279.5354.1198.

[199] C. R. Mirasso, J. Mulet, and C. Masoller. Chaos shift-keying encryption in chaotic external-cavity semiconductor lasers using a single-receiver scheme. 14:456–458, 2002. ISSN 1041-1135. doi: 10.1109/68.992576.

[200] X. Li, W. Pan, B. Luo, and D. Ma. Mismatch robustness and security of chaotic optical communications based on injection-locking chaos synchronization. 42:953–960, 2006. ISSN 0018-9197. doi: 10.1109/jqe.2006.880379.

[201] Wei Li Zhang, Wei Pan, Bin Luo, Xi Hua Zou, Meng Yao Wang, and Zhi Zhou. Chaos synchronization communication using extremely unsymmetrical bidirectional injections. 33: 237, 2008. ISSN 0146-9592. doi: 10.1364/ol.33.000237.

Appendix A

Numerical Algorithms for Stability and Dynamical Analysis of Microresonators

We report MatLab and Mathematica scripts that have been developed for this work, in order to study stability of the model equations 4.21 for an optical micro-cavity in a configuration where a pump and a signal are coupled, in presence of Kerr and thermo-optical effect in a third-order nonlinear material, considering four-wave mixing. We show also the numerical approach used to propagate the fields equations, based on Runge-Kutta method

A.1 System of Equations

Intra-cavity fields

```
%%%%%%%%%%%%%%%%%%%%%%%%%%%%%
% aa -> pump              %
% bb -> signal            %
% cc1 -> left idler       %
% cc2 -> right idler      %
% dd thermal detuning     %
%%%%%%%%%%%%%%%%%%%%%%%%%%%%%%
```

Parameters for the model

```
%%%%%%%%%%%%%%%%%%%%%%%%%%%%%%%%%%%%%%%%%%%%%%%%%%%%%%%%%
% sigma -> ratio between thermal decay time and photon lifetime %
% rho -> ratio between Kerr and thermo-optical coefficient     %
% dwa -> pump detuning                                         %
% dwb -> signal detuning                                       %
% aa_in -> pump input field                                    %
% bin_0 -> signal input field                                  %
% FWM -> four-wave mixing contributions on/off                 %
%%%%%%%%%%%%%%%%%%%%%%%%%%%%%%%%%%%%%%%%%%%%%%%%%%%%%%%%%
```

System of equations

```
%%%%%%%%%%%%%%%%%%%%%%%%%%%%%%%%%%%%%%%%%%%%%%%%%%%%%%%%%%%%%
% fa = @(aa,bb,cc1,cc2,dd,ain_0) (-(1i*dwa+1+1i*dd-1i*(abs(aa).^2+2 %
% *abs(bb).^2+2*abs(cc1).^2+2*abs(cc2).^2)).*aa+1i*FWM*(2*conj(aa)  %
% .*bb.*cc2+conj(cc1).*bb.^2+2.*conj(bb).*cc1.*cc2)-1i*ain_0);      %
%                                                                   %
% fb = @(aa,bb,cc1,cc2,dd,bin_0) (-(1i*dwb+1+1i*dd-1i*(2*abs(aa).^2 %
% abs(bb).^2+2*abs(cc1).^2+2*abs(cc2).^2)).*bb+1i*FWM.*(2*conj(bb)  %
% .*aa.*cc1+conj(cc2).*aa.^2+2.*conj(aa).*cc2.*cc1)-1i*bin_0);      %
%                                                                   %
% fc1 = @(aa,bb,cc1,cc2,dd) (-(1i*dwc1+1+1i*dd-1i*(2*abs(aa).^2+2*  %
% abs(bb).^2+abs(cc1).^2+2*abs(cc2).^2)).*cc1 +1i*FWM.*(conj(aa)    %
% .*bb.^2+2*conj(cc2).*aa.*bb));                                    %
%                                                                   %
% fc2 = @(aa,bb,cc1,cc2,dd) (-(1i*dwc2+1+1i*dd-1i*(2*abs(aa).^2+2*  %
% abs(bb).^2+2*abs(cc1).^2+abs(cc2).^2)).*cc2 +  1i*FWM.*(conj(bb)  %
% .*aa.^2+2*conj(cc1).*bb.*aa));                                    %
%                                                                   %
% fd = @(aa,bb,cc1,cc2,dd) (rho*(abs(aa).^2+abs(bb).^2+abs(cc1).^2  %
% +abs(cc2).^2)-dd)./sigma;                                         %
%%%%%%%%%%%%%%%%%%%%%%%%%%%%%%%%%%%%%%%%%%%%%%%%%%%%%%%%%%%%%
```

A.2 Numerical Stability: Case of Degenerate Four-Wave Mixing

```
% sol_c, function that returns the stationary solutions given
% bb and the arrays a_vet (intra-cavity field) and
% dwa_vet (pump detuning).
% cc is the lowest energy solution for the idler.
[cc,err,c01,c02,c03] = solc(rho,dwb,a_vet,dwa_vet,bb,FWM);


[Dwa,aa]=meshgrid(dwa_vet,a_vet);
dd = rho.*(abs(aa).^2+abs(bb).^2+abs(cc).^2);


% Input fields
ain = 1i*(1i*Dwa+ 1 + 1i*dd  - 1i* (  abs(aa).^2+2*abs(bb).^2+...
2*abs(cc).^2))*aa+ FWM*2*conj(aa).*bb.*cc;


bin = 1i*(1i*dwb+ 1 + 1i*dd  - 1i* (2*abs(aa).^2+  abs(bb).^2...
+2*abs(cc).^2))*bb+   FWM*conj(cc).*aa.^2;



% Calculating the eigenvalues of the stationary solutions
for numa = 1:length(a_vet)
    for numd = 1:length(dwa_vet)
       dwa=Dwa(numa,numd)
        dwc=2*dwa-dwb;
```

```
% Steady state solution
a0 = aa(numa,numd);

a0r = real(a0);

a0i = imag(a0);

b0r = real(b0);

b0i = imag(b0);

c0r = real(cc(numa,numd));

c0i = imag(cc(numa,numd));

d0=dd(numa,numd);


% Jacobian matrix for the perturbative approach
eqar = [(-1)+(-2).*a0i.*a0r+(-2).*(b0r.*c0i+b0i.*c0r)...

.*FWM,(-3).*a0i.^2+(-1).*a0r.^2+(-2).*b0i.^2+(-2).*b0r...

.^2+(-2).*c0i.^2+.(-2).*c0r.^2+d0+dwa+(-2).*b0i.*c0i...

.*FWM+2.*b0r.*c0r.*FWM,(-4)*a0i.*b0r+(-2).*a0r.*c0i....

*FWM+2.*a0i.*c0r.*FWM,(-2).*(2.*a0i.*b0i+a0i.*c0i....

*FWM+ a0r.*c0r.*FWM),(-4).*a0i.*c0r+(-2).*a0r.*b0i....

*FWM+2.*a0i.*b0r.*FWM,(-2).*(2.*a0i.*c0i+a0i.*b0i.*FWM...

+a0r.*b0r.*FWM),a0i];


eqai = [a0i.^2+3.*a0r.^2+2.*b0i.^2+2.*c0i.^2+2.*c0r...

.^2+(-1).*d0+(-1).*dwa+(-2).*b0i.*c0i.*FWM+2.*b0r...

.*(b0r+c0r.*FWM),(-1)+2.*a0i.*a0r+2.*b0r.*c0i.*FWM...

+2.*b0i.*c0r.*FWM,2.*(2.*a0r.*b0r+a0i.*c0i.*FWM+a0r...

.*c0r.*FWM),4.*a0r.*b0i+(-2).*a0r.*c0i.*FWM+2.*a0i....

*c0r.*FWM,2.*(2.*a0r.*c0r+a0i.*b0i.*FWM+a0r.*b0r....

*FWM),4.*a0r.*c0i+(-2).*a0r.*b0i.*FWM+2.*a0i.*b0r....

*FWM,(-1).*a0r];
```

```
eqbr = [(-4).*a0r.*b0i+2.*a0r.*c0i.*FWM+(-2).*a0i...
.*c0r.*FWM,(-2).*(2.*a0i.*b0i+a0i.*c0i.*FWM+a0r....
*c0r.*FWM),(-1)+(-2).*b0i.*b0r,(-2).*a0i.^2+(-2)....
*a0r.^2+(-3).*b0i.^2+(-1).*b0r.^2+(-2).*c0i.^2+(-2)...
.*c0r.^2+d0+dwb,(-2).*(2.*b0i.*c0r+a0i.*a0r.*FWM),(-4)...
.*b0i.*c0i+((-1).*a0i.^2+a0r.^2).*FWM,b0i];


eqbi = [2.*(2.*a0r.*b0r+a0i.*c0i.*FWM+a0r.*c0r.*FWM),...
4.*a0i.*b0r+2.*a0r.*c0i.*FWM+(-2).*a0i.*c0r.*FWM,2...
.*a0i.^2+2.*a0r.^2+b0i.^2+3.*b0r.^2+2.*c0i.^2+2.*c0r...
.^2+(-1).*d0+(-1).*dwb,(-1)+2.*b0i.*b0r,4.*b0r.*c0r+...
((-1).*a0i.^2+a0r.^2).*FWM,4.*b0r.*c0i+2.*a0i.*a0r....
*FWM,(-1).*b0r];


eqcr = [(-4).*a0r.*c0i+2.*a0r.*b0i.*FWM+(-2).*a0i...
.*b0r.*FWM,(-2).*(2.*a0i.*c0i+a0i.*b0i.*FWM+a0r...
.*b0r.*FWM),(-2).*(2.*b0r.*c0i+a0i.*a0r.*FWM),...
(-4).*b0i.*c0i+((-1).*a0i.^2+a0r.^2).*FWM,(-1)...
+(-2).*c0i.*c0r,(-2).*a0i.^2+(-2).*a0r.^2+(-2)...
.*b0i.^2+(-2).*b0r.^2+(-3).*c0i.^2+(-1).*c0r...
.^2+d0+dwc,c0i];


eqci = [2.*(2.*a0r.*c0r+a0i.*b0i.*FWM+a0r.*b0r...
.*FWM),4.*a0i.*c0r+2.*a0r.* b0i.*FWM+(-2).*a0i...
*b0r.*FWM,4.*b0r.*c0r+((-1).*a0i.^2+a0r.^2).* ...
FWM,4.*b0i.*c0r+2.*a0i.*a0r.*FWM,2.*a0i.^2+2...
.*a0r.^2+2.*b0i.^2+2.*b0r.^2+c0i.^2+3.*c0r...
.^2+(-1).*d0+(-1).*dwc,(-1)+2.*c0i.*c0r,(-1).* ...
 c0r];
```

```
eqd = 1./sigma*([2*rho0.*a0r,2*rho0.*a0i,2...
*rho0.*b0r,2*rho0.*b0i,2*rho0.*c0r,2*rho0.*c0i,-1]);


% Eigenvalues
op = [eqar.',eqai.',eqbr.',eqbi.',eqcr.',eqci.',eqd.'].';
[eigvect eigval] = eig(op);
eigval0 = [eigval(1,1) eigval(2,2) eigval(3,3) eigval...
(4,4) eigval(5,5) eigval(6,6) eigval(7,7)];


% Sorting out the eigenvalues
[dum ind] = sort(imag(eigval0));
[dumr indr] = sort(real(eigval0));
eigval_vett(numa,numd,:) = (eigval0(ind));


% Eigenvalues variable
eigval_vettr(numa,numd,:) = (eigval0(indr));
end
end


% Test to determine the stability of the equilibria (US states for
%% the unstable points, SP for the self-pulsing points)
th = 1e-15;
US = zeros(length(a_vet),length(dwa_vet),length(l));
SP = US;
for num=1:7
US = US+((real(eigval_vett(:,:,:,num))>0)....
*(abs(imag(eigval_vett(:,:,:,num)))<th).*1);
SP = SP+((real(eigval_vett(:,:,:,num))>0)...
.*(1-(abs(imag(eigval_vett(:,:,:,num)))<th))*1);
end
```

```
% Results of the test
test = (US(:,:,:)>0)*1.5+(SP(:,:,:)>0)*2;


% Function that return the boundaries of the US and SP regions
PdSP1 = real(psp1(rho_vet,dwa_vet,dwb,b0,sigma));

PdSP2 = real(psp2(rho_vet,dwa_vet,dwb,b0,sigma));

PdU1 = real(psu1(rho_vet,dwa_vet,dwb,b0,sigma));

PdU2 = real(psu2(rho_vet,dwa_vet,dwb,b0,sigma));

PdU3 = real(psu3(rho_vet,dwa_vet,dwb,b0,sigma));

PdU4 = real(psu4(rho_vet,dwa_vet,dwb,b0,sigma));


% Strong regime boundaries
Pda11u = (-1).*(dwa+b0.^2.*((-2)+rho)).*((-1)+rho).^(-1);


Pda22u = (-1).*(dwa+b0.^2.*((-1)+rho)).*((-2)+rho).^(-1);


Pda33u = (-1/6).*(2+(-3).*rho+rho.^2).^(-1).*((-3).*b0...
.^2+(-2).*dwa+(-3).*dwb+(-6).*b0.^2.*rho+dwa.*rho+3.*dwb...
.*rho+6.*b0.^2.*rho.^2+((-12).*(dwa+b0.^2.*((-2)+rho))...
.*(dwb+3.*b0.^2.*((-1)+rho)).*(2+(-3).*rho+rho.^2)+(dwa...
.*((-2)+rho)+3.*dwb.*((-1)+rho)+b0.^2.*((-3)+(-6).*rho+6...
.*rho.^2)).^2).^(1/2));


Pda44u = (1/6).*(2+(-3).*rho+rho.^2).^(-1).*(3.*b0.^2+2...
.*dwa+3.*dwb+6.*b0.^2.*rho+(-1).*dwa.*rho+(-3).*dwb.*rho...
+(-6).*b0.^2.*rho.^2+((-12).*(dwa+b0.^2.*((-2)+rho))...
.*(dwb+3.*b0.^2.*((-1)+rho)).*(2+(-3).*rho+rho.^2)+(dwa...
.*((-2)+rho)+3.*dwb.*((-1)+rho)+b0.^2.*((-3)+(-6).*rho+6...
.*rho.^2)).^2).^(1/2));
```

```
% Single pump US and SP boundaries
PPdSP1 = real((1/2).*((-1)+rho).^(-1).*(rho.*((-1)+s)+(-3)...
.*s).^(-1).*(dwa.*rho+4.*dwa.*s+(-2).*dwa.*rho.*s+s.*(s....
^(-3).*((-4).*((-1)+rho).*(rho.*((-1)+s)+(-3).*s)....
*(1+s).^2+dwa.^2.*s.*(rho+2.*s).^2)).^(1/2)));


PPdSP2 = real((1/2).*((-1)+rho).^(-1).*(rho.*((-1)+s)+(-3)...
.*s).^(-1).*(dwa.*rho+4.*dwa.*s+(-2).*dwa.*rho.*s+(-1).*s....
*(s.^(-3).*((-4).*((-1)+rho).*(rho.*((-1)+s)+(-3).*s)....
*(1+s).^2+dwa.^2.*s.*(rho+2.*s).^2)).^(1/2)));


PPdU1 = real((-1/3).*(2.*dwa.*((-1)+rho)+(((-3)+dwa.^2)...
.*((-1)+rho).^2).^(1/2)).*((-1)+rho).^(-2));


PPdU2 = real( (1/3).*((-2).*dwa.*((-1)+rho)+(((-3)+dwa.^2)...
.*((-1)+rho).^2).^(1/2)).*((-1)+rho).^(-2));
```

A.3 Numerical Continuation of the Equilibrium Curve

```
% Initial guess

x0=fsolve(@(x01) system_eqs(x01,dwa,dwb,dwc1,dwc2,rho,FWM...

,a0,b0,1),x01,options);


dd=rho*(abs(x2(1)).^2+abs(x0(2)).^2+abs(x0(3)).^2+abs(x0(4)).^2);
```

MatCont scripts

```
%%%%%%%%%%%%%%%%%%%%%%%%%%%%%%%%%%%%%%%%%%%%%%%%%%%%%%%%%%%%%%%%%%%%

% This function intialize the vectors for the continuation of the  %

% equilibrium curve                                                %

%                                                                  %

% [x1,v1] = init_EP_EP(@system_eqs,[real(x2(1));imag(x2(1));       %

% real(x2(2));imag(x2(2));real(x2(3));imag(x2(3));real(x2(4));     %

% imag(x2(4));dd],par,pos);                                        %

%                                                                  %

% Continuation of the equilibrium curve                           %

%                                                                  %

% [xf,vf,sf,hf,ff] = cont(@equilibrium,x1,v1,opt);                %

%                                                                  %

% Moving backward along the curve                                 %

%                                                                  %

% opt=contset(opt,'Backward',1);                                  %

% [xb,vb,sb,hb,fb] = cont(@equilibrium,x1,v1,opt);                %

%                                                                  %

% xf and xb are the vector containing the steady state curve and  %

% the type of bifurcation that may have been occurred             %

%%%%%%%%%%%%%%%%%%%%%%%%%%%%%%%%%%%%%%%%%%%%%%%%%%%%%%%%%%%%%%%%%%%%
```

A.4   Numerical Propagation of the Model Equations

A step-adaptive Runge-Kutta-Fehlberg Method (RKF45) has been used to perform the numerical propagation of the intra-cavity fields

```
% Runge-Kutta parameters
%%%%%%%%%%%%%%%%%%%%%%%%%%%%%%%%%%%%%%%%%%%%%%%
% maxt -> number of seconds for the propagation %
% eps -> error in approximating the solution    %
% h -> initial step                             %
% tstep -> t=tstep, initial time                %
%%%%%%%%%%%%%%%%%%%%%%%%%%%%%%%%%%%%%%%%%%%%%%%%


% Solution at t = 0, with initial guess x0
x=fsolve(@(x0) stablestate(x0,dwa,dwb,dwc1,dwc2,rho,FWM,ain_0...
,bin_0,1),x0,options);
aa=x(1);
bb=x(2);
cc1=x(3);
cc2=x(4);
dd=rho*(abs(aa)^2+abs(bb)^2+abs(cc1)^2+abs(cc2)^2);


% Runge-Kutta-Fehlberg RK(45)
i=1;
while tstep<maxt

    % saving the i-th value of the fields
    AA(i) = aa;
    BB(i) = bb;
    CC1(i) = cc1;
    CC2(i) = cc2;
    DD(i) = dd;
    t(i) = tstep; % saving the time step
```

```
h = min(h,maxt-tstep); % adjusting the step


%Runge-Kutta-Fehlberg coefficients

k1a = h*fa(aa,bb,cc1,cc2,dd,ain_0);

k1b = h*fb(aa,bb,cc1,cc2,dd,bin_0);

k1c1 = h*fc1(aa,bb,cc1,cc2,dd);

k1c2 = h*fc2(aa,bb,cc1,cc2,dd);

k1d = h*fd(aa,bb,cc1,cc2,dd);


k2a = h*fa(aa+k1a/4,bb+k1b/4,cc1+k1c1/4,cc2+k1c2/4,...
dd+k1d/4,ain_0);

k2b = h*fb(aa+k1a/4,bb+k1b/4,cc1+k1c1/4,cc2+k1c2/4,...
dd+k1d/4,bin_0);

k2c1 = h*fc1(aa+k1a/4,bb+k1b/4,cc1+k1c1/4,cc2+k1c2/4,...
dd+k1d/4);

k2c2 = h*fc2(aa+k1a/4,bb+k1b/4,cc1+k1c1/4,cc2+k1c2/4,...
dd+k1d/4);

k2d = h*fd(aa+k1a/4,bb+k1b/4,cc1+k1c1/4,cc2+k1c2/4,dd...
+k1d/4);


k3a = h*fa(aa+3*k1a/32+9*k2a/32,bb+3*k1b/32+9*k2b/32,...
cc1+3*k1c1/32+9*k2c1/32,cc2+3*k1c2/32+9*k2c2/32,dd+...
3*k1d/32+9*k2d/32,ain_0);


k3b = h*fb(aa+3*k1a/32+9*k2a/32,bb+3*k1b/32+9*k2b/32...
,cc1+3*k1c1/32+9*k2c1/32,cc2+3*k1c2/32+9*k2c2/32,dd+...
3*k1d/32+9*k2d/32,bin_0);


k3c1 = h*fc1(aa+3*k1a/32+9*k2a/32,bb+3*k1b/32+9*k2b/32...
,cc1+3*k1c1/32+9*k2c1/32,cc2+3*k1c2/32+9*k2c2/32,dd+...
3*k1d/32+9*k2d/32);
```

```
k3c2 = h*fc2(aa+3*k1a/32+9*k2a/32,bb+3*k1b/32+9*k2b/32,...
cc1+3*k1c1/32+9*k2c1/32,cc2+3*k1c2/32+9*k2c2/32,dd+...
3*k1d/32+9*k2d/32);


k3d = h*fd(aa+3*k1a/32+9*k2a/32,bb+3*k1b/32+9*k2b/32,...
cc1+3*k1c1/32+9*k2c1/32,cc2+3*k1c2/32+9*k2c2/32,dd+...
3*k1d/32+9*k2d/32);


k4a = h*fa(aa+1932*k1a/2197-7200*k2a/2197+7296*k3a/2197...
,bb+1932*k1b/2197-7200*k2b/2197+7296*k3b/2197,cc1+1932...
*k1c1/2197-7200*k2c1/2197+7296*k3c1/2197,cc2+1932*k1c2/...
2197-7200*k2c2/2197+7296*k3c2/2197,dd+1932*k1d/2197-7200...
*k2d/2197+7296*k3d/2197,ain_0);


k4b = h*fb(aa+1932*k1a/2197-7200*k2a/2197+7296*k3a/2197...
,bb+1932*k1b/2197-7200*k2b/2197+7296*k3b/2197,cc1+1932...
*k1c1/2197-7200*k2c1/2197+7296*k3c1/2197,cc2+1932*k1c2/...
2197-7200*k2c2/2197+7296*k3c2/2197,dd+1932*k1d/2197-7200...
*k2d/2197+7296*k3d/2197,bin_0);


k4c1 = h*fc1(aa+1932*k1a/2197-7200*k2a/2197+7296*k3a/2197...
,bb+1932*k1b/2197-7200*k2b/2197+7296*k3b/2197,cc1+1932...
*k1c1/2197-7200*k2c1/2197+7296*k3c1/2197,cc2+1932*k1c2...
/2197-7200*k2c2/2197+7296*k3c2/2197,dd+1932*k1d/2197-7200...
*k2d/2197+7296*k3d/2197);


k4c2 = h*fc2(aa+1932*k1a/2197-7200*k2a/2197+7296*k3a/2197...
,bb+1932*k1b/2197-7200*k2b/2197+7296*k3b/2197,cc1+1932...
*k1c1/2197-7200*k2c1/2197+7296*k3c1/2197,cc2+1932*k1c2...
/2197-7200*k2c2/2197+7296*k3c2/2197,dd+1932*k1d/2197-7200...
*k2d/2197+7296*k3d/2197);
```

```
k4d = h*fd(aa+1932*k1a/2197-7200*k2a/2197+7296*k3a/2197...
,bb+1932*k1b/2197-7200*k2b/2197+7296*k3b/2197,cc1+1932...
*k1c1/2197-7200*k2c1/2197+7296*k3c1/2197,cc2+1932*k1c2...
/2197-7200*k2c2/2197+7296*k3c2/2197,dd+1932*k1d/2197-7200...
*k2d/2197+7296*k3d/2197);



k5a = h*fa(aa+439*k1a/216-8*k2a+3680*k3a/513-845*k4a/4104,...
bb+439*k1b/216-8*k2b+3680*k3b/513-845*k4b/4104,cc1+439*...
k1c1/216-8*k2c1+3680*k3c1/513-845*k4c1/4104,cc2+439*k1c2/...
216-8*k2c2+3680*k3c2/513-845*k4c2/4104,dd+439*k1d/216-8*...
k2d+3680*k3d/513-845*k4d/4104,ain_0);


k5b = h*fb(aa+439*k1a/216-8*k2a+3680*k3a/513-845*k4a/4104,...
bb+439*k1b/216-8*k2b+3680*k3b/513-845*k4b/4104,cc1+439*...
k1c1/216-8*k2c1+3680*k3c1/513-845*k4c1/4104,cc2+439*k1c2/...
216-8*k2c2+3680*k3c2/513-845*k4c2/4104,dd+439*k1d/216-8*...
k2d+3680*k3d/513-845*k4d/4104,bin_0);


k5c1 = h*fc1(aa+439*k1a/216-8*k2a+3680*k3a/513-845*k4a/4104,...
bb+439*k1b/216-8*k2b+3680*k3b/513-845*k4b/4104,cc1+439*...
k1c1/216-8*k2c1+3680*k3c1/513-845*k4c1/4104,cc2+439*k1c2/...
216-8*k2c2+3680*k3c2/513-845*k4c2/4104,dd+439*k1d/216-8*...
k2d+3680*k3d/513-845*k4d/4104);


k5c2 = h*fc2(aa+439*k1a/216-8*k2a+3680*k3a/513-845*k4a/4104,...
bb+439*k1b/216-8*k2b+3680*k3b/513-845*k4b/4104,cc1+439*...
k1c1/216-8*k2c1+3680*k3c1/513-845*k4c1/4104,cc2+439*k1c2/...
216-8*k2c2+3680*k3c2/513-845*k4c2/4104,dd+439*k1d/216-8*...
k2d+3680*k3d/513-845*k4d/4104);
```

```
k5d = h*fd(aa+439*k1a/216-8*k2a+3680*k3a/513-845*k4a/4104,...

bb+439*k1b/216-8*k2b+3680*k3b/513-845*k4b/4104,cc1+439*...

k1c1/216-8*k2c1+3680*k3c1/513-845*k4c1/4104,cc2+439*k1c2/...

216-8*k2c2+3680*k3c2/513-845*k4c2/4104,dd+439*k1d/216-8*...

k2d+3680*k3d/513-845*k4d/4104);


k6a = h*fa(aa-8*k1a/27+2*k2a-3544*k3a/2565+1859*k4a/4104-...

11*k5a/40,bb-8*k1b/27+2*k2b-3544*k3b/2565+1859*k4b/4104-...

11*k5b/40,cc1-8*k1c1/27+2*k2c1-3544*k3c1/2565+1859*k4c1/...

4104-11*k5c1/40,cc2-8*k1c2/27+2*k2c2-3544*k3c2/2565+1859...

*k4c2/4104-11*k5c2/40,dd-8*k1d/27+2*k2d-3544*k3d/2565+...

1859*k4d/4104-11*k5d/40,ain_0);


k6b = h*fb(aa-8*k1a/27+2*k2a-3544*k3a/2565+1859*k4a/4104-...

11*k5a/40,bb-8*k1b/27+2*k2b-3544*k3b/2565+1859*k4b/4104-...

11*k5b/40,cc1-8*k1c1/27+2*k2c1-3544*k3c1/2565+1859*k4c1...

/4104-11*k5c1/40,cc2-8*k1c2/27+2*k2c2-3544*k3c2/2565+1859...

*k4c2/4104-11*k5c2/40,dd-8*k1d/27+2*k2d-3544*k3d/2565+1859...

*k4d/4104-11*k5d/40,bin_0);


k6c1 = h*fc1(aa-8*k1a/27+2*k2a-3544*k3a/2565+1859*k4a/4104-...

11*k5a/40,bb-8*k1b/27+2*k2b-3544*k3b/2565+1859*k4b/4104-...

11*k5b/40,cc1-8*k1c1/27+2*k2c1-3544*k3c1/2565+1859*k4c1...

/4104-11*k5c1/40,cc2-8*k1c2/27+2*k2c2-3544*k3c2/2565+1859...

*k4c2/4104-11*k5c2/40,dd-8*k1d/27+2*k2d-3544*k3d/2565+1859...

*k4d/4104-11*k5d/40);
```

```
k6c2 = h*fc2(aa-8*k1a/27+2*k2a-3544*k3a/2565+1859*k4a/4104...

-11*k5a/40,bb-8*k1b/27+2*k2b-3544*k3b/2565+1859*k4b/4104-...

11*k5b/40,cc1-8*k1c1/27+2*k2c1-3544*k3c1/2565+1859*k4c1...

/4104-11*k5c1/40,cc2-8*k1c2/27+2*k2c2-3544*k3c2/2565+1859...

*k4c2/4104-11*k5c2/40,dd-8*k1d/27+2*k2d-3544*k3d/2565+1859...

*k4d/4104-11*k5d/40);


k6d = h*fd(aa-8*k1a/27+2*k2a-3544*k3a/2565+1859*k4a/4104...

-11*k5a/40,bb-8*k1b/27+2*k2b-3544*k3b/2565+1859*k4b/4104-...

11*k5b/40,cc1-8*k1c1/27+2*k2c1-3544*k3c1/2565+1859*k4c1...

/4104- 11*k5c1/40,cc2-8*k1c2/27+2*k2c2-3544*k3c2/2565+1859...

*k4c2/4104-11*k5c2/40,dd-8*k1d/27+2*k2d-3544*k3d/2565+1859...

*k4d/4104-11*k5d/40);


aa_1 = aa+25*k1a/216+1408*k3a/2565+2197*k4a/4104-k5a/5;
bb_1 = bb+25*k1b/216+1408*k3b/2565+2197*k4b/4104-k5b/5;
cc1_1 = cc1+25*k1c1/216+1408*k3c1/2565+2197*k4c1/4104-k5c1/5;
cc2_1 = cc2+25*k1c2/216+1408*k3c2/2565+2197*k4c2/4104-k5c2/5;
dd_1 = dd+25*k1d/216+1408*k3d/2565+2197*k4d/4104-k5d/5;


aa_2 = aa + 16*k1a/135+6656*k3a/12825+28561*k4a/56430-9*k5a...

./50+2*k6a/55;
bb_2 = bb + 16*k1b/135+6656*k3b/12825+28561*k4b/56430-9*k5b...

./50+2*k6b/55;
cc1_2 = cc1 + 16*k1c1/135+6656*k3c1/12825+28561*k4c1/56430-...

9*k5c1/50+2*k6c1/55;
cc2_2 = cc2 + 16*k1c2/135+6656*k3c2/12825+28561*k4c2/56430-...

9*k5c2/50+2*k6c2/55;
dd_2 = dd + 16*k1d/135+6656*k3d/12825+28561*k4d/56430-9*k5d

/50+2*k6d/55;
```

```matlab
    Ra = abs(aa_1-aa_2)/h;

    Rb = abs(bb_1-bb_2)/h;

    Rc1 = abs(cc1_1-cc1_2)/h;

    Rc2 = abs(cc2_1-cc2_2)/h;

    Rd = abs(dd_1-dd_2)/h;


    %Error estimation
    delwa = 0.84*(eps/Ra)^(1/4);

    delwb = 0.84*(eps/Rb)^(1/4);

    delwc1 = 0.84*(eps/Rc1)^(1/4);

    delwc2 = 0.84*(eps/Rc2)^(1/4);

    delwd = 0.84*(eps/Rd)^(1/4);


    if (Ra<=eps && Rb<=eps && Rc1<=eps && Rc2<=eps && Rd<=eps)
        tstep = tstep+h;

        aa = aa_1;

        bb = bb_1;

        cc1 = cc1_1;

        cc2 = cc2_1;

        dd = dd_1;

        i = i+1;

        h = min([delwa,delwb,delwc1,delwc2,delwd])*h;
    else
        h = min([delwa,delwb,delwc1,delwc2,delwd])*h;

    end

end
```